POSITRON ANNIHILATION STUDY OF SUPERIONIC CONDUCTORS

Thulani Phillip Jili

A thesis submitted to the Faculty of Science, University of the Witwatersrand, Johannesburg, in fulfillment of the requirements for the degree of

Doctor of Philosophy

School of Physics

2017

Declaration

I declare that this thesis is my own unaided work. It is being submitted for the degree of Doctor of Philosophy in the University of the Witwatersrand, Johannesburg. It has not been submitted for any degree or examination in other University

_____

Signature of candidate

_____ day of _____ 20 _____ in _____

Abstract

Different experimental techniques have clearly demonstrated that the predominant intrinsic point defects in ionic barium fluoride are anion Frenkel pairs. Positron annihilation technique is utilized in obtaining Doppler broadening and positron lifetime spectra in the temperature range 300 - 900 K. Doppler broadening quantifies the defects whereas positron lifetime components elaborate on the nature of defects.

Theoretical approach by density functional theory (DFT) and the generalized gradient approximation (GGA) in the calculation of electron-positron momentum density (or Doppler broadening) spectra at 0 K show that the positron annihilations decay predominantly with barium valence electrons, especially the 5p and 6s electrons and to a lesser extent with core electrons. These annihilations contribute towards the electron-positron momentum density. The annihilations with valence electrons partly contribute toward the short positron lifetime component. The positron-electron annihilations in barium atoms increase steadily with temperature. At 693 K, the annihilation fraction due to the Ba-atom when the anionic Frenkel is formed is found to be 84.44% compared to 15.56% for the fluorine atom. These annihiltions become part of a larger bulk positron-electron annihilations which form a short positron lifetime component. It is also noted that for F-divacancy at 693 K, the annihilation fraction due to 5p and 6s valence electrons in Ba increases by 2.13% to 86.57% indicating the role of defect clusters

in the annihilation process.

The long positron lifetime decreases in the temperature range from 500 ps at 300 K to 402 ps at 711 K, corresponds to a fractional increase of 22% in the temperature range 300 K to 693 K. The long positron lifetime component is attributed to a delocalized positronium which quickly annihilates through the pick-off (spin conversion) process. Pick-off process seems to be the dominant processes in the long positron lifetime component.

The self-diffusion, at all temperature ranges, of cations Ba^{2+} in barium fluoride is several orders of magnitude smaller than that of F^{-} which has a diffusion constant of $10^{-9}\ m^2/s$ at 300 K. Therefore the contribution of cations in superionic conductivity in the temperature range can be ignored. This is also supported by the absence of third lifetime component which is an indication that only anionic vacancies, F^{-}, are generated in the temperature range. The variation of the lattice constant with temperature as determined by X-ray diffraction becomes a major factor in the determination of S-parameters as a function of temperature hence it can reveal the critical temperature at which the formation of anion Frenkel defects commences before entering superionic region. The disordering of fluorine sublattice is found to deviate from linear behaviour at a temperature of 580 K (S-parameter of 0.50622 and lattice constant of 0.623 nm) without observing any appreciable superionic conductivity. X-ray diffraction technique provides a lattice constant of 0.625 nm at 693 K (corresponding to S-parameter of 0.50776) through which an appreciable small activity in conduction is first observed. This is demonstrated through the correlation between the lattice constants and conductivity values at elevated temparatures. This effectively means that lattice constant increases exponentially with temperature.

Ilmenite ($FeTiO_3$) which is an ionic conductor in which a permanent dipole moment can be formed by local changes in the environment of Ti^{4+} ion. It was used to test the validity the positron annihilation spectroscopy in a completely different environment of this corundum structure of space group R-3. The observed long positron lifetime components in comparison with theoretical calculations clearly show that these long positron lifetime components emanate from positron annihilations at metallic vacancies Fe^{2+}. Mössbauer pressure effect confirms the increase of Fe^{3+} at high pressure. At ambient conditions (pressure and temperature), the ratio Fe^{3+}/Fe^{2+} is small but gradually increase as the pressure increase. The relative intensity clearly shows a dramatic increase of the Fe^{3+} component with pressure.

Further test was carried out using variable positron beam on a 100 keV Ar^+ implanted LiF in the fluence range of $10^{12} - 10^{16}$ $ions/m^2$. In the process of ion implantation on alkali halides, ion vacancies in the form of F centers are formed. Using the penetration depth profile, S-parameter at different incident positron beams from 0.03 to 25 keV energies identifies the concentration of defects. This identification was also confirmed by optical absorption which clearly identified the F-band at 242 nm and F2-band at 444 nm.

Keywords:

Doppler broadening, positron lifetime, S-parameter, W-parameter, penetration depth profile, lattice constant, X-ray diffraction, optical absorption, density functional theory, generalized gradient approximation.

Firstly, I would like to thank Almighty God for keeping me safe during those sleepless nights at the iThemba Laboratory for Accelerator Based Sciences (TLABS) Research Unit. Many thanks go to my wife Duduzile Brenda Pinky Jili and my kids Xolo, Khethi, Thando and Siyabonga for their genuine support, understanding and encouragement. I also dedicate this work to my late mother Teresa Komzan Hlongwa whose support kept me going.

Acknowlegdement

I would like to thank my supervisor Prof. Elias Sideras-Haddad for his guidance and being inspirational. I would also like to thank Dr Daniel Wamwangi, my co-supervisor, who walked this road with me.

Special thanks go to Dr Ilja Makonnen for his invaluable discussions on issues related to theoretical analysis. I am also grateful to Mr Sergio Ballestrero and Dr Ian Korir for the sacrifice they made in making time available to come and empower me with their amazing skills in computational analysis.

I am also grateful to the Aalto University positron group (Finland) for allowing me to utilize their state-of-art coincidence set-up during my overseas visit. Special thanks go to Prof. Filip Tuomesto, who is the Head of Positron Group, for his invaluable discussions. Many thanks go to Mr Jussi-Matti Maki, who is also a member of positron group at Aalto University, for his kind assistance in setting up the experiment and in data analysis.

My sincere gratitude go to Dr Isaac Machi, who was then the Group Head of IThemba LABS Gauteng, for his assistance with infrastructure and equipment. Many thanks go to Prof Dave Billing and his team for their assistance with X-ray

diffraction equipment.

I record with appreciation the financial support of the National Research Foundation (NRF), the University of Zululand and the University of the Witwatersrand.

Many thanks go to my colleagues at the University of Zululand, especially Prof OM Ndwandwe, Dr CL Ndlangamandla, Prof EJ Sendezera (my former colleague), Dr B Kibirige, Dr S Ntshangase, Dr Nimreraou, Prof B Spoelstra, Prof J Msomi, Dr N Biyela, Ms N Chonco, Mr A Sefage, Mr S Khanyile, Mr T Nyawo, Mr T Masango, Mrs N Mothapo, Mr N Zungu and Dr M Madhuku.

Many thanks go to Prof OEHM Nxumalo and Dr Tshitshi Mbatha for their encouragement and support.

I am also grateful to all my teachers from primary to high school, especially my science teachers Dr Sipho Ntuli and Mr Oscar Nzimande, who were my source of inspiration.

Contents

Declaration ii
Abstract iii
Acknowledgement vii
List of Figures xiii
List of Tables xvi

1 Introduction 1

1.1 Categories of superionic conductors 2

1.1.1 Class I Superionics 2

1.1.2 Class II Superionics 3

1.1.3 Class III Superionics 3

1.2 Motivation 6

1.3 Layout of the thesis 7

2 Theory of positron creation and annihilation and the formation of positronium 9

2.1 Positron creation 9

2.2 Positron annihilation 10

2.3 Positronium formation 12

2.4 Practical application of positron annihilation 17

3 Slowing Down and Thermalization of Positrons in Solids 18

3.1 The transport equation 19

3.2 Momentum scattering and slowing down density 20

3.3 Narrow collision interval 22

3.4 Sample-integrated quantities 23

4 Diffusion and trapping 26

4.1 Positron diffusion equation 27

4.1.1 Positron diffusion coefficient 30

4.2 Positron trapping into defects 31

4.2.1 Positron trapping models 32

4.3 Positron trapping in semiconductors 38

5 Theoretical framework of positron-matter interaction 40

5.1 Two-component Density Functional theory 40

5.1.1 Generalized Kohn-Sham method 40

5.1.2 Local-Density Approximation (LDA) 41

5.1.3 Delocalized positron states 43

5.1.4 Localized positron states 46

5.2 Positron states in semiconductors and insulators 48

5.3 The momentum distribution of electron-positron pairs 50

6 Properties and structural probes of superionic conductors 53

6.1 Properties of superionic conductors 53

6.2 Ionic diffusion 54

6.3 Ionic conductivity dependence with temperature 57

6.4 Structural probes 59

6.5 Specific heat capacity of superioinc conductors 61

6.6 Bulk modulus dependence on temperature 63

6.7 Thermal expansion coefficient 66

6.8 The behaviour of superionics based on defect concentration and structures 70

7 Positron Annihilation Experimental Arrangement 72

7.1 Vacuum Chamber 72
7.2 Source-Sample-Heater Mounting System 74
7.3 Doppler Broadening and Positron Lifetime Experimental Arrangements 76
7.3.1 Doppler Broadening Spectroscopy 76
7.3.2 Lifetime measurement technique 81
7.3.3 Variable-energy slow positron beam 86

8 Experimental results, analysis and discussion 88
8.1 Lattice constant measurements in BaF_2 using XRD 89
8.2 Determination of S- and W-parameters in ionic BaF_2 91
8.2.1 Analysis and discussion 91
8.3 Positron lifetime in barium flouride 96
8.3.1 Analysis and discussion 98
8.3.2 Positron-electron momentum density in BaF_2 103
8.3.3 Temperature-dependent S-parameter in BaF_2 in the framework of GGA 109
8.4 Positron lifetime in $FeTiO_3$ 111
8.4.1 Analysis and discussion 113
8.5 Positron annihilation in alkali halides using a variable energy positron beam 117
8.5.1 Optical absorption analysis of LiF implanted with Ar^+ . . 117
8.5.2 Positron beam analysis of LiF implanted with Ar^+ 120
8.5.3 The effect of implantation on the resistivity in argon-implanted LiF 123
8.6 Comparison of theory with experiment 123

9 Conclusion 127

Bibliography 132

List of Figures

Figure

1.1 Temperature dependence of conductivity for three different classes of superionic conductors 4

2.1 Decay Scheme of ^{22}Na 11
2.2 Positron emission spectrum 11
2.3 Positronium energy spectrum 14

4.1 Trapping Model for a single-type defect 33
4.2 Trapping Model for more than one type of defect 36
4.3 Positron potentials 39
4.4 Temperature dependence of positron trapping coefficient 39

5.1 Positron-electron correlation energy 45
5.2 $\Gamma(\rho_-)$ versus electron density parameter r_s 47

6.1 Potential along diffusion path 54
6.2 Different diffusion mechanisms 58
6.3 Excess specific heat in PbF_2 against temperature 64
6.4 Frenkel defect against temperature 64
6.5 Specific heat against temperature 65
6.6 Bulk modulus against temperature for BaF_2 67

6.7 Thermal expansion against temperature 69
6.8 A 2/2/2 cluster in pure CaF_2 71

7.1 Vacuum pumping system 73
7.2 Source-sample-heater arrangement 75
7.3 Heater components 75
7.4 Thermal conductivity versus temperature in chromel-alumel . . . 77
7.5 Detector 1 energy versus Detector 2 energy 80
7.6 Doppler broadening circuit diagram 80
7.7 Positron stability of 1275 keV peak 82
7.8 S-parameter of the 1275 keV peak 82
7.9 Fast timing circuit 84
7.10 Slow positron beam 87

8.1 X-ray diffraction patterns at different temperatures. 90
8.2 XRD pattern fitted with reference pattern 90
8.3 Lattice constant as a function of temperature in BaF_2 92
8.4 S-parameter versus temperature 92
8.5 Determination of wing parameters 93
8.6 S- versus W- parameters 93
8.7 Conductivity versus temperature 95
8.8 Decomposition of positron lifetime spectrum 97
8.9 Positron lifetime spectrum 99
8.10 Positron lifetime components 99
8.11 Ortho to para-positronium conversion 100
8.12 Pick-off annihilation process 101
8.13 Positron lifetime intensities 102

8.14 Free-atom annihilation rates in Ba and F atoms within IPM and LDA 104
8.15 Free-atom annihilation rates in Ba and F atoms within the IPM, GGA and LDA 106
8.16 Decomposition of electron-positron annihilation momentum in barium sates 106
8.17 Decomposition of electron-positron annihilation momentum in flourine states. 107
8.18 Annihilation probabilty ratios for barium and flourine. 107
8.19 Normalized total electron-positron momentum density. 108
8.20 Calculated annihilation rates 110
8.21 Calculated enhancement factor 110
8.22 Comparison of S-parameter between the values obtained from theory and experiment. 112
8.23 $FeTiO_3$ structure 113
8.24 Positron annihilation ratios in $FeTiO_3$ 114
8.25 Bulk and defect positron lifetime components 116
8.26 Average positron lifetime in $FeTiO_3$ 118
8.27 Positron lifetime as a function of the number of vacancies in Fe . 118
8.28 Absorbance against photon wavelength 119
8.29 Makhov profiles 121
8.30 Positron implantation energy versus S-parameter. 121
8.31 Resisivity as a function fluence 124

List of Tables

Table

1.1 Class I superionics conductors 2

6.1 Formation of energies of Frenkel and Schottky defects in alkaline flourites 56

8.1 Enhancement factors calculated using LDA and GGA 104

8.2 Annihilation fractions at different core and valence states of atoms of the lattice 108

8.3 Positron annihilation ratios in $FeTiO_3$ 116

8.4 Annihilation fractions at different core states of atoms of the lattice 122

Chapter 1

Introduction

Barium Flouride (BaF_2) has been studied for its unique intrinsic light properties [98, 165, 59, 105] and so far it is considered the fastest luminescent material [97]. It is suitably used in energy and particle detectors [164]. BaF_2 exhibits superionic conductivity through the variation of temperature to above the transition temperature of about 700 K. The vacancy generation mechanism around the transition temperature has been the subject of many contradictions as will be discussed later in this chapter. Some researchers have introduced known quantities of impurities into the lattice [162, 197] to maximize its conductivity at low temperatures. BaF_2 is now considered as a suitable material for high temperature cells e.g. for electric cars.

Another material of interest is lead flouride (PbF_2). The basic understanding of the nature of superionic state has presented many challenges. Theoretical and experimental approaches are in many cases difficult because of dynamical structural disorders which characterizes superionic conduction.

Table 1.1: Different Class I cationic and anionic conductors

Material	Type	Transitional Temperature (^oC)
CuI	Cationic	369 [114]
Cu_2HgI_4	Cationic	70 [190]
Cu_2S	Cationic	122 [151]
LuF_2	Anionic	945 [189]
Bi_2O_3	Anionic	730 [185]
YF_3	Anionic	1052 [189]

1.1 Categories of superionic conductors

Generally a large number of ionic materials are insulators at low temperatures. Their activation energies are comparable to those of liquids at high temperatures. The classification of superionics is based on how the superionic state is achieved [136, 25].

1.1.1 Class I Superionics

This category of superionic materials is composed of both anionic and cationic conductors. These materials achieve their superionic conduction state through the mobility of cations immediately following the alpha-beta phase transition. AgI is a typical example of type I superionic material. At 147 ^oC the conductivity of this material undergoes a superionic transition typically of about three orders of magnitude [191]. The iodine sublattice changes from a hexagonal closed-packed structure to a body-centered cubic [85] (space group Im3m) when the cation (silver) structure undergoes a disruption from ordered to disordered state. Some of the cationic and anionic conductors in this class are shown in table 1.1

1.1.2 Class II Superionics

This group of superionics achieve its high level of conductivity following a gradual and continuous disordering [98] process without any phase transition. Superionic transition in these materials commence at temperatures yT_m, well below their melting point T_m such that $y \in (0, 1)$. For PbF_2, $y = 0.523$ and 0.823 for $SrCl_2$ [25]. Anomaly in the specific heat capacity is associated with this group. BaF_2 and $\beta - PbF_2$ are typical type II superionics. Na Super Ionic Conductor (NASICON) falls also in this category.

1.1.3 Class III Superionics

Materials in this category achieve high levels of ionic conduction through the increased mobility [98] of thermally activated defects. The disordering in these compounds is anomalously low in the sense that this class of materials attains its superionic conduction without notable phase change from ion-insulating to the superionic state. Ionic conductivity versus temperature on an Arrhenius plot for type III would show a linear behaviour. Some of type III materials display a broad specific heat anomaly at the transitional temperature [60, 166]. These researchers attribute the specific anomaly to the development of anion disorder in the diffuse phase transition. Figure 1.1 displays the superionic behaviour of conductivity of different classes versus temperature [98].

Another interesting feature of PbF_2 is the lowest cation-anion interaction coefficient [54]. Researchers have studied the superionic-ionic transition in $Cd_{1-x}Pb_xF_2$. The $Cd_{1-x}Pb_xF_2$ undergoes a superionic transition in crystal (PbF_2) to an ionic crystal (CdF_2) [101]. This behaviour is characterised by the rapid diffusion of a significant fraction of one of the constituent ions [98]. Intense experimental and

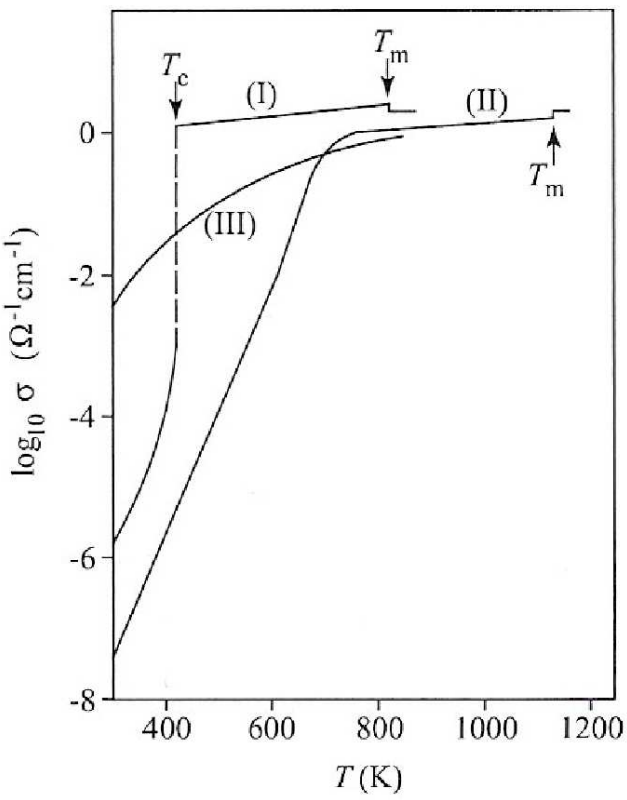

Figure 1.1: Typical plots of ionic conductivity against temperature for three different classes of superionic conductors [98, 85].

theoretical efforts have been made to explain this effect. The mechanism associated with fast-ions conductors has not been convincingly explained and perhaps this can be attributed to the fact that disorder is often thermally activated [98]. It has been established that it can result from a gradual or a first order structural phase transition. Generally the superionics apply to materials whose ionic conductivity σ is greater than $10^{-2}\ \Omega^{-1}m^{-1}$.

The high increase in conductivity is accompanied by an increase in heat content also from transition temperature (T_c) [55, 60, 174]. Materials with flourite structure display pronounced specific heat capacities anomaly at temperatures well below their melting temperatures, T_m [35]. This anomaly is associated with the disorder of anion sublattice.

Another interesting naturally occurring ilmenite in the form of $FeTiO_3$ is studied in this work using positron annihilation spectroscopy. It is based on a hexagonal-close-packed (HCP) oxygen lattice with metal atoms occupying two-thirds of the available octahedral sites. [202]. This is an interesting material which is used in the manufacture of titanium dioxide for paint pigments. Titanium itself is used to manufacture aircraft parts and artificial joints for humans. Therefore it is extremely important that defects associated with ilmenites be investigated using positron annihilation technique and its ionic conductivity at various temperatures as a test of the experiment and theory.

Positron annihilation technique presents itself as a vital non-destructive tool to study various defect types in ionic crystals and other solid materials [62, 63, 10, 64, 70, 152, 170].

Ionic crystal studies are associated with two or more positron lifetime components [198] which are defect type specific. This allows the identification of nature and quantity of defects in ionic materials [142]. Therefore a conclusion can be drawn that ionic crystals and some condensed media exhibit a wider spectrum of positron and positronium states [26].

1.2 Motivation

Many studies that have been conducted show that the interactions between defects slow down the rate at which interstitials are generated until a certain threshold concentration is reached [149] in which defect-defect interactions become prominent. The high conductivity at elevated temperature is a direct consequence of the mobility of these thermally activated defects [149, 68, 35, 56, 57]. Other researchers have considered a massive disodering of the anion sublattice above the transitional temperature [149, 111, 1]. It is clear that defect-generation mechanism in superionic conductors is not yet fully understood. Some ion-transport mechanisms [38] were not fully investigated.

This work addresses the question of defect generation (responsible for superionic region) in relation to the temperature, that is, at what critical temperature are the defects responsible for superionic conduction created. Are they created below or above the transitional temperature T_c or are they created at the transitional temperature? Positron annihilation technique has been under utilized in studying the role of vacancies in superionic state and particularly in the study of defect generation in the neighborhood of the transitional temperature in type II superionics. The features presented by positron annihilation technique stimulate an

interest in theoretical and experimental work more especially in the analysis of positron annihilations in ionic materials and other condensed media.

1.3 Layout of the thesis

This thesis is comprised of an abstract, acknowledgement, nine chapters, an appendix and a list of references.

- Chapter one. This chapter gives a description of three categories of superionic conductors and how superionic conduction is achieved at elevated temperatures without any structural phase change.

- Chapter two. This chapter describes how positronium states (singlet and triplet) are formed and their annihilation process. Recent applications of positron annihilation technique are briefly discussed.

- Chapter three. This chapter contains theoretical background on the slowing down and thermalization of positrons in solids. The theory entails the transport equation, the momentum scattering and slowing down density, narrow collision interval and sample-integrated quantities.

- Chapter four. This chapter discusses the effect of thermalization of positrons. At this stage, the onset of diffusion in the lattice as charged particles, is considered. The diffusion equation which includes the positron implantation profile is discussed. Trapping of positrons at different defects follow the diffusion process. Trapping models are also discussed.

- Chapter five. This chapter describes the density functional theory in the context of generalized Kohn-Sham method, localized density approximation and delocalized and localized positron states. The electron-positron

momentum density which describes annihilation probabilities with core and valence electrons of the host sample is discussed.

- Chapter six. In this chapter, the properties and structural probes of superionic conductors are discussed. The formation energies of Frenkel and Schottky defects in certain alkaline earth fluoride structures are presented. The specific heat anomaly in these structures at elevated temperatures is also discussed.

- Chapter seven. This chapter describes various components of equipment used to obtain positron lifetime and Doppler broadening spectra. Variable energy slow positron beam utiized for bulk and surface studies in ionic LiF implanted with 100 keV argon ions at different fluencies, is also discussed.

- Chapter eight. This chapter presents experimental results, analysis and discussions.

- Chapter nine. In this chapter, the conclusion and suggestions related to this work are presented.

Chapter 2

Theory of positron creation and annihilation and the formation of positronium

In 1932 Carl Anderson, while studying cosmic rays identified a new strange particle from the tracks in his cloud chamber. He interpreted the strange tracks to be from a particle of the same mass as the electron but with positive polarity [9], and his findings confirmed the existence of positrons as was earlier predicted by Paul Dirac.

2.1 Positron creation

Positrons are obtained from β^+ active isotopes through the decay scheme given by $^{22}Na \rightarrow {}^{22}Ne + e^+ + \nu$ where e^+ is the emitted positron. Positrons emitted from the radioactive source have a wider range of energy spectrum given by [108]

$$N(E)dE = gF(Z,E)pE(E_{max} - E)^2 dE \tag{2.1}$$

where $N(E)$, g, and E are number of decays, coupling constant and total energy of the positron respectively [108]. E_{max} and p are maximum energy and momentum

of the positron. $F(Z,E)$ refers to the Fermi function [108]. The Fermi function [203] for the allowed transitions is given by the expression [108]

$$F_{allowed}(Z,E) = \frac{2\pi\eta}{1-e^{-2\pi\eta}} \tag{2.2}$$

where $\eta = \frac{-Z\alpha E}{p}$.

The commonly used β^+ isotope is ^{22}Na which decays according to the scheme $^{22}Na \rightarrow {}^{22}Ne + e^+ + \nu$ as shown in figure 2.1 and the corresponding positron emission spectrum is shown in figure 2.2.

2.2 Positron annihilation

In nature there are three processes in which positron undergoes an annihilation with an electron. The first process involves the annihilation of a free positron with a free electron. The second process involves the annihilation of positron-electron pair in the presence of an external field. The third process involve a process in which the annihilation produces one-photon emission and although the probability for this to happen is extremely small, it cannot be neglected.

In two-photon annihilation, the cross section of annihilation increases with a decrease in relative speed between positron and the electron [20, 69, 160] as shown below,

$$\sigma_{2\gamma} = \sigma_D = \pi r_o^2 \frac{c}{v} \tag{2.3}$$

where r_o is the classical electron radius and σ_D the differential cross section which approaches infinity as the relative speed v approaches zero although the positron annihilation rate λ_D tends to a finite limit given by equation (2.4),

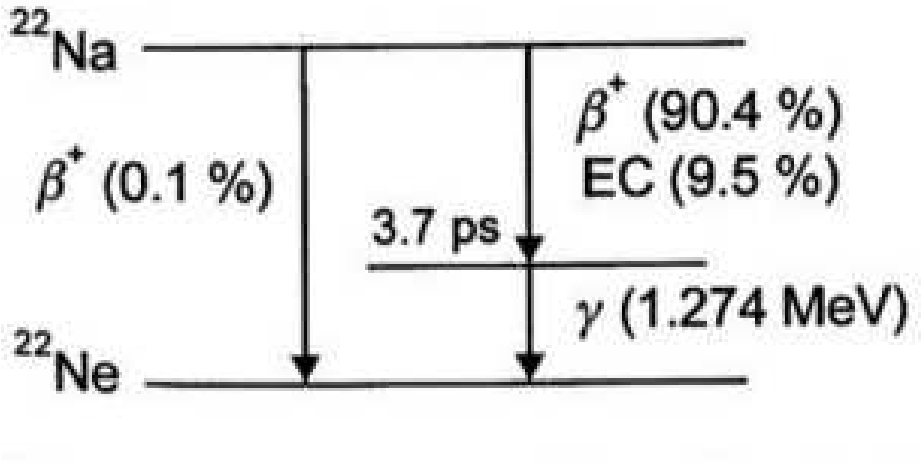

Figure 2.1: Decay scheme of radioactive ^{22}Na to ^{22}Ne [104]

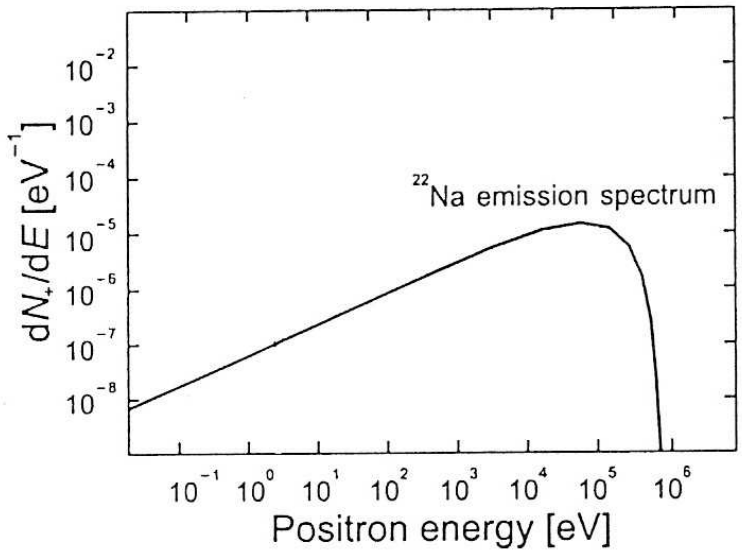

Figure 2.2: Positron emission spectrum from Na^{22} decay [104].

$$\lambda_D = \sigma_D v n_e = \pi r_o^2 c n_e \tag{2.4}$$

where n_e is the electron density.

For the annihilation pair to take place, the momentum and energy laws must be conserved leading to the equations given by

$$k_1 + k_2 = p = 2mv \tag{2.5}$$

$$k_1 c + k_2 c = E = 2mc^2 \tag{2.6}$$

where m, k_i are relativistic mass and photon momenta, respectively. The electron-positron pair's center of mass is moving with speed v.

For non-zero v values, the individual photon's direction differ from 180^o and thus shifted from 511 keV. If the pair's momentum is less than m_oc, the deviation angle is defined by [104]

$$sin(\theta) \cong \frac{p_\perp}{m_o c} \tag{2.7}$$

and the Doppler shifted energy takes the form

$$\Delta E_\gamma \cong \frac{p_\parallel c}{2} \tag{2.8}$$

2.3 Positronium formation

The simplest bound system of e^+ and e^- is known as a positronium (Ps) irrespective of the relative spins. The energy levels of a single electron atom is given by the equation (2.9) [6]

$$E_n = -\frac{\alpha^2 Z^2 m_e c^2}{2n^2} \tag{2.9}$$

where Z is the nuclear charge and α the fine structure constant.

Since the positron and the electron have equal masses, m_e in equation (2.9) is replaced by the reduced mass, $m_e/2$, leading to the energy equation;

$$\begin{aligned} E_n &= -\frac{\alpha^2}{n^2}\frac{m_e c^2}{4} \\ &= -\frac{6.8}{n^2} eV \end{aligned} \tag{2.10}$$

Different ways of positronium formation are given by [133, 132]. These energy levels are all defined relative to the two particles at rest and at infinite separation, so that the energy level describes the extent to which the two particles are bound as shown in figure 2.3.

Bound state velocities of positronium are non-relativistic and are approximately given by

$$\frac{v}{c} = \frac{\alpha}{n} \tag{2.11}$$

and this is the reason why the relativistic correction for the equation (2.10) is small. The positronium wavefunctions, taking into account the reduced mass, have the same form as those of hydrogen atom. The n=1 state of the positronium is thus;

$$\Psi_{n=1}(r) = \frac{1}{\sqrt{\pi a_{p_s}^3}} e^{-\frac{r}{a_{p_s}}} \tag{2.12}$$

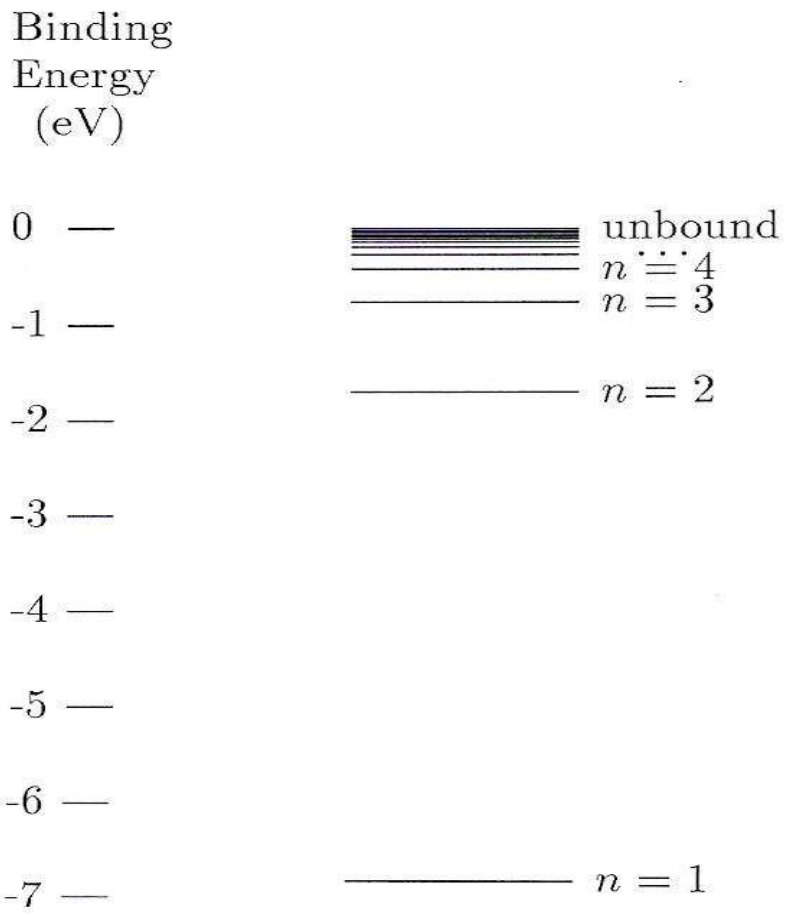

Figure 2.3: Positronium energy spectrum. On this scale the splittings among levels with the same principal quantum number n are too small to be visible [6].

The ground state for hydrogen is stable, since both electron and proton are stable but in the case of positronium the positron and electron can annihilate into two or three photons and therefore the probability is high enough to make the lifetime of the positronium very short. Interestingly, Crater et al. [49] proposed the existence of a distinctive four photon decay emission of the ordinary singlet bound state of positronium.

For n=1, the ground states, we have the singlet state 1^1S_0 (para-positronium, para-Ps) where the total spin angular momentum is equal to zero and the triplet state 1^3S_1 (ortho-positronium, ortho-Ps) has the total spin angular momentum equals to one. Many annihilations occur in the $1S$ states. The $2S$ states have smaller amplitudes at the origin resulting in their annihilation probability being smaller. The $2P$ state wavefunctions are extremely small at the origin and as a result the annihilation probability is very small. Therefore an excited positronium will undergo deexcitation by emitting photons until it arrives at one of the $1S$ states, and annihilate there.

Three substates of orthopositronium have different magnetic quantum numbers m and zero for parapositronium. The cross sections for the two annihilation processes depend on the relative spin between the two particles.

Positronium system can annihilate according to the following schemes

$$e^+e^- \longrightarrow \gamma\gamma$$

or

$$e^+e^- \longrightarrow \gamma\gamma\gamma$$

and that the "virtual" annihilations

$$e^+e^- \longrightarrow \gamma \longrightarrow e^+e^-$$

need to be considered to get a correct calculation of energy levels and the quantum electrodynamics (QED) provides a good description of the electromagnetic force rather than a theory based on the Coulomb force. Pertubation theory in QED is employed to calculate decay probabilities as well as the corrections due to $e^+e^- \longrightarrow \gamma \longrightarrow e^+e^-$. This leads to the ground states widths for o-Ps and p-Ps. Orthopositronium $^3S_1$ ground state three-photon decay width [30, 99, 117, 3] is given by

$$\begin{aligned}\Gamma_o^{th} &= \frac{2(\pi^2-9)\alpha^6 m_e}{9\pi}\Big\{1+\frac{\alpha}{\pi}10.286606+(\frac{\alpha}{\pi})^2\left[\frac{\pi^2}{3}ln\alpha+44.87\right] \\ &\quad +\frac{\alpha^3}{\pi}\left[-\frac{3}{2}ln^2\alpha+(3.428869-\frac{229}{30}-8ln2)\times ln\alpha+\frac{D_o}{\pi^2}\right]\Big\} \quad (2.13)\end{aligned}$$

and the 1^1S_0 parapositronium (p-Ps) ground state decay width [76, 50, 4] is given by

$$\begin{aligned}\Gamma_p^{th} &= \frac{\alpha^5 m_e}{2}\Big\{1+\frac{\alpha}{\pi}(\frac{\pi^2}{4}-5)+(\frac{\alpha}{\pi})^2\left[-2\pi^2 ln\alpha+5.1243\right] \\ &\quad \times\frac{\alpha^3}{\pi}\left[-\frac{3}{2}ln^2\alpha+(\frac{533}{90}-\frac{\pi^2}{2}+10ln2)ln\alpha+\frac{D_p}{\pi^2}\right]\Big\} \quad (2.14)\end{aligned}$$

where $\alpha = 1/137$ is the electromagnetic coupling constant or fine structure constant.

The theoretical value for parapositronium (p-Ps) lifetime was found to be 123.91 ps [159]. The best theoretical value for orthopositronium (o-Ps) is 142.08 ns [14] and was experimentally confirmed to be 141.88 ns [123].

2.4 Practical application of positron annihilation

A number of experiments on positron annihilation experiments have been done [96, 154, 179, 107, 176, 200, 77, 167, 119, 29]. An overview of some recent applications is provided by [169, 112, 184].

Positron annihilation technique, apart from being non-destructive, has an advantage over many techniques in identifying point defects [58] at various temperature conditions. Linderoth et al [109] has clearly demonstrated that average positron lifetime has a strong dependence on the annealing temperature of the material. Theoretical calculations, in which average positron lifetimes and momenta are obtained, have been carried out for various metals [44, 181, 143, 51, 91].

The electron-positron annihilation momentum density in a solid can be obtained from various positron techniques or can be reconstructed from experimental data of angular correlation of positron annihilation experiments. Various reconstruction techniques are discussed by Pecora [137]. Shiotani et al [177] also provide some insight on how angular correlation of annihilating radiation (ACAR) values be found through the utilization of X-rays. Experimental and theoretical studies on semiconductors using annihilation techniques have been performed by [204, 147, 140]. Positron annihilation technique has also played a pivotal role in the study of superconducting materials with high critical temperatures [17, 113, 72].

Chapter 3

Slowing Down and Thermalization of Positrons in Solids

Positrons entering a condensed matter undergo a slowing down and thermalization processes. Generally, the time difference between the implantation of a positron in a condensed matter and its thermalization time is shorter than its lifetime [172]. During a slowing down process, the loss of energy by the slowing down positron is temperature independent whereas during the thermalization process the loss of energy depends on the sample temperature. Generally, the energy range for positrons emitted during β^+ decay is from about 100 keV to few MeV [172]. Typical kinetic energies in slow positron beams range from few keV to about 50 keV. If relativistic positron beams [183] are considered (e.g 4 MeV) about 15 percent of the positrons incident in lead, for example, annihilate in flight [192]. During a positronium formation, the amount of energy loss per unit time, dE/dt, is quickly reduced because of charge neutrality of positronium leading to the end of slowing down process[171].

3.1 The transport equation

Various variables that characterize the transport equation include the position $\mathbf{r}$, time t and the unit vector associated with positron's direction $\boldsymbol{\xi}$. The number of positrons per unit volume, m, depends on $\mathbf{r}$, t, $\mathbf{p}$ and $\boldsymbol{\xi}$ where $\mathbf{p}$ is the particle's momentum. Therefore the quantity

$$m(\mathbf{r}, \boldsymbol{\xi}, p; t) d^3\mathbf{r} d^2\boldsymbol{\xi} dp \tag{3.1}$$

gives the number of positrons contained in the differential volume element $d^3\mathbf{r}d^2\xi dp$ at time t [172]. The relationship between flux and number density is given by [172]

$$\Phi(\mathbf{r}, \boldsymbol{\xi}, p; t) = vm(\mathbf{r}, \boldsymbol{\xi}, p; t) \tag{3.2}$$

where v is the speed of positrons.

The transport equation is then expressed as [172]

$$\begin{aligned} \frac{\partial n(\mathbf{r}, \boldsymbol{\xi}, p; t)}{\partial t} &= -\boldsymbol{\xi} \bullet \boldsymbol{\nabla}\Phi(\mathbf{r}, \boldsymbol{\xi}, \mathbf{p}; \mathbf{t}) \\ &\quad -(\Omega_s + \Omega_a)\Phi(\mathbf{r}, \boldsymbol{\xi}, p; t) \\ &\quad + \int_0^\infty \oint \Omega_s(\boldsymbol{\xi}' \rightarrow \boldsymbol{\xi}, p' \rightarrow p)\Phi(\mathbf{r}, \boldsymbol{\xi}', p; t) dp' d^2\xi' \\ &\quad + S(\mathbf{r}, \xi, p; t) \end{aligned} \tag{3.3}$$

Consider the terms on the right hand side of equation 3.3. The first negative term refers to the rate at which particles are lost out of the differential volume. The second term is associated with the energy lost due to scatterings in other different directions and also due electron-positron annihilations and trappings [172]. The positive third term refers to the gain in scatterings into $d^3\mathbf{r}d^2\xi dp$ from other

directions rather than the one defined by the unit vector ξ. The second and third terms are related through the following equation [172]

$$\Omega_p(p) = \int_0^\infty \Omega_s(p' \rightarrow p)dp' \tag{3.4}$$

with

$$\Omega_s(p' \rightarrow p) = \oint \Omega_s(\boldsymbol{\xi}' \rightarrow \boldsymbol{\xi}, p' \rightarrow p)d^2\boldsymbol{\xi}' \tag{3.5}$$

The fourth term, known as the differential source density, accounts for the generation of particles in the volume element [172]

Another form of transport equation which utilizes directional cosines with respect to the particle's direction is given by Seeger et al [172] as

$$\begin{aligned} \frac{1}{(\Omega_s + \Omega_a)}[\frac{1}{v}\frac{\partial\Psi(\mathbf{r}, \boldsymbol{\xi}, p; t)}{\partial t} &+ cos(\theta)\frac{\partial\Psi(\mathbf{r}, \boldsymbol{\xi}, p; t)}{\partial z}] + \Psi(\mathbf{r}, \boldsymbol{\xi}, p; t) \\ &= \int \frac{\Omega_s(p')}{\Omega_s(p')} \oint \frac{\Omega_s(\boldsymbol{\xi}' \rightarrow \boldsymbol{\xi}, p' \rightarrow p)}{\Omega_s(p)} \\ &\times \Psi(\mathbf{r}, \boldsymbol{\xi}', p'; t)d^2\boldsymbol{\xi}dp' \end{aligned} \tag{3.6}$$

References [45, 102] give further applications for equation (3.6).

3.2 Momentum scattering and slowing down density

The probability of positron's momentum scattering is given by [171]

$$g_p(p' \rightarrow p) = \frac{\Omega_s(p' \rightarrow p)}{\Omega_s(p)} \tag{3.7}$$

where p' is the initial value of the particle's momentum. It is evident that the scattererd energy and momentum can only be less than the initial value. Therefore

$$g_p(p' \rightarrow p) = 0, \forall p > p' \tag{3.8}$$

It is also apparent that the minimum value of the scattered momentum is $\beta p'$, where $\beta \in (0, 1)$ [172]. Therefore for

$$g_p(p' \rightarrow p) \neq 0, \forall p \in [\beta p', p'] \tag{3.9}$$

the change of positron's momentum from p' to p'' is less than p following the scattering, is given by [172]

$$H(p', p) = \int_{\beta p'}^{p} g_p(p' \rightarrow p'')dp'' \tag{3.10}$$

and the properties of $H(p', p)$ are [172, 171];

- the differential probability,$\frac{\partial H(p',p)}{\partial p}$ is given by equation 3.8
- for $\frac{p}{\beta}$, H vanishes
- for $p' = p$, $H = 1$

The average logarithmic loss per collision, ζ_p, is given as [171, 172]

$$\zeta_p =< ln(\frac{p}{p_o}) - ln(\frac{p'}{p_o}) >_{p'} \tag{3.11}$$

where p_o is an arbitrary reference momentum.

After considering the first bullet of the properties of H, equation 3.11 can then be expressed as [172]

$$\zeta_p = \int_{\ln \beta p}^{\ln p} H(p', p)dlnp' \tag{3.12}$$

The quantity of positrons in a unit volume that eventually have momentum magnitudes less than p per second is interpreted as the slowing down density Υ given by [172]

$$\Upsilon(\mathbf{r},p;t)=\int_{p}^{\frac{p}{\beta}}\frac{\Omega_s(p')}{[\Omega_s(p')+\Omega_a(p')]}H(p',p)\Psi(\mathbf{r},p';t)dp' \tag{3.13}$$

Upon integrating over all directions, the transport equation can then be expressed as [172]

$$\begin{aligned}\frac{\partial\Upsilon(\mathbf{r},p;t)}{\partial p} &- \frac{1}{\Omega_s(p)+\Omega_a(p)}\\ &\times [\frac{1}{v}\frac{\partial\Psi(\mathbf{r},p;t)}{\partial t}+\Omega_s(p)\Psi(\mathbf{r},p;t)]+S(\mathbf{r},p;t)\\ &= \frac{1}{\Omega_s(p)+\Omega_a(p)}\oint\boldsymbol{\xi}\bullet\boldsymbol{\nabla}\Psi(\mathbf{r},\boldsymbol{\xi},p,;t)d^2\boldsymbol{\xi}\end{aligned} \tag{3.14}$$

3.3 Narrow collision interval

The collision interval,β, has a range $0\leq\beta<1$ as was shown earlier. When β is close to 1 , the change in the momentum between successive scattering event intervals do not show much appreciable difference. This means that βp is close to p. If we consider the narrow collision interval in which a positron has a probability to alter its momentum from p_1 to p_2 after scattering, then we may, for a narrow collision interval, write [171, 172]

$$H(p_1,p_2)=H(\ln(\frac{p_1}{p_2})) \tag{3.15}$$

so that $H(p_1,p_2)$ appears as dimensionless.

By substituting equation (3.15) into equation (3.12), the average logarithmic loss per collision, after replacing p_2 by p_1, becomes

$$\begin{aligned}\zeta &= \int_{p_1=p_1}^{p_1=p_2} \frac{1}{p_1} H(p_1,p_2)dp_1 \\ &= \int_{lnp_1=lnp_1}^{lnp_1=lnp_2+ln\frac{1}{\beta}} H(p_1,p_2)dlnp_1 \end{aligned} \tag{3.16}$$

In the limit as $\beta \rightarrow 1$, the only quantity that changes appreciably in equation (3.13) is $H(p_1,p_2)$ and the slowing down density, in the limit as $\beta \rightarrow 1$ can be expressed as [172]

$$\Upsilon(\mathbf{r},p;t) = \frac{\Omega_s(p)\Psi(\mathbf{r},p;t)}{\Omega_s(p)+\Omega_a(p)} p\zeta_p \tag{3.17}$$

3.4 Sample-integrated quantities

Equation (3.14) can be simplified through the employment of the identity [172]

$$\boldsymbol{\nabla} \bullet \Psi(\mathbf{r},\boldsymbol{\xi},p;t)\boldsymbol{\xi} = \boldsymbol{\xi} \bullet \boldsymbol{\nabla}\Psi(\mathbf{r},\boldsymbol{\xi},p;t) \tag{3.18}$$

and integrate over the entire sample's volume and use Gauss' theorem to obtain

$$\int_V \boldsymbol{\nabla} \bullet \boldsymbol{\nabla} \bullet \Psi(\mathbf{r},\boldsymbol{\xi},p;t)\boldsymbol{\xi} d\tau \tag{3.19}$$

Then equation (3.14) becomes [171, 172]

$$\begin{aligned}\frac{\partial \Upsilon(\mathbf{r},p;t)}{\partial p} &- \frac{1}{\Omega_s(p)+\Omega_a(p)} \times [\frac{1}{v}\frac{\partial \Psi(\mathbf{r},p;t)}{\partial t} + \Omega_a(p)\Psi(\mathbf{r},p;t)] + S(\mathbf{r},p;t) \\ &= \frac{1}{\Omega_s(p)+\Omega_a(p)} \oint \Big\{ \int\int \Psi(\mathbf{r},\boldsymbol{\xi},p;t)\boldsymbol{\xi} \bullet d^2A \Big\} d^2\boldsymbol{\xi} \end{aligned} \tag{3.20}$$

Since the right-hand side of equation (3.20) is space independent, owing to the surface integral, we can rewrite equation (3.20) as [172, 171]

$$\begin{aligned}\frac{\partial\Upsilon(p;t)}{\partial p} &- \frac{1}{\Omega_s(p)+\Omega_a(p)} \\ &\times [\frac{1}{v}\frac{\partial\Psi(p;t)}{\partial t}+\Omega_a(p)\Psi(p;t)]+S(p;t) \\ &= \frac{1}{\Omega_s(p)+\Omega_a(p)}\oint\Big\{\int\int\Psi(\mathbf{r},\boldsymbol{\xi},p;t)\boldsymbol{\xi}\bullet d^2A\Big\}d^2\boldsymbol{\xi} \qquad (3.21)\end{aligned}$$

where d^2A are the surface element vectors of the sample. The event rate density Ψ in equation (3.20) can be removed if we make use of equation (3.17) and Laplace transform, then the resulting equation with respect to time is obtained as [172]

$$\frac{\partial\hat{\Upsilon}(p;\eta)}{\partial p}-\frac{\Omega_s(p)+(\frac{\eta}{v})\hat{\Upsilon}(p;\eta)}{p\zeta_p(p)\Omega_s(p)}+\hat{S}(p;\eta)+n(p;0)=0 \qquad (3.22)$$

The general solution of equation (3.22) is

$$\begin{aligned}\hat{\Upsilon}(p;\eta) &= exp(\eta\int\frac{dp}{pv\zeta_p(p)\Omega_s(p)}+\int\frac{\Omega_a(p)dp}{p\zeta_p(p)\Omega_s(p)}) \\ &\times \Big\{C-\int\hat{S}(p;\eta)+\eta(p,0^+)\,exp(-\int\frac{\Omega_a(p')+\frac{\eta}{v}}{p'\zeta_p(p')}dp')dp\Big\} \qquad (3.23)\end{aligned}$$

where C is a constant resulting from indefinite integration.

Suppose at time t=0, the number of particles/positrons m_o have constant linear momentum given by p_o. If we utilize the condition $m_o\delta(p-p_o)$ which is identical to the number of particles at t=0, then the p-integration yields a constant that is included in the integration constant C. Equation (3.23) reduces to

$$\begin{aligned}\hat{\Upsilon}(p;\eta) &= Cexp[-\int_{p'=p}^{p_o}\int\frac{\Omega_a(p')dp'}{p'\zeta_p(p')}] \\ &\times exp[-\eta\int_{p'=p}^{p_o}\frac{dp'}{p'v\zeta_p\Omega_s(p')}] \qquad (3.24)\end{aligned}$$

By using equations (3.2) and (3.17) we obtain the average number of positrons having the same momentum p given by [172]

$$n_{av}(p,t) = \frac{C}{\Omega_s(p)v(p)p\zeta_p} exp(-\frac{1}{\tau_{av}} f(p))\delta(t - f(p)) \tag{3.25}$$

where $f(p)$ is a function related to the time it takes for the positron to alter the momentum from p_o to p.

For average narrow collision interval, we have

$$\zeta_p = -\frac{1}{p}(p)_s\tau_s \tag{3.26}$$

where $(p)_s$ is the rate at which momentum is lost due to scattering and τ_s the mean time between scatterings.

Finally, the sample-averaged number of particles can be written as [172]

$$n_{av} = \frac{n_o}{(dp/dt)_s} exp(-\frac{t}{\tau_{av}}\delta(t - f(p)) \tag{3.27}$$

with

$$\begin{aligned} f(p) &= \int_{p_o}^{p} \frac{dp'}{(dp'/dt)_s} \\ &= \int_{p_o}^{p} dp'(\frac{dp'}{dt})_s^{-1} \end{aligned} \tag{3.28}$$

Age-momentum correlation (AMOC) analysis utilizes equation (3.27) for positroniums that are formed with energies greater than $3k_BT/2$ [182].

Chapter 4

Diffusion and trapping

Thermalized positrons with energies

$$\frac{3k_BT}{2} \tag{4.1}$$

begin to behave as charged particles and these positrons spend most of their time in the regions in the bulk region (interstitial) because of the repulsive nuclear core of ions. When thermal equilibrium of a positron with the material is reached, the dominant scattering is due to phonons. Soininen et al [180] showed that at low to medium temperatures (between 10 K and 500 K) the positron scatterings with longitudinal acoustic phonons varies as $T^{-1/2}$ but at elevated temperatures above 500 K, the deviation from the trend indicates the onset of optical phonon scattering. Other types of scattering, for example by electrons and impurities, are ineffective compared to the phonon scattering [21] and the motion of the positron is nearly a random walk in all directions [125]. The analysis of positron's slowing down and diffusion takes into account the spatial distribution and linear momentum of positron as having random probability distribution given by the distribution function $f(\mathbf{r}, \mathbf{p}, t)$ [146].

4.1 Positron diffusion equation

When positrons are in thermal balance with the material means that the energy and momentum no longer depend on time. In general, a distribution of positrons in a material, once thermal balance of positron with the material is reached, is given by [146]

$$\begin{aligned} \frac{\partial f(\mathbf{r},\mathbf{t})}{\partial t} &= D_+ \boldsymbol{\nabla}^2 f(\mathbf{r},\mathbf{t}) - [\lambda_{\mathbf{b}} + \kappa(\mathbf{r})]\mathbf{f}(\mathbf{r},\mathbf{t}) \\ &\quad -\boldsymbol{\nabla} \bullet [v_d(\mathbf{r}) f(\mathbf{r},t)] + f_i(\mathbf{r},t) \end{aligned} \tag{4.2}$$

where D_+ and v_d are the coefficient of diffusion and the drift speed of positron, respectively and $\kappa(\mathbf{r})$ the rate at which positron is trapped in a defect [146].

The diffusion coefficient can be calculated from the microscopic quantum mechanical theory provided scattering processes are known [124, 65]. The average length travelled by a positron between successive scatterings $< l >$ can be obtained from the semiclassical random-walk theory and is temperature-dependent [146]

$$< l >= \frac{3D_+}{\sqrt{< v^2 >}} \tag{4.3}$$

with

$$< v^2 >= \frac{3k_B T}{\mu} \tag{4.4}$$

where $< v^2 >$ is the thermal average positron velocity, k_B the Boltzmann constant and μ the reduced positron mass. From equation (4.3), the diffusion constant can be written as [146]

$$D_+ = \frac{< v^2 >^{1/2} < l >}{3}$$

$$\begin{aligned} &= \frac{< v^2 >^{1/2} < v^2 >^{1/2} < l >}{3 < v^2 >^{1/2}} \\ &= \frac{< v^2 > \tau}{3} \end{aligned} \tag{4.5}$$

where τ is the relaxation time.

The time-independent diffusion equation becomes [146]

$$D_+ \boldsymbol{\nabla}^2 f(\mathbf{r}) - [\lambda_b + \kappa(\mathbf{r})] f(\mathbf{r}) - \boldsymbol{\nabla} \bullet [v_d(\mathbf{r}) f(\mathbf{r})] + f_i(\mathbf{r}) = 0 \tag{4.6}$$

with initial condition

$$f(\mathbf{r}, 0) = I(\mathbf{r}) \tag{4.7}$$

where $I(\mathbf{r})$ is the implantation profile.

The second term of equation (4.6) refers to the effective annihilation rate in the delocalized state. Therefore

$$\begin{aligned} \lambda_b + \kappa(\mathbf{r}) &= \lambda_{eff} \\ &= \frac{1}{\tau_{eff}(\mathbf{r})} \end{aligned} \tag{4.8}$$

The trapping rate is directly proportional to the quantity of defects but also depends on the nature of defects. For positron diffusion to occur, certain conditions must be satisfied, namely

- Maxwell-Boltzmann distribution must be obeyed by the positron momentum distribution.
- the scattering of positrons has to be isotropic and quasielastic
- sample layer thickness or a defect zone has to be large enough [87].

Equation (4.2) in one dimension has the following form

$$\frac{\partial f(z)}{\partial t} = D_+ \frac{\partial^2 f}{\partial z^2} + v_d \frac{\partial f}{\partial z} - [\lambda + \kappa_d(z)] f(z) \tag{4.9}$$

For time-independent equation (4.9) reduces to

$$0 = D_+ \frac{\partial^2 f}{\partial z^2} + v_d \frac{\partial f}{\partial z} - [\lambda + \kappa_d(z)] f(z) \tag{4.10}$$

The function $f(z)$ obeys the following boundary conditions [146]:

- the positron density must rapidly decrease in the sample far away from the sample's entry surface.
- for the first two terms on the right hand side of equation 4.9, continuity of current density has to be maintained especially through the surface of the sample.

The variation of positron depth distribution leads to non-steady state diffusion-trapping equation in which case

$$\frac{\partial f(z)}{\partial t} \neq 0 \tag{4.11}$$

in equation (4.7) [28]. Frieze et al. [66] has found the solution for diffusion equation (4.2) through the utilization of eigenfunctions for spatially arranged vacancies. The diffusion equation, given by equation (4.2) has also been solved for two groups (thermal and epithermal) by [27, 146] in which Green's function is utilized

$$f(z,t) = \int_0^\infty G(z|x,t) P(x) dx \tag{4.12}$$

where $G(z|x,t)$ is the Green's function given by [146]

$$G(z|x,t) = e^{-\lambda_{eff}t}\frac{1}{\sqrt{4\pi D_+ t}}[e^{-(x-z)^2/(4D_+t)} + e^{-(x+z)^2/(4D_+t)} - \frac{\mu}{D_+}e^{(\frac{\mu}{D_+})(x+z+\mu t)}erfc[\frac{x+z}{\sqrt{4D_+t}} + \mu[\sqrt{\frac{t}{D_+}}]]] \quad (4.13)$$

where μ is the rate at which positrons escape via interface.

Annihilation rates are then calculated as [27, 146]

$$N(t) = \lambda_b f_b(t) + \lambda_s f_s(t) + \lambda_{ps} f_{ps}(t) \quad (4.14)$$

where $f_b(t)$, $f_s(t)$ and f_{ps} refer to the fraction of positrons in the defect-free region in the bulk, the fraction of positrons at the surface and the fraction of para-positronium (pPs), respectively. λ_i are the annihilation rates.

Slow positron beam experimental results are usually analyzed using the diffusion-equation approach [194].

4.1.1 Positron diffusion coefficient

In semiconductors, the scattering by longitudinal acoustic phonons is the most crucial process and this process leads to the diffusion coefficient which does vary with temperature. The calculation is carried out through the utilization of deformed-potential approximation [16, 180] in which the relaxation-time is

$$\tau_{ph} = (\sqrt{\frac{8\pi}{9}})\frac{\frac{h^4 s}{(2\pi)^4}}{(m^*)^{3/2}(k_B T)^{3/2}\gamma} \quad (4.15)$$

where s refers to the speed of sound and γ the positron-phonon coupling constant.

The coupling constant can be obtained by knowing the deformation potential and elastic constants $< c_{ii} >$. Typical values of positron-phonon coupling constant for various materials are 583, 478 and 307 for Al, Ag and Cu respectively [150]. The diffusion coefficient is then given by

$$\begin{aligned} D_+ &= \tau_{ph}\frac{k_B T}{m^*} \\ &= (\sqrt{\frac{8\pi}{9}})\frac{\frac{h^4}{(2\pi)^4} < c_{ii} >}{(m^*)^{5/2}(k_B T)^{1/2}E_d^2} \end{aligned} \tag{4.16}$$

At elevated temperatures, optical phonon scattering have non-negligible contribution according to [180] and it is clear that the diffusion is highly reduced by high levels of impurities.

The effective positron mass m^* estimate falls in the range 1.3 to $1.7m_e$ [167]. The effect of phonon scattering on the effective positron mass results in a non-symmetry Doppler broadening of positron-electron annihilation momentum distribution [120, 146].

4.2 Positron trapping into defects

The potential experienced by a positron at open-volume defect in a material is greatly reduced mainly because of a decrease in the repulsion force by the nucleus. Therefore, a delocalized positron can have a larger energy eigenvalue than a localized positron in a defect and during a transition from bulk to a defect, the excess amount of energy is transferred to the material [146]. Open-volume defects and larger defects do trap positrons in sites where the density of ions is depleted [74] and also in negative vacancies in semiconductors [161, 146].

4.2.1 Positron trapping models

Positron trapping in solids has the following conditions [146]:

- the probability that positrons are trapped during thermalization is not significant
- the distribution of defects in the sample under investigation is homogeneuos and
- there is no interaction between defects.

4.2.1.1 Positron trapping by a single-type defect

Positrons, after thermalization, can annihilate in a defect-free bulk of the sample with annihilation rate λ_b or in open-volume defects provided defect concentration is high enough. A typical trapping model scheme is shown in figure 4.1.

The electron density in such a defect is reduced and the annihilation rate in localized states is smaller than in delocalized states [146]. Single-type defect model is represented by equations (4.17) and (4.18) [104]

$$\frac{df_b}{dt} = -\lambda_b f_b - \kappa_d f_b + f_i \tag{4.17}$$

$$\frac{df_d}{dt} = -\lambda_d f_d + \kappa_d f_b \tag{4.18}$$

where f_b, f_d are probabilities that positrons in the bulk and defect at time t respectively. λ_b and λ_d are the annihilation rates in bulk and in defect, respectively and f_i refers to the source term. The decay spectrum of positrons is obtained from solving equations (4.17) and (4.18) and is given by equation (4.19).

$$D(t) = I_1 e^{-(\lambda_b+\lambda_d)t} + I_2 e^{-\lambda_d t} \tag{4.19}$$

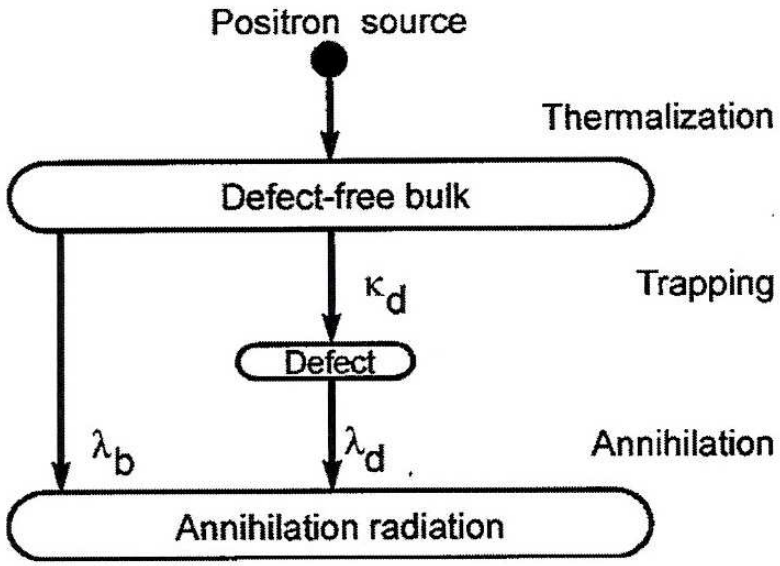

Figure 4.1: Single-type defect model for positron trapping. Annihilation of positron with electron occurs both in a defect-free region and in a defect resulting in two positron lifetime components [104].

where I_1 and I_2 are respectively the corresponding intensities of bulk and defect positron lifetime components, given by [146]

$$I_1 = 1 - I_2 \tag{4.20}$$

and

$$I_2 = \frac{\kappa_d}{\lambda_b - \lambda_d + \kappa_d} \tag{4.21}$$

In the kinetic trapping model [146], the trapping rate κ_d is given by

$$\kappa_d = \mu C \tag{4.22}$$

where μ and C are the trapping coefficient and defect concentration, respectively. It is also worth noticing that the trapping rate is temperature-dependent and also depends on the doping fluencies in materials e.g. in P-doped Si [146]. Positron lifetime spectra, once obtained, are fitted with the sum of decaying components after implementing proper source correction and background subtraction [146]. In the two component fit (according to a single type defect model), the model function is given by

$$\frac{dN(t)}{dt} = -N_o\left(\frac{I_1}{\tau_1}e^{-\frac{t}{\tau_1}} + \frac{I_2}{\tau_2}e^{-\frac{t}{\tau_2}}\right) \tag{4.23}$$

where N_o is the total number of positrons present at time $t = 0$, and τ_1 and τ_2 are defined as

$$\frac{1}{\tau_1} = \frac{1}{\tau_b} + \kappa_b \tag{4.24}$$

$$\tau_2 = \tau_d \tag{4.25}$$

The average positron lifetime τ is given as [146]

$$\tau = \sum_{i=1}^{k+1} I_i \tau_i \tag{4.26}$$

If the values of τ_b and τ_d are known, the rate at which positrons are trapped can be extracted from the mean positron lifetime τ as [146]

$$\begin{aligned} \kappa_d &= \frac{1}{\tau_b} \frac{\tau - \tau_b}{\tau_d - \tau} \\ &= \frac{\eta}{\tau_b(1-\eta)} \end{aligned} \tag{4.27}$$

where the parameter η represents the annihilation fraction given by

$$\begin{aligned} \eta &= \int_0^\infty n_d(t) dt \\ &= \frac{\kappa_d}{\lambda_b + \kappa_d} \end{aligned} \tag{4.28}$$

4.2.1.2 Positron trapping in different independent defect types

Consider several independent defect types in which two are independent open-volume defects and one shallow positron trap with detrapping rate σ. The model is shown in figure 4.2. The model has been successfully applied to materials e.g. in n-doped GaAs [104, 103]

The rate equations are [104, 103]

$$\frac{dN_b(t)}{dt} = -(\lambda_b + \kappa_{d1} + \kappa_{d2}) N_b(t) \tag{4.29}$$

$$\frac{dN_{d1}(t)}{dt} = -(\lambda_{d1} + \sigma) N_{d1}(t) + \kappa_{d1} N_b(t) \tag{4.30}$$

$$\frac{dN_{d2}(t)}{dt} = -\lambda_{d2} N_{d2}(t) + \kappa_{d2} N_b(t) \tag{4.31}$$

$$\frac{dN_{d3}(t)}{dt} = -\lambda_{d3} N_{d3}(t) + \kappa_{d3} N_b(t) \tag{4.32}$$

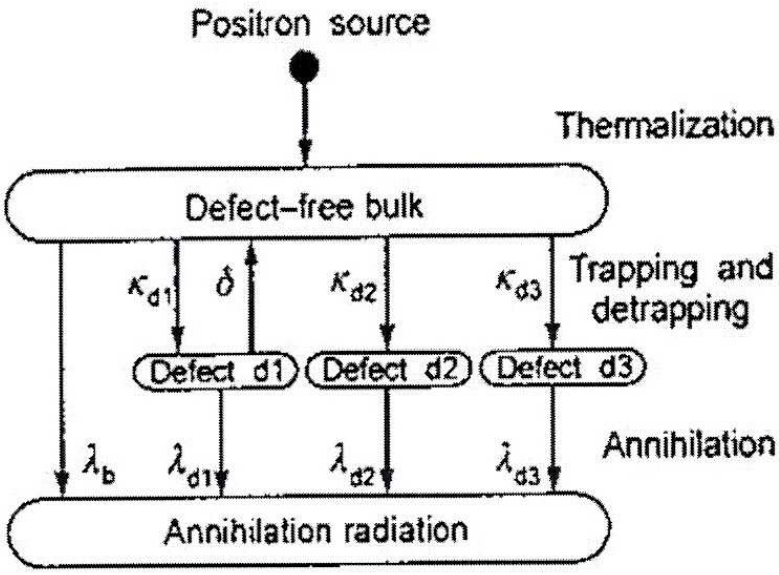

Figure 4.2: Trapping model for more than a single-type defect [104].

Shallow positron trap corresponds to a defect d1 while d2 and d3 are considered as open volume defects. k+1 lifetime components correspond to k defects. The corresponding lifetime components from equation (4.29) to (4.32) are [104]

$$\tau_1 = \frac{2}{\Xi + \Upsilon} \tag{4.33}$$

$$\tau_2 = \frac{2}{\Xi - \Upsilon} \tag{4.34}$$

$$\tau_3 = \frac{1}{\lambda_{d2}} \tag{4.35}$$

$$\tau_4 = \frac{1}{\lambda_{d3}} \tag{4.36}$$

Intensities are

$$I_1 = 1 - (I_2 + I_3 + I_4) \tag{4.37}$$

where

$$\begin{aligned} I_2 &= \frac{\sigma + \lambda_{d1} - \frac{1}{2}(\Xi - \Upsilon)}{\Upsilon} \\ &\times \left[1 + \frac{\kappa_{d1}}{\sigma + \lambda_{d1} - \frac{1}{2}(\Xi - \Upsilon)} + \frac{\kappa_{d2}}{\lambda_{d2} - \frac{1}{2}(\Xi - \Upsilon)} + \frac{\kappa_{d3}}{\lambda_{d3} - \frac{1}{2}(\Xi - \Upsilon)}\right] \end{aligned} \tag{4.38}$$

$$I_3 = \frac{\kappa_{d2}(\sigma + \lambda_{d1} - \lambda_{d2})}{[\lambda_{d2} - \frac{1}{2}(\Upsilon + \Xi)][\lambda_{d2} - \frac{1}{2}(\Xi - \Upsilon)]} \tag{4.39}$$

$$I_4 = \frac{\kappa_{d3}(\sigma + \lambda_{d1} - \lambda_{d3})}{[\lambda_{d3} - \frac{1}{2}(\Upsilon + \Xi)][\lambda_{d3} - \frac{1}{2}(\Xi - \Upsilon)]} \tag{4.40}$$

and [103]

$$\Xi = \lambda_b + \kappa_{d1} + \kappa_{d2} + \kappa_{d3} + \lambda_{d1} + \sigma \tag{4.41}$$

$$\Upsilon = \sqrt{(\lambda_b + \kappa_{d1} + \kappa_{d2} + \kappa_{d3} - \lambda_{d1} - \sigma)^2 + 4\sigma\kappa_{d1}} \tag{4.42}$$

The average positron lifetime is given by equation (4.26).

4.3 Positron trapping in semiconductors

The energy gap, the Fermi gap, is a critical factor for electron-hole excitation. The charged states are analyzed [145] by adding a Coulomb tail [146]

$$V_c = \frac{Q}{Er} \tag{4.43}$$

to the defect potential well. Q refers to the charge localized at the defect and E is the zero-frequency dielectric constant. The Coulomb tail has to be modified by truncation in consideration of the delocalization of the charge. The potential models are shown in figure 4.3

The trapping coefficient for various defect charge states are shown in figure 4.4 [145].

The dependency of trapping coefficients on temperature gives crucial information about the charge of defect [145]

The temperature dependent statistical distribution provides the trapping coefficients, $\beta(T)$ as [146]

$$\beta(T) = \frac{2}{\pi^{1/2}(k_B T)^{3/2}} \int_0^\infty dE\nu(p = \sqrt{2m^* E} e^{-\frac{E}{k_B T}} \sqrt{E} \tag{4.44}$$

The integral in equation (4.44) is proportional to T which means that the temperature-dependent trapping coefficient depends on the square root of T.

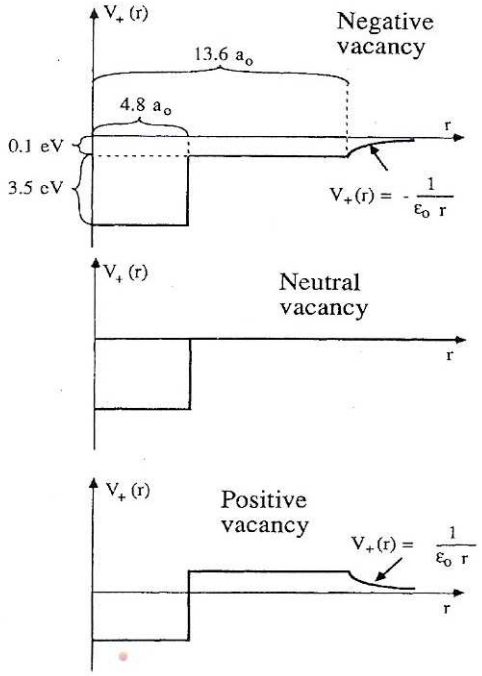

Figure 4.3: The positron potentials at different charge vacancies in silicon. The Coulomb potential is truncated at $r = 13.6a_o$ because of delocalization of the charge [104].

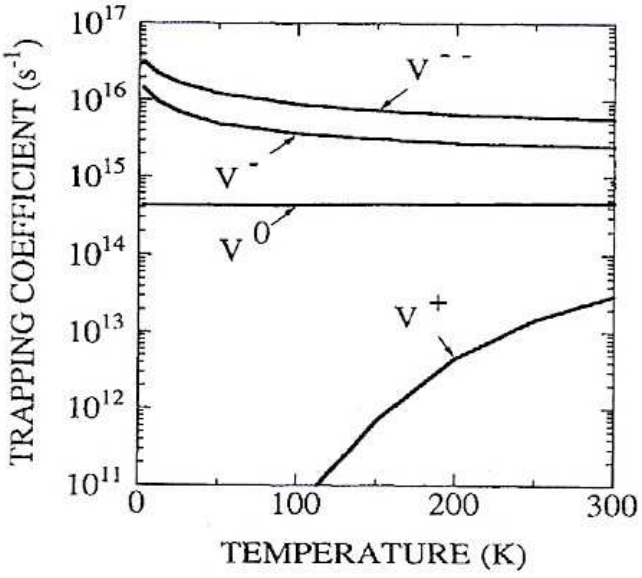

Figure 4.4: Positron trapping coefficient as a function of temperature for singly positive (V^+), neutral (V^o), singly negative (V^-) and doubly negative (V^{--}) vacancies [145, 146].

Chapter 5

Theoretical framework of positron-matter interaction

5.1 Two-component Density Functional theory

Density Functional theory (DFT), based on the work by Hohenberg et al [81] and Kohn et al [100], can be generalized to also include, not only electrons, but also positrons [92]. The theory then becomes known as Two-component Density Functional theory [44, 128, 24, 110]. The local density approximation (LDA), which is part of DFT, is the commonly used theory and relies on the results from the homogeneous electron gas. Investigation of positron annihilation in solids requires that positron annihilation rates in various densities on homogeneous gas are found and this requires the utilization of LDA although in some instances the LDA is modified to achieve reasonable annihilation rates.

5.1.1 Generalized Kohn-Sham method

In the Kohn-Sham method, the calculation of the ground-state electron and positron densities minimizing $E(\rho_-, \rho_+)$, the ground state energy for both positrons

and electrons [24], demands the solving of Schrodinger equation for positrons separately from Schrodinger equation for electrons [146] as

$$-\frac{1}{2}\nabla^2\psi_i + [\frac{\delta E_{xc}(\rho_-)}{\delta\rho_-(\mathbf{r})} - \phi(\mathbf{r}) + \frac{\delta \mathbf{E^{e-p}}(\rho_+,\rho_-)}{\delta\rho_-(\mathbf{r})}]\psi_\mathbf{i}(\mathbf{r}) = \epsilon_\mathbf{i}\psi_\mathbf{i}(\mathbf{r}) \tag{5.1}$$

$$-\frac{1}{2}\nabla^2\psi_i^+ + [\frac{\delta E_{xc}(\rho_+)}{\delta\rho_+(\mathbf{r})} + \phi(\mathbf{r}) + \frac{\delta \mathbf{E^{e-p}}(\rho_+,\rho_-)}{\delta\rho_+(\mathbf{r})}]\psi_\mathbf{i}^+(\mathbf{r}) = \epsilon_\mathbf{i}^+\psi_\mathbf{i}^+(\mathbf{r}) \tag{5.2}$$

where

$$\phi(r) = \int d\mathbf{r}^{'}\frac{-\rho_-(\mathbf{r}^{'}) + \rho_+(\mathbf{r}^{'}) + \rho_\mathbf{o}(\mathbf{r}^{'})}{\mathbf{r}-\mathbf{r}^{'}} \tag{5.3}$$

refers to the Coulomb potential [146] and $\rho_o(\mathbf{r}^{'})$ is the charge density (positive) responsible for setting up the external potential V_{ext}.

The densities for positron and electron are obtained by adding over the occupied states [146],

$$\rho_-(\mathbf{r}) = \sum_{\epsilon_\mathbf{i}\leq\epsilon_\mathbf{f}} \mid \psi_\mathbf{i}(\mathbf{r})\mid^\mathbf{2} \tag{5.4}$$

$$\rho_+(\mathbf{r}) = \sum_{\mathbf{i}}^{\mathbf{N_+}} \mid \psi_\mathbf{i}^+(\mathbf{r})\mid^\mathbf{2} \tag{5.5}$$

where ϵ_f, $\psi_i(\mathbf{r})$ and $\psi_i^+(\mathbf{r})$ are the Fermi energy, electron wavefunction and positron wavefunction respectively. N_+ is the number of positrons.

5.1.2 Local-Density Approximation (LDA)

If we are to utilize the two-component density functional (TCDF), for both electrons and positrons, we need to use LDA as an effective procedure for electronic structure and more importantly the exchange correlation energy given by [146]

$$E_{exc}[\rho] = \int d\mathbf{r}\rho(\mathbf{r})\epsilon_{\mathbf{xc}}(\rho(\mathbf{r})) \tag{5.6}$$

where ϵ_{xc} is the exchange-correlation energy for a spin unpolarized particle in a uniform one-component electron gas of density ρ. In equations (5.1) and (5.2), the exchanged-correlation potential, $\mu_{xc}(p)$ is given by [146]

$$\begin{aligned} \mu_{xc}(\rho) &= \frac{\delta E_{xc}(\rho)}{\delta\rho(\mathbf{r})} \\ &= \frac{\partial(\rho\epsilon_{xc}(\rho))}{\partial\rho} \end{aligned} \tag{5.7}$$

The exchange correlation energy functional $\epsilon_{xc}(\rho)$ for a homogeneous electron gas (HEG) use the Monte Carlo simulation [40]. The parametrization of ϵ_{xc} is obtained using the approach by Perdew and Zinger [139] and [138]. Using [146]

$$a_x = \frac{3}{4}\sqrt[\frac{2}{3}]{\frac{3}{2\pi}} \tag{5.8}$$

the exchange-correlation energy per electron for $r_s > 1$ is

$$\epsilon_{xc} = -\frac{a_x}{r_s} - \frac{0.1423}{1 + 1.0529\sqrt[2]{r_s} + 0.3334r_s} \tag{5.9}$$

and for $r_s < 1$,

$$\epsilon_{xc} = -\frac{a_x}{r_s} + 0.0311lnr_s - 0.0480 + 0.0020r_s lnr_s - 0.0116r_s \tag{5.10}$$

where r_s represents the radius of a spherical volume of the same magnitude as the volume per electron.

The electron-positron correlation energy

$$E_c^{e-p}(\rho_+, \rho_-) \tag{5.11}$$

is calculated, taking into account the vanishing positron density in a uniform electron gas [146, 11, 12, 13]. Lantto [106] calculated positron and electron density ratios and these were employed by Boronski and Nieminen [24] with one condition that the symmetry of E^{e-p} be maintained for both electron and positron densities [146].

The overlap of positron and electron densities is proportional to the positron annihilation rate [146],

$$\lambda = \pi r_o^2 c \int \rho_+(\mathbf{r}) \rho_-(\mathbf{r}) g(0; \rho_+, \rho_-) d\mathbf{r} \tag{5.12}$$

where r_o and g are the classical radius of the electron and positron-electron correlation function, respectively.

Local densiy approximation has a tendency of giving overestimated annihilation rates and therefore a generalized gradient approximation is usually employed as a corrective measure to rectify this overestimation [15, 146]

5.1.3 Delocalized positron states

The positron density in a defect-free crystal is negligible and can be excluded in solving Kohn-Sham equations (5.1) and (5.3). This also involves the exclusion of $e^+ - e^-$ correlation potential [146]

$$\frac{\delta E_c^{e-p}(\rho_+, \rho_-)}{\delta \rho_-(\mathbf{r})} \tag{5.13}$$

The sum of the correlation potential V_{corr} and Coulomb potential ϕ form a foundation for the potential which is experienced by a positron [146]

$$V_{+}(\mathbf{r}) = \mathbf{V_{corr}}(\rho(\mathbf{r})) + \phi(\mathbf{r}) \tag{5.14}$$

Numerous calculations have been performed for this system [11, 12] and the parametrized form of V_{corr} was done by Nieminen [128]. For homogeneous electron gas characterized by $r_s \leq 0.302$ (high electron density), one obtains

$$V_{corr}(r_s) = -\frac{1.56}{\sqrt{r_s}} + (0.051 lnr_s - 0.081) lnr_s + 1.14 \tag{5.15}$$

For $0.302 \leq r_s \leq 0.56$

$$V_{corr}(r_s) = -0.92305 - \frac{0.05459}{r_s^2} \tag{5.16}$$

For $0.56 \leq r_s \leq 8.0$

$$V_{corr}(r_s) = -\frac{13.15111}{r_s + 2.5} + \frac{2.8655}{r_s + 2.5} - 0.6298 \tag{5.17}$$

and for low electron density $r_s \geq 8.0$ [146]

$$V_{corr}(\rho_{-}) = 186.4207\rho_{-} - 179856.27\rho_{-}^2 - 0.524 \tag{5.18}$$

Figure 5.1 shows how the correlation energy varies with parameter r_s [146]
The zero-positron density limit is referred to as the enhancement factor [146] of the electron-density at the positron and is denoted by:

$$\gamma(\rho_{-}) \tag{5.19}$$

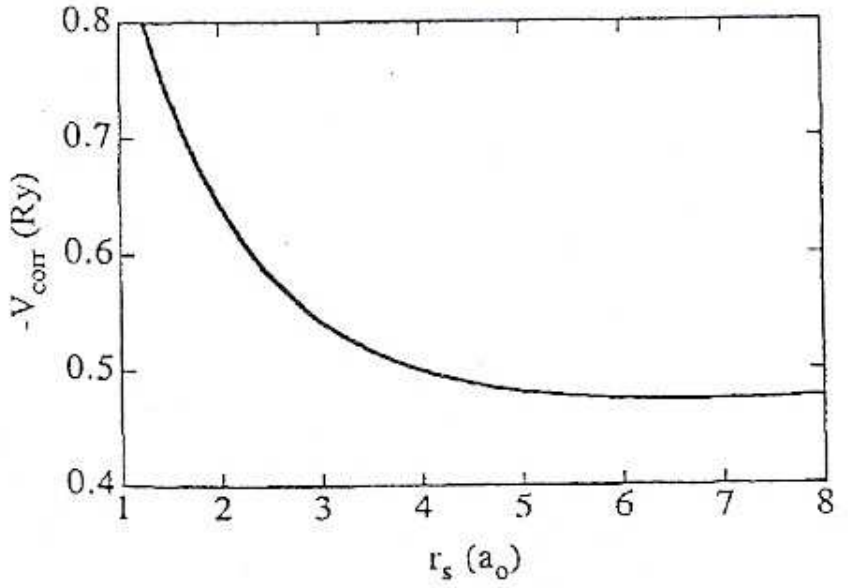

Figure 5.1: The variation of positron-electron correlation energy with parameter r_s [146, 11, 12, 24].

The annihilation rate is

$$\begin{aligned} \lambda &= \pi r_o c \int d\mathbf{r} \rho_+(\mathbf{r}) \gamma(\rho_-) \\ &= \int d\mathbf{r} \rho_+(\mathbf{r}) \mathbf{\Gamma}(\rho_-(\mathbf{r})) \end{aligned} \tag{5.20}$$

where $\Gamma(\rho_-(\mathbf{r}))$ is the annihilation rate in a homogeneous electronic gas with density ρ_-. $\Gamma(\rho_-(\mathbf{r}))$ [146] is given by the interpolation approach [24] based on many-body calculations [11]

$$\Gamma(\rho) = \pi r_o^2 cp(1 + 1.23r_s + 0.8295r_s^{3/2} - 1.26r_s^2 + 0.3286r_s^{5/2} + \frac{1}{6}r_s^3) \tag{5.21}$$

Figure 5.2 shows the relationship between $\Gamma(\rho_-)$ and electron gas density parameter r_s.

The results of Sterne et al [181] display a slightly changed parametrisation. They used

$$\Gamma(\rho) = \pi r_o^2 cp(1 + 0.1512r_s + 0.0048r_s^{3/2} - 2.01r_s^2 + 0.4466r_s^{5/2} + 0.1667r_s^3) \tag{5.22}$$

5.1.4 Localized positron states

Positron at lattice defects causes the mean density of electrons to increase around the defect and the screening effect can no longer be ignored [146]. The same procedure used for delocalized positrons is used for positrons at defects but this approach presents problems when the range of positron state in a defect becomes comparable to the short range screening cloud [146]. The calculations utilizing the two-component density functional performed by done by Puska et al [146], Nieminen et al [125] and Boronski et al [24] support the utilization of the con-

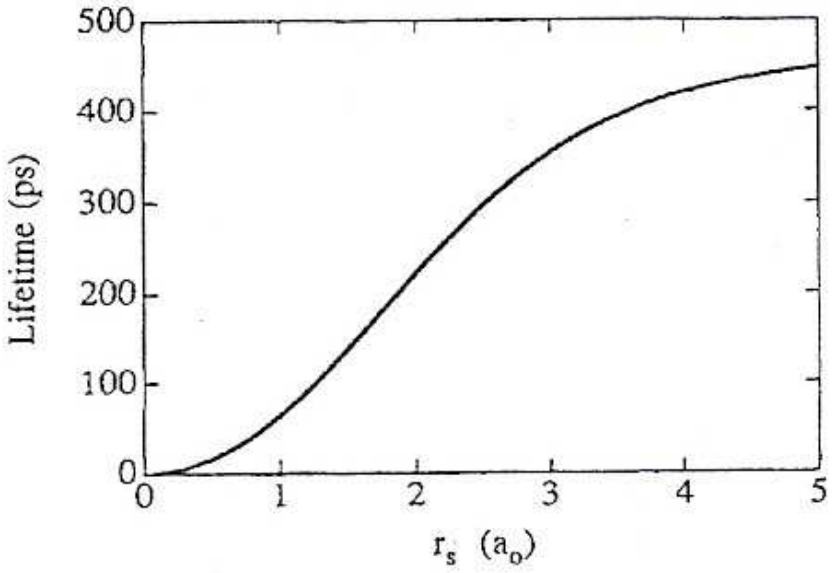

Figure 5.2: The positron lifetime in a homogeneous electron gas as a function of the electron gas density parameter r_s [24].

ventional approach since annihilation rates in these two procedures are the same. Therefore, we have [146]

$$\begin{aligned}[-\frac{1}{2}\nabla^2 - \int d\mathbf{r}\frac{\rho_-(\mathbf{r}') - \rho_o(\mathbf{r}')}{|\mathbf{r}-\mathbf{r}'|} & \\ + \frac{\delta E_c^{e-p}[\rho_+,\rho_-]}{\delta_{\rho_+}}]\psi^+(\mathbf{r}) & \\ = \epsilon^+\psi^+(\mathbf{r}) & \end{aligned} \tag{5.23}$$

which is the the positron's corrected version of Schrodinger's equation.

5.2 Positron states in semiconductors and insulators

The existence of the band gap in a dielectric and semiconductor materials affect the screening effect of positrons by electrons. The models for semiconductors lead to the annihilation rate in equation (5.20) [147] to be written as

$$\Gamma(\rho_-) = \pi r_o^2 cp(1+1.23r_s+0.8295r_s^{3/2}-1.26r_s^2+0.3286r_s^{5/2}+\frac{1}{6}(1-\frac{1}{\epsilon_\infty})r_s^3) \tag{5.24}$$

where ϵ_∞ is the high-frequency dielectric constant [146, 147].

The two constraints over equation (5.24) are:

- The electron density $\rho(\mathbf{r})$ at the site of positron ($\mathbf{r}=0$) obeys

$$\frac{\partial\rho_-}{\partial r}|_{r=0} = -\rho_-(0) \tag{5.25}$$

- The number of electrons $(1-\frac{1}{\epsilon_\infty})$ forming the screening cloud $\delta\rho_-(\mathbf{r})$ due a positron is given by

$$\int_0^\infty \delta\rho_-(\mathbf{r})4\pi r^2 dr = (1-\frac{1}{\epsilon_\infty}) \tag{5.26}$$

and this ensures the long-range potential to be proportional to

$$\frac{1}{\epsilon_\infty r} \tag{5.27}$$

Reduced screening effects on the correlation potential can be neglected but worth noting that the correlation potential scales can approximately be treated as [127]

$$(\lambda - \lambda_0)^{1/3} \tag{5.28}$$

where λ refers to the actual annihilation rate in the abscence of the enhancement factor.

The shielding effect of valence electrons in the insulator is further reduced because of wider band gaps. Puska et al [147] related polarizability of electrons in a dielectric material with the electron enhancement via Clausius-Mossotti relation given by

$$\alpha_{at} = \frac{3\Omega}{4\pi}\frac{\epsilon_\infty - 1}{\epsilon_\infty + 2} \tag{5.29}$$

where Ω is the unit-cell volume.

The annihilation rate is then given by [147, 146] as

$$\Gamma(\rho_-) = \pi r_o^2 c p_-(1 + A + B\Omega\frac{\epsilon_\infty - 1}{\epsilon_\infty + 2}) \tag{5.30}$$

where A and B are 0.684 and 0.0240 a_o^{-3} respectively, where a_o is the Bohr radius. These constants are the products of fitting the calculated annihilation rates of various insulators to rates obtained from experiments. Typical average positron lifetimes (reciprocals of annihilation rates) in an insulator and a semiconductor are 166 ps and 232 ps in GaAs and MgO respectively [147].

5.3 The momentum distribution of electron-positron pairs

The interaction of positrons with electrons in a condensed matter may provide a good foundation [53] to obtain electron-positron annihilation momentum distribution. The advantage of this approach is the utilization of a single particle wavefunction instead of charge densities as is the case in the DFT [147, 146].

In another approach, the positron wavefunction is obtained for the Coulomb potential as a result of core nuclear charge and electron density. The momentum distribution is thus given by [146, 172]

$$\rho(\mathbf{P}) = \sum_{\mathbf{i}} |\int \mathbf{dre^{iP.r}} \psi_{\mathbf{i}}^{\mathbf{ep}}(\mathbf{r}.\mathbf{r}^{'})|^{\mathbf{2}} \tag{5.31}$$

where $\mathbf{P}$ is the resultant momentum arising from positron-electron annihilation and $\psi_i^{ep}(\mathbf{r}, \mathbf{r}^{'})$ is the dual-particle wavefunction approximated as [146, 147]

$$\psi_i^{ep}(\mathbf{r}, \mathbf{r}^{'}) = \psi_+^o(\mathbf{r})\psi_i^o(\mathbf{r}^{'})\sqrt{g_i(\mathbf{r})} \tag{5.32}$$

where $\psi_+^o(\mathbf{r})$ and $\psi_i^o(\mathbf{r}^{'})$ are the wavefunctions for positrons and electrons in their occupied states$i$, respectively in the absence of $e^+ - e^-$ correlation effects [147]. The function $g_i(\mathbf{r})$ accounts for the deviation of positron wavefunction from ψ_+^o taking into account the enhancement of ρ_- at the positron for the electronic core and valence states i [147, 146]. The annihilation rate is then obtained by summing momenta [147]

$$\begin{aligned} \lambda &= \frac{\pi r_o^2 c}{(2\pi)^3} \int d\mathbf{P}\rho(\mathbf{P}) \\ &= \pi r_o^2 \int d\mathbf{r}_i \mid \int d\mathbf{r}\psi_i^{ep}(\mathbf{r}, \mathbf{r}^{'})|^{\mathbf{2}} \end{aligned} \tag{5.33}$$

The function $g_i(\mathbf{r})$ in equation 5.32 can be set to unity through the utilization of independent-particle model (IPM). It is important that we go beyond the approximation of independent-particle model and use the momentum-dependent enhancement factor [94, 95]

$$\epsilon(P, r_s) \tag{5.34}$$

for the homogeneous electron gas function [118]

$$g_{ki}(\mathbf{r}) = \epsilon(\sqrt{\epsilon_{ki}/\epsilon_F}k_F, r_s) \tag{5.35}$$

where ϵ_{ki} and ϵ_F are the electronic energy and Fermi energy, respectively. The spatial dependence can be introduced through the use of positron-dependent r_s parameter [52, 90]. If this is done, then

$$g_{ki}(\mathbf{r}) = \epsilon(\sqrt{\epsilon_{ki}/\epsilon_F}k_F, r_s(\mathbf{r})) \tag{5.36}$$

where

$$r_s(\mathbf{r}) = [4\pi\rho_-(\mathbf{r})/3]^{-1/3} \tag{5.37}$$

The correlation function in the framework of LDA, can also be utilized for inner electronic states well below the Fermi gap [146]. This is achieved through the modification of equation 5.36 in which ϵ_{ki} is equated to zero [51, 53]. Therefore equation 5.36 can be written as

$$g_{ki}(\mathbf{r}) = \epsilon(0, r_s(\mathbf{r})) \tag{5.38}$$

for inner electronic states.

If the modification of the correlation function, shown in equation 5.38, is taken into account, equation 5.31 can be expressed as [146]

$$\rho(\mathbf{P}) = 2\sum\nolimits_{n,k} h(n,\mathbf{k}) \mid B_n(k,\mathbf{P})|^2 \tag{5.39}$$

where $B_n(k,\mathbf{P})$ is given as

$$\sigma(\mathbf{P}-\mathbf{k}-\mathbf{K}) \int_{\Omega} dr e^{-i\mathbf{P}.\mathbf{r}} \psi_{+}^{o}(\mathbf{r}) \psi_{n,\mathbf{k}}(\mathbf{r}) \sqrt{g_{n,\mathbf{k}}(\mathbf{r})} \tag{5.40}$$

and h(n,$\mathbf{k}$) is the Fermi function. $\psi_{n,\mathbf{k}}^{o}$, $\mathbf{k}$ and Ω are the Bloch states, wave vector and unit cell (primitive) [146].

Angular Correlation of Annihilation Radiation (ACAR) technique is utilized when the quanta from the annihilation of positrons with electrons are not emitted in exact opposite directions but instead form a small deviation angle from 180^o. If ϕ_z is the small deviation angle from collinearity, the 1-D ACAR momentum distribution, $\xi(\phi_z)$, can be expressed as [146, 147]

$$\xi(\Theta_z) \approx \int \xi(P_x, P_y, \Theta_z m_e c) dP_y \int dP_x \tag{5.41}$$

where P_x and P_y are the momentum components measured along x and y directions in the laboratory frame of reference. If the independent particle model is used, the ACAR distribution shown in equation 5.41 can be modified and written as [146]

$$\xi(\Theta_z) \approx [k_F^2 - (\Theta_z m_e c)^2] \tag{5.42}$$

which renders inverted parabolas. This is the case for a constant density of states in which valence states are occupied by electrons up to the Fermi level [146].

Chapter 6

Properties and structural probes of superionic conductors

6.1 Properties of superionic conductors

Identification of ionic conductors is through ionic diffusion process in which ions move through the spaces between non-mobile atoms [39]. Non-mobile atoms (ordered sublattice) in the crystal are associated with occupied sites. The sublattice of mobile ions is normally referred to as molten sublattice and the assumption of a molten state is based on the following considerations:

- Some ionic conductors (e.g. $\alpha - AgI$ with best ionic conductivity of $1\Omega^{-1}cm^{-1}$), it has been shown that the conductivity is larger in its solid state than in its liquid state [168].
- The site occupation probability of mobile ions is less than unity [168] (e.g.α-silver iodide or β-alumina.)

Thermal activation energy allows these mobile ions to diffuse through the lattice. It is well understood that the ions reside often in their respective potential wells and the residing time is longer than the time it takes to jump (hopping) to the next site [168, 46]. The harmonic potential well shown in figure 6.1 illustrates the

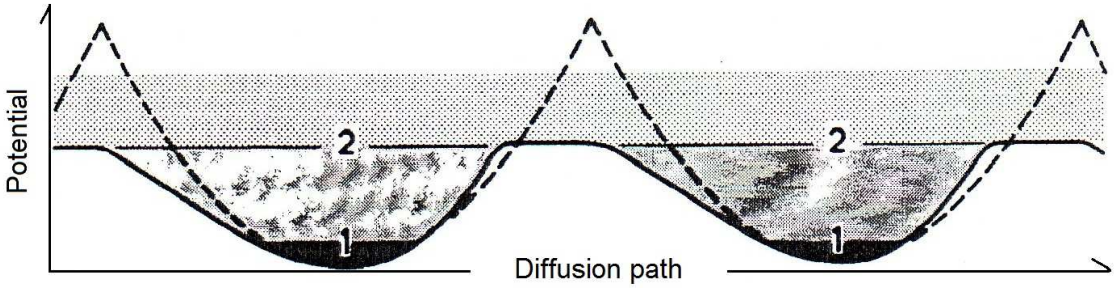

Figure 6.1: Solid line represents the potential along the diffusion path. The potential minima indicate the equlibrium atomic positions. The grey shadowing illustrates the decreasing occupation of energy levels with increasing energy [39]. The broken line indicates the approximation of the solid-line potential by a harmonic potential [168].

population of ions in different excitation states. The occupation probabilities are calculated using Maxwell-Boltzmann statistics. The temperature dependence of the atomic positions and energies is shown by grey shadowing in the figure.

The thermal vibration amplitudes at energy levels 1 and 2 [39] are marked by the width of potential shown as horizontal lines in the figure. The probability density results in the probability of a thermal vibration (phonon) from atomic sites [39] and the subsequent hopping of the atom into a neighbouring volume element. The potential form and the temperature dependence determine the probability density.

6.2 Ionic diffusion

Conduction and the diffusion of mobile ions are closely related to the presence of defects in the crystal lattice [205]. There are two types of defects responsible for ionic motion, namely:

- Schottky defects

- Frenkel defects

Schottky defects are a combination of cation and anion vacancies i.e. ionic pairs from their interior lattice sites to the surface of the crystal. Frenkel defects are combinations of vacancies and intersitial ions. Table 6.2 shows the calculated energies of formation of Frenkel and Schottky defects [79] in some alkali earth flourites. It is clear that in MF_2 crystals, the formation energy for cation Frenkel is always larger than that of anion Frenkel. Schottky pairs have almost the formation energy as that of cation Frenkel and it should noted that as the temperature increases the disordering of F sublattice increases. This will tie up with the discussions involving positron annihilation spectroscopy in chapter 8.

At high temperature values the defects exist in thermodynamic equilibrium in the crystal and for Schottky defects in MX crystals the concentration or mole fraction increases with temperature according to

$$x = x_o exp(-\frac{h_f}{2kT}) \tag{6.1}$$

where

$$x_o = exp(\frac{s_f}{2k}) \tag{6.2}$$

where h_f and s_f are the enthalpy and entropy of formation of pair of defects [80]. The microscopic diffusion coefficient for a defect is given by

$$d = d_o exp(-\frac{\Delta h}{kT}) \tag{6.3}$$

where

$$d_o = \frac{1}{6}\nu a^3 exp(\frac{\Delta s}{k}) \tag{6.4}$$

Table 6.1: Formation energies of Frenkel and Schottky defects in alkaline earth flourites [31].

Substance	defects	Energy (eV)	Charge
CaF_2	Anion Frenkel	2.6 - 2.7	F^-
	Schottky	7.0 - 8.6	$F^- - Ca^{2+}$
	Cation Frenkel	8.5 - 9.2	Ca^{2+}
BaF_2	Anion Frenkel	1.6 - 1.9	F^{-1}
	Schottky	6.3 - 6.9	$F^{-1} - Ba^{2+}$
	Cation Frenkel	7.8 - 8.0	Ba^{2+}
SrF_2	Anion Frenkel	2.2 - 2.4	F^-
	Schottky	6.9 - 8.1	$F^- - Sr^{2+}$
	Cation Frenkel	8.2 - 8.6	Sr^{2+}

where ν is the number of attempts per second, a is the jump distance and Δh and Δs are the activation enthalpy and entropy of the jump, respectively [80]. The factor $\frac{1}{6}$ is appropriate for a cubic lattice. In an electric field there is also a drift mobility given by

$$\mu = \mu_o exp(-\frac{\Delta h}{kT}) \tag{6.5}$$

where

$$\mu_o = (\frac{q}{kT})d_o \tag{6.6}$$

Cations in flourite structures have self-diffusion coefficients that are several orders of magnitude smaller compared to those of anion [82] and therefore the contribution of cations in the ionic conductivity may be neglected. In general, the diffusion processes that have been studied are [19] :

- The vacancy mechanism [19]. The vacancy mechanism involves the jump of atoms into vacancies, see figure 6.2 (a).
- The interstitial mechanism [19]. In this situation the atoms jump from interstice to interstice, see figure 6.2 (b).
- The non-collinear interstitialcy mechanism [19]. In this mechanism, see figure 6.2 (c), the mobile ion knocks the anion initially at the normal lattice site to one of three possible equivalent interstitial sites numbered 3, 4 and 5.

6.3 Ionic conductivity dependence with temperature

The ionic conductivity can be written as [131]

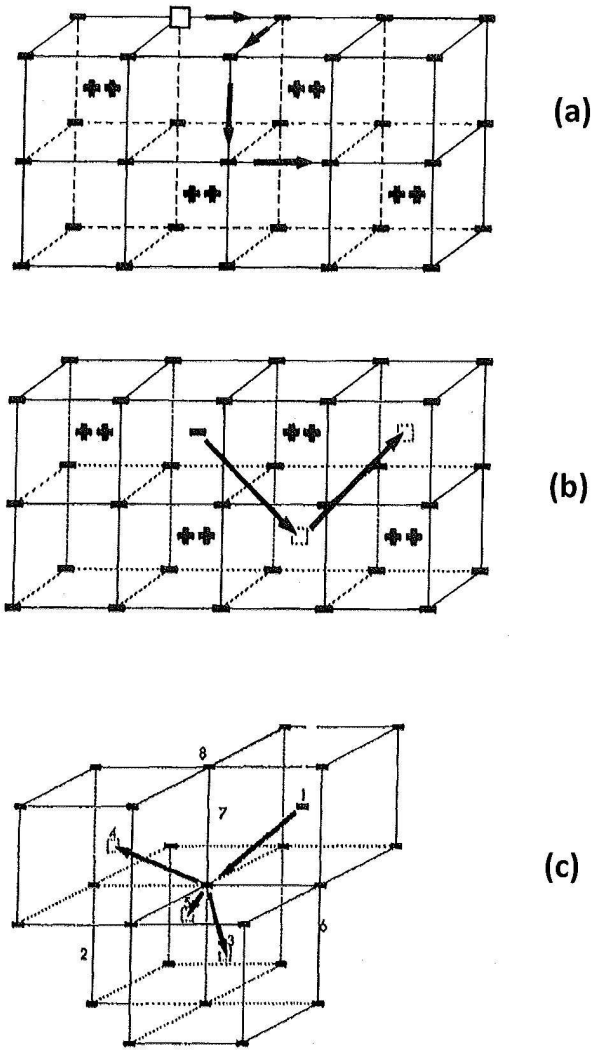

Figure 6.2: Different diffusion mechanisms [19] (a) vacancy mechanism (b) interstitial mechanism (c) non-collinear interstitialcy mechanism.

$$\sigma = \frac{ne^2}{kT}\alpha\nu a^2 exp[-\frac{\Delta G_m}{kT}] \tag{6.7}$$

where n is the mobile ion density (defects), e is their charge, k is the Boltzmann's constant, α is a geometrical factor of order unity, ν is the number of attempts per second by ion to overcome the Gibb's free-energy barrier ΔG_m and a is the jump distance.

At elevated temperatures n is expressed by [71]

$$n = (NN^{'})^{1/2} exp(-\frac{\Delta G_f}{2kT}) \tag{6.8}$$

where N, $N^{'}$ and ΔG_f are the anion lattice site density, the anion interstitial site density and Gibb's free-energy necessary for a Frenkel defect formation respectively [131]. Substituting equation (6.8) into equation (6.7), and use the relationship

$$\Delta G = \Delta H - T\Delta S \tag{6.9}$$

we obtain

$$\sigma = \frac{\sigma_o}{T} exp[-\frac{\Delta H_f/2 + \Delta H_m}{kT}] \tag{6.10}$$

where

$$\sigma_o = \frac{(NN^{'})^{1/2} e^2 \alpha\nu a^2}{k} exp[\frac{\Delta S_f}{2k} + \frac{\Delta S_m}{k}] \tag{6.11}$$

6.4 Structural probes

An extensive amount of work has been done on flourite structure crystals. The main focus of interest in these materials is high conductivities at elevated temperatures. Various experiments to obtain the properties of defects have been

performed including diffusion [19, 115], ionic conductivity [19, 23, 89, 43], nuclear magnetic resonance [88], activation volumes [163, 131], elastic constants [35], specific heat [130, 166, 131] and a number of other techniques [78, 32].

A detailed form of a model for the crystal free-energy for superionic conductors is detailed in [130, 84, 158, 199]. The form of this free-energy density is given by [131, 130]

$$G = G^p + x\Delta G^f - kTlnW - x^2\Delta G^i \tag{6.12}$$

The first term on the right is the Gibb's free-energy of a defect-free crystal and

$$G^p = E^p + PV^p - TS^p \tag{6.13}$$

where x is the Frenkel defects concentration. ΔG^f is the energy shift [130] when the Frenkel defects on the anion sublattice are formed at low defect concentrations, $-kTlnW$ represents the entropy, mainly because of the presence of defects. The fourth term on the right in equation (6.12) is the defect interaction effect [131]. The configurational entropy which in this case is also identical $kTlnW$ is given by [131, 148]

$$lnW = -(q-x)ln(q-x) - (m-x)ln(m-x) - 2xlnx + mlnm + qlnq \tag{6.14}$$

where m is the number of interstitial sites divided by the number of anions. Modification of equation (6.14) is to allow m and q to vary with defect concentration (in most cases q is set to 1) [131]. The minimization of equations (6.12) and (6.13) with respect to x leads to [131, 130]

$$\frac{x^2}{(q-x)(m-x)}\left(\frac{m}{m-x}\right)^{-\partial m/\partial x}\left(\frac{q}{q-x}\right)^{-\partial q/\partial x} = B(x,T) \tag{6.15}$$

where

$$B(x,T) = e^{-\frac{\Delta G^f - 2x\Delta G^i}{kT}} \tag{6.16}$$

6.5 Specific heat capacity of superioinc conductors

The specific heat of the material is given by [131, 130]

$$(\frac{\partial H}{\partial T})_p = T(\frac{\partial S}{\partial T})_p \tag{6.17}$$

where H is the crystal enthalpy and S the entropy. Using equation (6.12) we obtain

$$S = S^p + x\Delta S^f - x^2\Delta S^i + klnW \tag{6.18}$$

The specific heat is then given by [131, 130]

$$C_p = T\frac{\partial S^p}{\partial T} + Tx\frac{\partial \Delta S^f}{\partial T} - Tx^2\frac{\partial \Delta S^i}{\partial T} + F(m,q,T,x) + K(x,T,q,m) \tag{6.19}$$

where $F(m,q,T,x)$ is

$$F(m,q,T) = kT\frac{\partial m}{\partial T}(ln\frac{m}{m-x}) + kT\frac{\partial q}{\partial T}(ln\frac{q}{q-x}) \tag{6.20}$$

and $K(m,q,T,x)$ is

$$K(m,q,T,x) = kT\frac{\partial x}{\partial T}(\frac{\Delta S^f - 2x\Delta S^i}{k} + ln\frac{(q-x)(m-x)}{x^2}) \tag{6.21}$$

The excess specific heat can immediately be obtained by dropping the temperature derivatives of various entropies and using [131, 130]

$$\frac{\partial m}{\partial T} = \frac{\partial m}{\partial x}\frac{\partial x}{\partial T} \tag{6.22}$$

and

$$\frac{\partial q}{\partial T} = \frac{\partial q}{\partial x}\frac{\partial x}{\partial T} \tag{6.23}$$

along with equation (6.19) to obtain

$$\Delta C_p = \frac{\partial x}{\partial T}(\Delta H^f - 2x\Delta H^i) \tag{6.24}$$

Equation (6.12) is differentiated to obtain the $\frac{\partial x}{\partial T}$ factor through the assumption that $\Delta H's$ and $\Delta S's$ are temperature-independent [131, 130]

$$\frac{\partial x}{\partial T} = \frac{\Delta H^f - 2x\Delta H^i}{-2\Delta G^i T + kT^2\epsilon} \tag{6.25}$$

where

$$\epsilon = \frac{2}{x} - \frac{\frac{\partial q}{\partial x}-1}{q-x} - \frac{\frac{\partial m}{\partial x}-1}{m-x} - \frac{\partial^2 m}{\partial x^2}ln(\frac{m}{m-x}) + U + V \tag{6.26}$$

where U is

$$U = -\frac{\partial m}{\partial x}\frac{\partial}{\partial x}(ln\frac{m}{m-x}) - \frac{\partial^2 q}{\partial x^2}ln(\frac{q}{q-x}) \tag{6.27}$$

and V

$$V = -\frac{\partial q}{\partial x}\frac{\partial}{\partial x}(ln\frac{q}{q-x}) \tag{6.28}$$

For $\Delta G^i = 0$ and $x << 1$, equations (6.24) to (6.28) are simplified to the following form [2]

$$\Delta C_p = \frac{x(\Delta H^f)^2}{2kT} \tag{6.29}$$

A simplest possible form of $m(x)$ and $q(x)$ are

$$m(x) = \frac{1}{2} - \alpha x \tag{6.30}$$

and

$$q(x) = 1 - \gamma x \tag{6.31}$$

α and γ parameters represent the effectiveness of the repulsive force in diminishing the number of interstitial sites and lattice sites that are likely to be occupied by interstitials and vacancies.

The calculated values of ΔC_p against the temperature are shown in figure 6.3 for PbF_2 [130]. The corresponding concentrations of Frenkel defects plotted against the inverse temperature [131, 130] are shown in figure 6.4.

Dworkin and Bredig [60] discovered that the diffuse transition in flourites is accompanied by a peak in the excess specific heat (specific heat anomally) as shown in figure 6.5.

6.6 Bulk modulus dependence on temperature

Bulk modulus for crystalline solid is defined as [131, 130]

$$\frac{1}{K_T} \tag{6.32}$$

where K_T is the isothermal compressibility given by

$$K_T = -(\frac{1}{V})(\frac{\partial V}{\partial P})_T \tag{6.33}$$

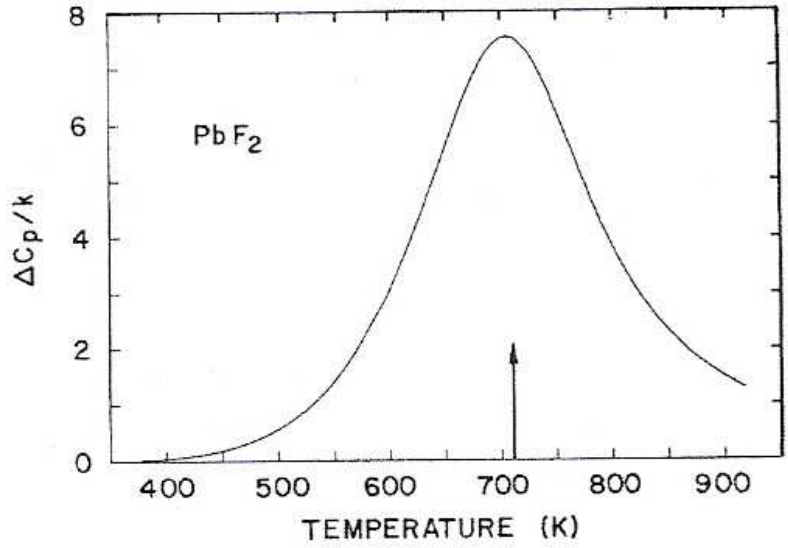

Figure 6.3: Theoretically calculated excess specific heat of PbF_2 [130, 131] to approximate the experimental results obtained by Schroter et al [166].

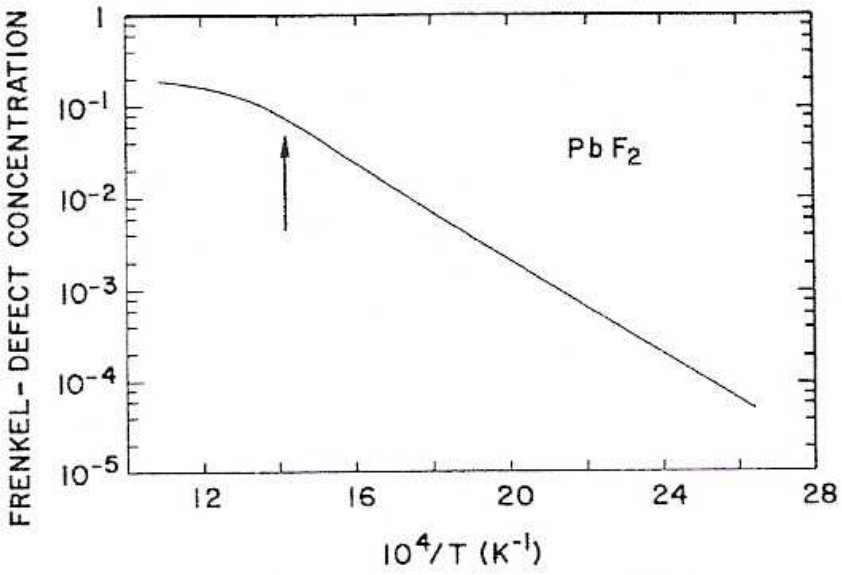

Figure 6.4: Frenkel-defect concentration in PbF_2 against temperature [130]. The arrow points to the concentration at which the anomaly in the specific heat of PbF_2 occurs [130].

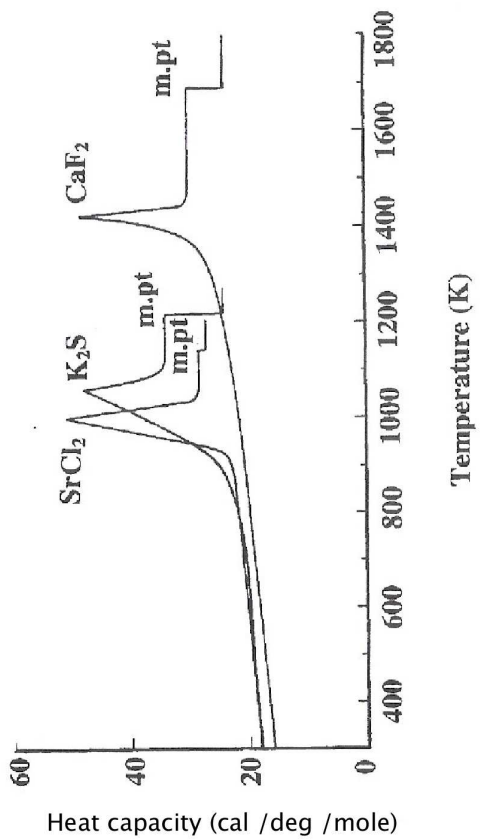

Figure 6.5: Specific heat anomaly for several materials [60].

The volume is obtained from [131, 130]

$$V = (\frac{\partial G}{\partial P})_T \tag{6.34}$$

and this leads to

$$V = V^p + x\Delta V^f - x^2\Delta V^i \tag{6.35}$$

Using equation 6.12, after the assumption of non-variability ΔV with pressure, we obtain

$$K_T = -\frac{1}{V}\frac{\partial V^p}{\partial P} - \frac{1}{V}\frac{\partial x}{\partial P}(\Delta V^f - 2x\Delta V^i) \tag{6.36}$$

Differentiation of equation 6.25 with respect to pressure gives

$$\frac{\partial x}{\partial P} = -T\frac{\partial x}{\partial T}\frac{\Delta V^f - 2x\Delta V^i}{\Delta H^f - 2x\Delta H^i} \tag{6.37}$$

For $x << 1$ and $\Delta G^i = 0$ (in the limit), we obtain

$$K_T = K_T^o + \frac{x(\Delta V^f)^2}{2kTV^p} \tag{6.38}$$

where

$$K_T^o = -(\frac{1}{V^p})(\frac{\partial V^p}{\partial P})_T \tag{6.39}$$

The bulk modulus as a function of temperature [131, 130], in BaF_2, has the lowest value at approximately 1200 K as shown in figure 6.6.

6.7 Thermal expansion coefficient

The thermal expansion coefficient is given by [130]

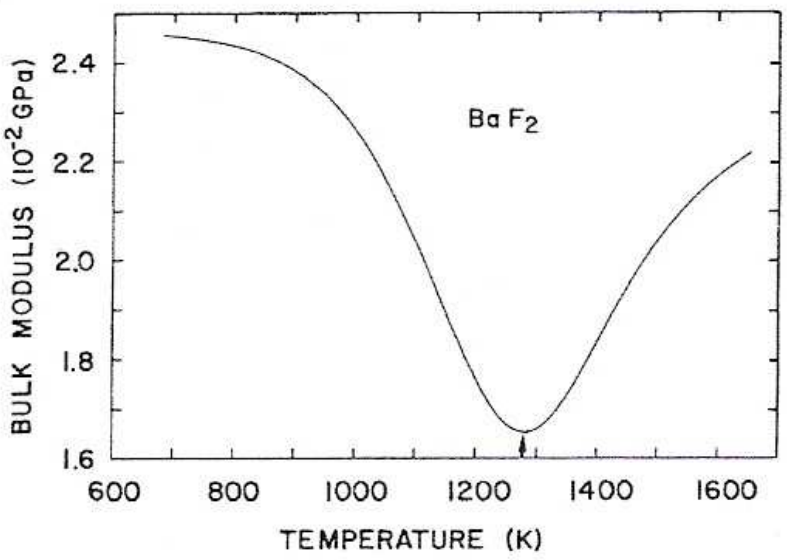

Figure 6.6: Bulk modulus against temperature for BaF_2[130].

$$A = \frac{1}{V}(\frac{\partial V}{\partial T})_p \tag{6.40}$$

and by differentiating equation 6.35 and substituting $(\frac{\partial V}{\partial T})_p$ into equation 6.40 we obtain

$$A = \frac{1}{V}\frac{\partial V^p}{\partial T} + \frac{1}{V}\frac{\partial x}{\partial T}(\Delta V^f - 2x\Delta V^i) \tag{6.41}$$

Substituting equation 6.25 into equation 6.41 gives

$$A = \frac{1}{V}\frac{\partial V^p}{\partial T} + \frac{1}{V}(\frac{\Delta H^f - 2x\Delta H^i}{-2\Delta G^i T + kT^2\epsilon})(\Delta V^f - 2x\Delta V^i) \tag{6.42}$$

In the limit $\Delta G^i = 0$ and $x << 1$, we obtain

$$A = \frac{1}{V^p}(^{p}_{-} + \frac{1}{V}(\frac{\Delta H^f \Delta V^f}{kT^2\epsilon}) \tag{6.43}$$

Figure 6.7 shows the thermal expansion coefficient as a function of temperature [130]. Coefficient of expansion is critical since we shall be calculating and experimentally determining the lattice constants at different temperatures.

Thermal expansion coefficient is related to the calculation of lattice constant as a function of temperature. In ionic matrials it is shown that positron annihilation technique can best be utilized to identify the threshold temperature at which disordering of a sublattice becomes evident. Positron annihilation technique (PAT) is also used as a tool in the determination of minimum lattice constant, through S-parameter, at which superionic conductivity is first observed. A detailed explanation is given in subsequent chapters.

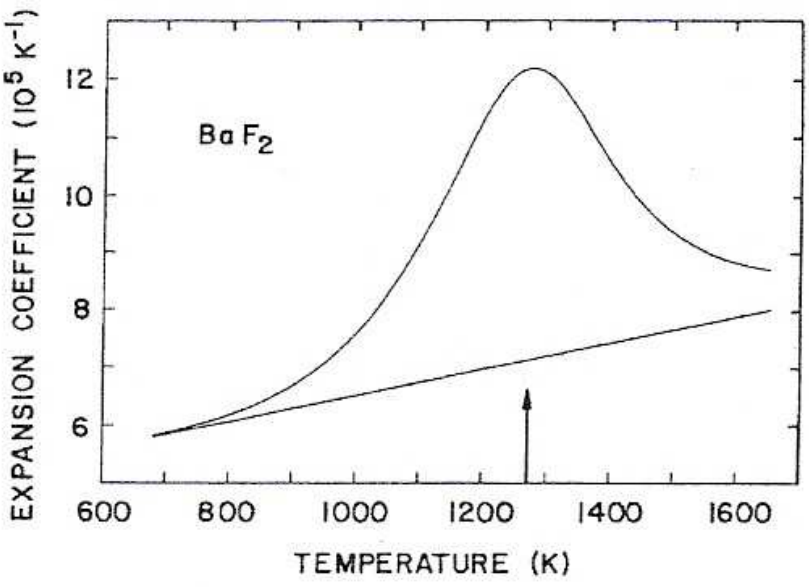

Figure 6.7: Thermal expansion coefficient against temperature for BaF_2 [130]

6.8 The behaviour of superionics based on defect concentration and structures

The increase in temperature leads to high defect concentration and this causes strong interaction between these defects and thus the formation of clusters of 2/2/2 as shown in figure 6.8 [153]. Therefore the superionic state in fluorites can be explained using these clusters [47, 37, 8].

An increase in the number of clusters formed leads to an increase in the defect-defect repulsions which reduces the availability of site. These factors tend to limit a further generation of thermal disorder above the transitional temperature.

Quasi-elastic neutron scattering experiments to study superionic behaviour in PbF_2, $SrCl_2$ and CaF_2 were done by Hutchings [86] to explain quasi-elastic peaks. Catlow et al. [34] utilized Extended X-rays Absorption Fine Structure (EXAFS) studies to demonstrate that the type of cluster formed depends on the size of the dopant ion [42]. These researchers performed these studies on CaF_2 doped with 10 mol percentage ReF_3, where Re represent rare-earth. They found that (2,2,2) dimeric clusters were dominant for CaF_2 doped with larger rare-earths $(La, Ceetc.)$ whilst for CaF_2 doped with smaller rare-earths (Tb, Tm, etc) the cubo-octahedral clusters were formed.

Doping flourites with trivalent impurities results in transition temperatures being reduced [36, 135, 134, 122, 48] meaning that the transition temperature occurs at much lower temperatures than in pure compounds [153].

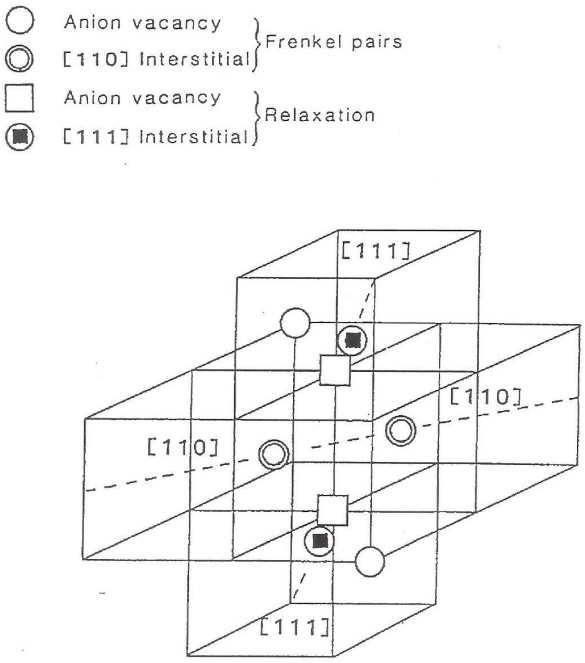

Figure 6.8: A 2/2/2 cluster in pure CaF_2 [33].

Chapter 7

Positron Annihilation Experimental Arrangement

Positron annihilation spectroscopy requires a different measurement technique for both the Doppler broadening and positron lifetime measurements at different temperatures. Since the temperature range starts at room temperature to 900 K, a relatively good vacuum of about 10^{-6} Torr has to be mantained.

7.1 Vacuum Chamber

Figure 7.1, shows a schematic diagram of a vacuum chamber system for medium to high temperature experiments. It consists of a rotary pump which is used to reduce pressure to about 10^{-3} Torr with the valve closed. The turbo pump is then used to achieve pressures down to about 10^{-5} Torr. It consists of multiblades and it attains a rotational speed of 27 000 rpm. It has become the standard that in order to further improve vacuum, a heater tape shown in figure 7.1 is utilized to heat up the lower part of the chamber for the degassing process and this vastly improves the vacuum to about 5.3×10^{-6} Torr.

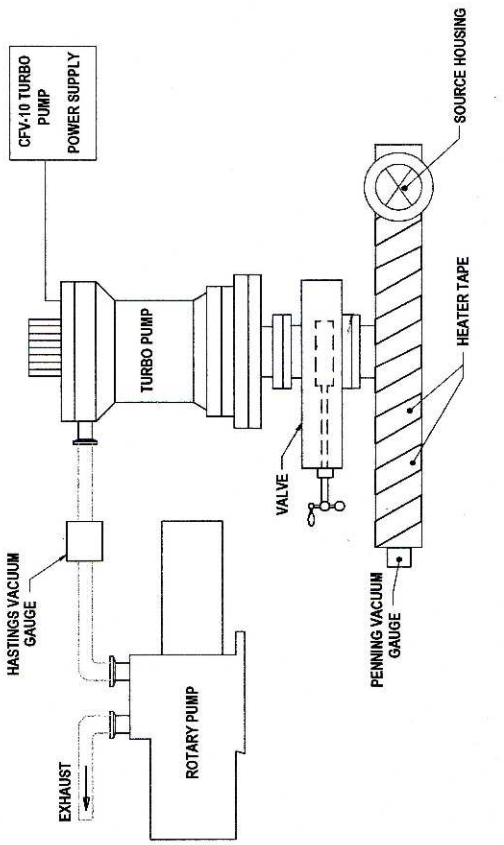

Figure 7.1: Schematic diagram of the pumping section of the experiment. The CFV-10 turbo pump has a peak speed of 27 000 rpm at full operation.

7.2 Source-Sample-Heater Mounting System

A standard source-sample sandwich arrangement prepared from two equal single BaF_2 cyrstals each of size 10 mm x 8 mm x 2 mm, of orientation (111) and its mounting system, is shown in figure 7.2. A source of activity 20 μCi was prepared from a sodium solution and evaporated on a thin nickel foil of thickness 7 μm. A second nickel foil was used together with the first nickel foil to seal the source. The use of nickel foils enables high temperature measurements. Two shapal-M ceramics shown in figure 7.2 were used to isolate the sandwich arrangement and collector plates from making contact with the mounting frame. The choice of ceramics used is based on their physical properties. The electrical resistivity of the shapal-M ceramics is 1.8×10^{13} Ω cm at 25 ^oC with thermal conductivity of 100 $\mathrm{W}m^{-1}K^{-1}$ at 20 ^oC. Two metal plates shown in figure 7.2 provide an adjustable electric field across the source-sample arrangement and also provide path for ionic current.

The heater housing is situated at the lower part of the mounting system as shown in figure 7.2. The heater element itself which is made from molybdenum as shown in figure 7.3. Molybdenum heater element was used because of its low coefficient of thermal expansion (5.1×10^{-6} mm per degree celcius) and high melting point of 2615 degrees Celcius. The other advantage of utilizing molybdenum heater is its good thermal conductivity of 138 W per meter per Kelvin from 0 to 100 degrees Celcius.

The heater element is isolated from the rest of the mounting system by a sapphire glasses. The choice of sapphire glasses is based on the following properties:

(1) high resistivity of 10^{14} at ambient temperature

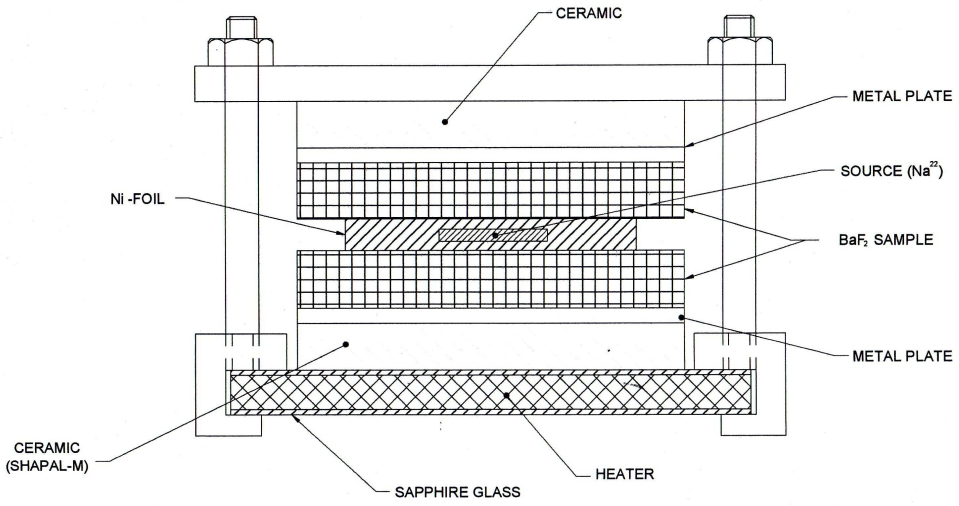

Figure 7.2: Source-sample-heater arrangement.The two ceramics (Shapal-M) are used to isolate electrical contacts (collector metal plates) from the mounting frame and are also used as heat transport passage to the samples.

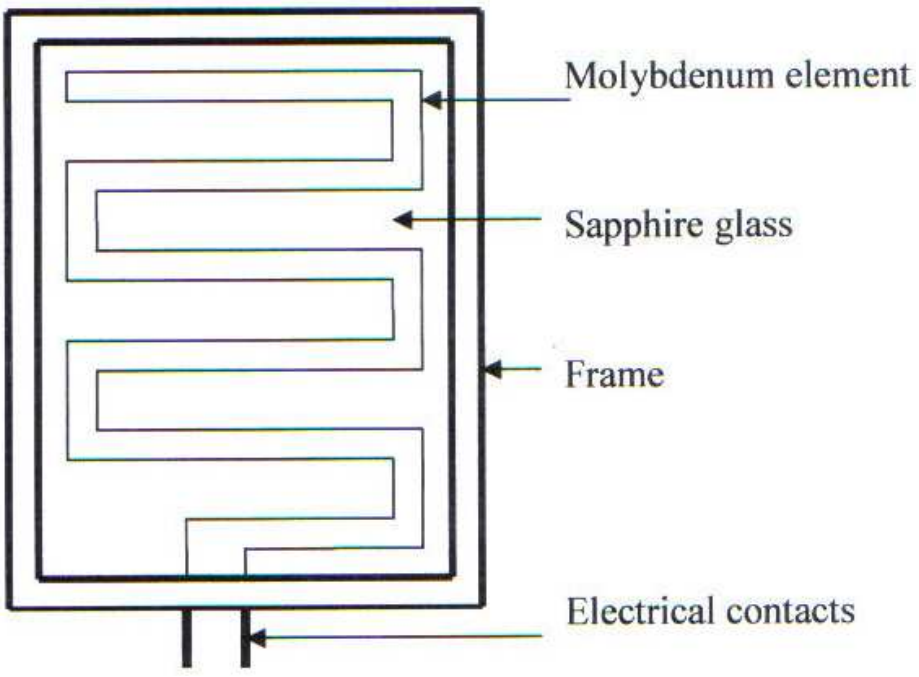

Figure 7.3: Schematic diagram of the heater system used. Sapphire glass is mainly used because of its high electrical resistivity of 10^{14} Ω cm at ambient temperature, good thermal conductivity of 42 W $m^{-1}K^{-1}$ at 25 degrees Celcius, and high melting point of 2053 ^oC.

(2) good thermal conductivity of around 42 W per meter per Kelvin at 25 degrees Celcius

(3) high melting point of 2053^o C

A K-type (chromel-alumel) was also utilized to obtain the temperature of the source-sample sandwich arrangement. A relationship between thermal conductivity and temperature in chromel-alumel is shown in figure 7.4. The chromel-alumel thermocouple was chosen because of its $+/-1.5$ degree Celcius tolerance between -40 and 375 degrees Celcius and a tolerance of $+/-0.004$ T between 375 and 1000 degrees Celcius, where T represents the temperature of hot junction.

7.3 Doppler Broadening and Positron Lifetime Experimental Arrangements

7.3.1 Doppler Broadening Spectroscopy

The commonly used β^+ isotope is ^{22}Na which decays according to the decay scheme $^{22}Na \rightarrow ^{22}Ne + e^+ + \nu$. Doppler broadening requires a special arrangement of energy detectors. In solids, positrons predominately annihilate with outer electrons from the conduction and valence bands.

In general, the emission-annihilation event depict an exponential like functional form. The component of the function comprises of the background noise, the time resolution and lastly the annihilation. One hardly expects noise in a true coincidence measurement however the non deterministic emission of the positron by radioactive ^{22}Na may produce positrons rapidly one after another and this may lead to a false coincidence. Therefore the source activity determines the background level in both the Doppler broadening and lifetime experiments.

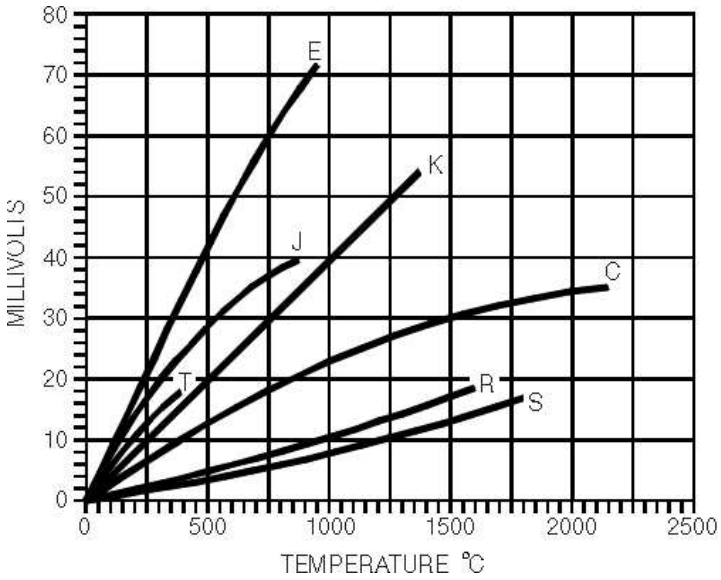

Figure 7.4: A plot of thermal conductivity versus temperature in chromel-alumel thermocouple (K-type) and other types of thermocouples [116].

The analysis of the probability events occurring from annihilations with core electrons is not feasible in a traditional, single-detector setup due to high noise background. This challenge is hugely eliminated in a two-detector system detecting both annihilating photons and selecting only simultaneuos events. The two-detector system was then employed which improved the energy resolution by $\sqrt{2}$. The measured energy resolution was 1.6 keV (FWHM) at 511 keV. The background radiation mainly due to the 1.27 MeV gamma during a β^+ decay of ^{22}Na to ^{22}Ne, is reduced substantially. In this experiment the peak-to-noise ratio was 1.5×10^4 which is good for the analysis of high momentum components.

The Doppler broadening technique is a process in which the quantity of defects is measured to determine the momentum density distribution. The annihilation radiation (photons) have energies given by [129]

$$E_1 = E_0 - \frac{E_b}{2} + \Delta E + \delta_1 \tag{7.1}$$

and

$$E_2 = E_0 - \frac{E_b}{2} - \Delta E + \delta_2 \tag{7.2}$$

where E_b, E_0, and δ_i are the binding energy of the $e^+ - e^-$ system, the electronic rest mass energy and detector resolution errors, respectively [129]. Longitudinal projection of momentum distribition (P_L), in the direction of 511 keV emission, is provided by the Doppler shift (ΔE) on the annihilation quanta by [129]

$$\Delta E = \frac{cP_L}{2} \tag{7.3}$$

where c is the speed of light.

From annihilation equations (7.1) and (7.2) the sum and difference of the two γ energies can be written as [129]

$$E_1 + E_2 = 2E_0 - E_b + (\delta_1 + \delta_2) \tag{7.4}$$

$$E_1 - E_2 = 2\Delta E + (\delta_1 - \delta_2) \tag{7.5}$$

The energy spectrum of a two detector system is plotted in a two-dimensional histogram shown in figure 7.5. This is the coincidence spectrum which represents the measurements of photon energies E_o and E_1 in the detectors. The coincidence peak broadens along the region $E_o + E_1 \approx 2m_oc^2$ due to the Doppler shift of the annihilating radiation.

The positive gradient diagonals in figure 7.5 represent lines of constant energy difference. Two-detector system improves the energy resolution of the spectrometer by a factor of $\sqrt{2}$ [129]. This can be observed from figure 7.5 where the tails of negative slope diagonals are almost free from Compton scattered photons. The reduced Compton background allows the investigation of electron-positron annihilation momentum density resulting from annihilations of core electrons with positrons. The circuit diagram used for Doppler broadening is shown in figure 7.6

High-purity germanium (HPGe) detectors were utilized to measure the energy of the gammas resulting from the annihilation of positron-electron pairs. Detectors were placed 15 cm apart in a collinear arrangement. The effective energy resolution of the detectors was 2 keV (FWHM) at 511 keV. The event-rate in two-dimensional spectra was measured at approximately 300 $counts/s$. The spectra

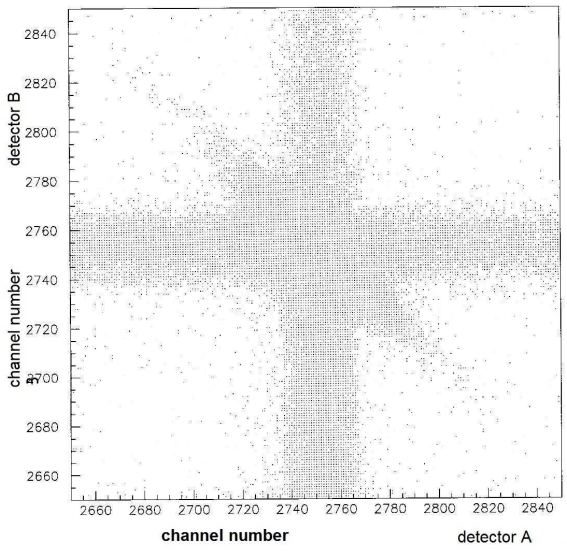

Figure 7.5: A two dimensional spectrum of coincidence events collected with barium flouride. The spectrum contains a total of more than 6×10^6 events. The elliptic region extending diagonally with $E_0 + E_1 \approx 2m_oc^2 = 1022$ keV, comes from annihilations with high momentum electrons and this region is nearly background free.

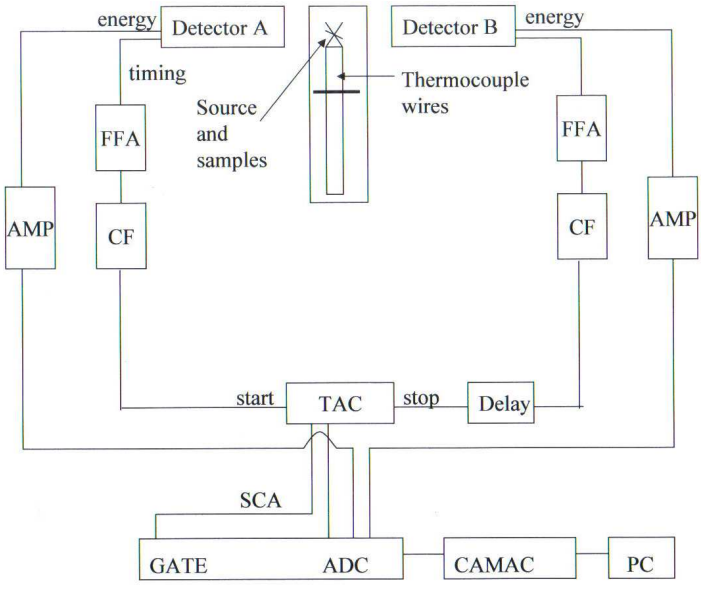

Figure 7.6: Circuit diagram for high resolution source-based electron-positron momentum distribution measurements. For momentum distributions, high purity germanium detectors A and B were used. Effective energy resolution obtained was 2 keV at the 511 keV annihilation peak.

over a temperature range from room temperature (300 K) to 700 K were accumulated for 6 hours each.

The centroid positions of the 1275 keV gamma line were monitored over the entire measurements to ensure the stability of the spectrometer as shown in figure 7.7. This is very useful since a stable 1275 keV gamma line means a non-drifting condition of the 511 keV peak. The broadening of the 1275 keV line has to be monitor in the process of data accumulation.

The Doppler broadening for the 1275 keV line should stay constant throughout the temperature range since 1275 keV gamma is not part of the electron-positron annihilation gammas. The S-parameter over the temperature range for the 1275 keV line was calculated and is shown in figure 7.8. It is clear from the graph that there is no change in the s-parameter between 300 K and 800 K.

7.3.2 Lifetime measurement technique

This technique monitors the time spent by the positron in the sample to derive defect related information. A start signal is the 1275 keV gamma accompanied by the positron emission from Na-22 isotope during its decay to Ne-22. The positron then enters the sample where it annihilates with electron either in the bulk (defect-free region) or in the defect producing two γ photons of 511 keV each. The 511 keV annihilation photon plays a role of a stop signal. The positron source-sample arrangement is prepared by sandwiching a sealed positron source of activity 20 μCi between two identical pieces of the sample material. The time difference between the detection of 1275 keV gamma photon and the arrival of 511 keV due to the positron-electron annihilation, is the lifetime of the positron inside the sample. The annihilation follows a first order kinetics. Therefore,

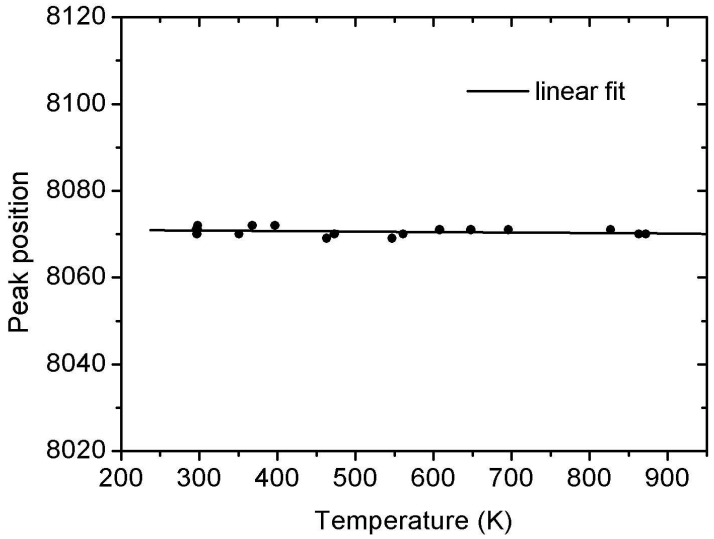

Figure 7.7: The centroid position of the 1275 keV gamma line was monitored over the temperature range to ensure the stability of the electronics. This was also carried out as a tool to minitor the stability of the 511 keV annihilation peak.

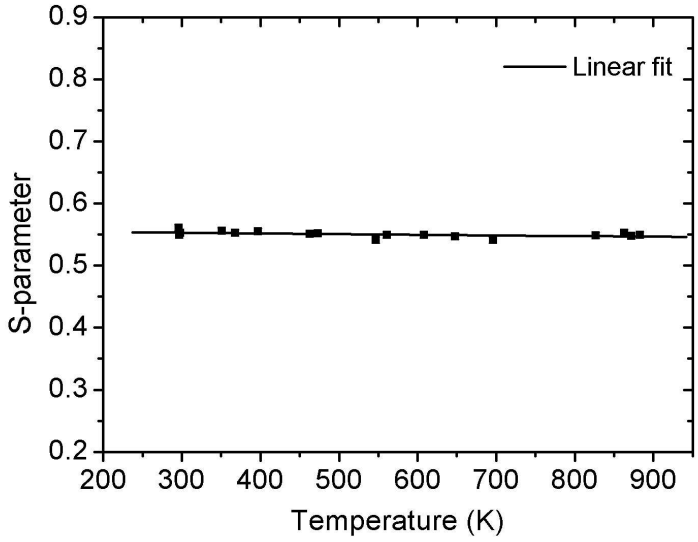

Figure 7.8: The S-parameter of the 1275 keV gamma line was monitored over the temperature range. The area under the 1275 keV curve remained constant throughout the temperature range since the 1275 keV line is not part of the positron-electron annihilation energy.

inside a defect-free sample, positrons annihilate at a fixed rate. If positrons are directed toward a material that contains voids or other open-volume defects, they thermalize around the material and tend to be trapped at the defect. A void means that there is no atom and hence fewer electrons and therefore the positrons live longer than they would in a defect-free material. The experimental arrangement of the positron lifetime measurement is shown in figure 7.9 and the resulting positron lifetime spectrum obtained with a typical spectrometer presented in figure 7.9 give a spectrum for BaF_2.

7.3.2.1 Detectors

In positron lifetime spectrometer, photomultipliers are used and consist of photo-multipier tubes and scintillators. Scintillators produce photons in the visible range when exposed to radiations of high energy. The high energy fall on these crystals and through the process of [178] photoelectric effect, Compton scattering and pair production, they transfer their energy either fully or partially to primary electrons. These primary electrons in turn excite multiple electrons. During de-excitation to the ground state, these electrons emit photons in the visible region.The ideal shape of a detector is conical, but due to the constraints in the manufacturing sector, the detectors are generally constructed as a truncated cones. This minimizes the spread in time due to the distance travelled by the photons before they reach photomultiplier tube (PMT).

In this experiment BaF_2 scintillators coupled with XP2020 Photomultiplier tubes were used. The scintillator converts the high energy gamma photons into low energy of visible light which could be easily detected by PMT. The low energy light photons produced by the scintillator are then collected at the photocathode, which is biased by a high negative voltage. This gives rise to photoelectrons in

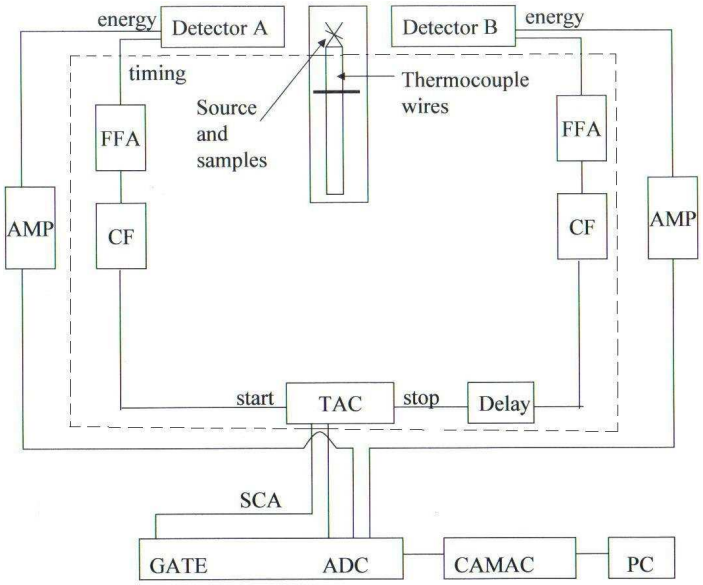

Figure 7.9: Fast timing circuit shown within the broken line. Fast filter amplifiers (FFA) with time rise of less than 8 ns are standard for output maximum amplitude of +5V. Constant fraction differential discriminator selects the correct start (1275 keV) and stop signal (511 keV) and in this way it can act as single channel analyzers. The analogue output signal of the time-to-amplitude convertor, which is the time difference between stop and start signals is converted into a digital pulse by the analogue-to-digital convertor (ADC) which can be read by the camac.

accordance with photoelectric effect. These photoelectrons are then focussed onto electron multipliers which essentially consist of electrodes called dynodes where each dynode is charged to a higher potential than the previous one. Therefore electrons are accelerated and through the process of secondary emission, the electron population is amplified by a factor of 10^5 to 10^7 per photon incident on the cathode. A large amount of charge is then accumulated at the anode which appears as an electric output pulse.

7.3.2.2 Constant Fraction Differential Discriminator (CFDD)

Constant Fraction Differential Discriminator specify a clear-cut mark for the arrival of a signal irrespective of its amplitude and rise time variations. CFDD splits the input signal into two parts. The first part is attenuated by 0.4 and the second part is inverted and delayed. The two signals are summed algebraically to obtain a zero crossing-over which does not depend on the rise time and amplitude. The moment a signal crosses zero, a pulse is generated. CFFD is also equipped with a single channel analyser which selects the signal corresponding to γ-photon of desired energy with the aid of lower level discriminator (LLD) and upper level discriminator (ULD) voltages.

7.3.2.3 Time to Amplitude Convertor (TAC) and CAMAC Crate

The main function of TAC is to convert the time difference between the arrival of signals at its START and STOP inputs, into amplitudes. The start signal is the 1.275 MeV gamma photon which signifies the birth of a positron when ^{22}Na beta-decays into ^{22}Ne. The stop signal is the annihilation photon (511 keV) which signifies the death of a positron. The arrival of the START signal triggers the process of charging a capacitor using a constant current. The charging process continues until the arrival of STOP signal. The charge accumulated in the

capacitor is proportional to the time for which it has been charged. In addition, the voltage is, in turn, proportional to the charge. The TAC, therefore, gives pulses whose voltage amplitude is in proportion with the time difference between START and STOP signals. The data acquisition system (DAQ) comprised of a Computer Automated Measurement and Control (CAMAC) which basically controls analog-to-digital convertor which is linked to a list-sequencer (LS). This unit is critical in data flow between modules and crate controller.

7.3.3 Variable-energy slow positron beam

Variable energy slow positron beam shown in a schematic diagram in figure 7.10 was used for surface and bulk studies in ionic LiF [173] implanted with 100 keV argon ions (Ar^+) at different fluencies. The beam belongs to the Reasearch Centre, Rossendorf in Germany. The equipment comprises of a virgin positron source chamber, moderator, a beam-guiding line, an accelerator and a target chamber. Positrons from ^{22}Na radioisotope (30 mCi) are moderated by a tungsten foil in order to produce a monoenergetic beam. The beam diameter is tuned to a diameter of $\sim$ 3 mm. After moderation the positrons [173] accelerated to obtain intended energies. Finally, positron are focused onto the target which is made of the material to be studied. The energy can be selected in the interval between 10 eV to 50 keV. In this experiment the highest energy used was 25 keV

The thermalization time of positrons inside the target material takes few picoseconds followed by the diffusion leading to the annihilations. Each annihilation produce two gamma rays (511 keV each) that are detected by high purity germanium (HPGe) detectors with resolution of 1.26 keV (FWHM) at 511 keV.

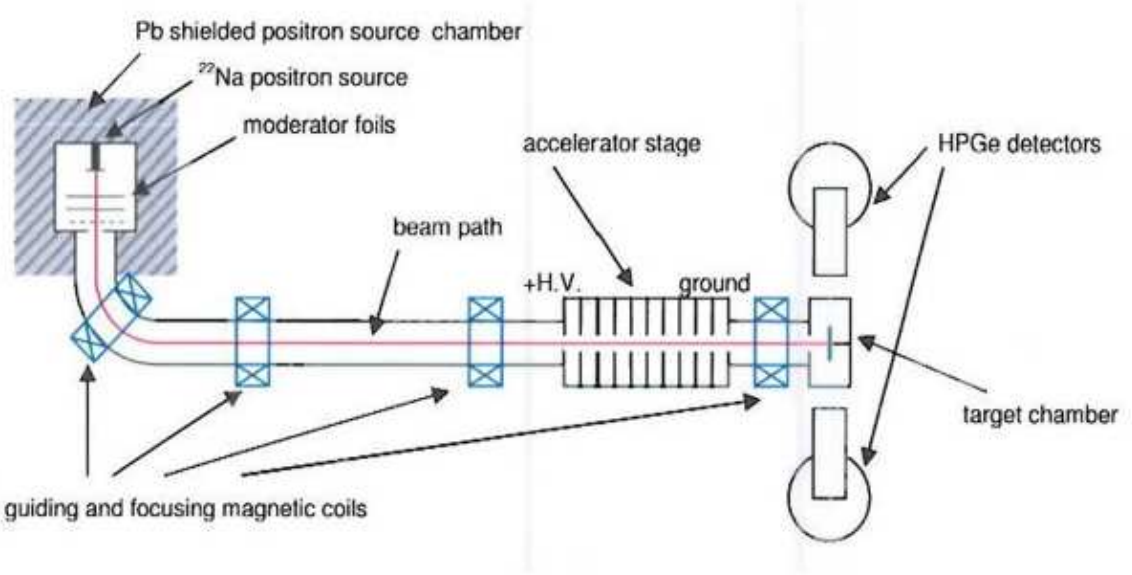

Figure 7.10: Schematic diagram of a variable positron energy beam showing various critical components of the beam line. The energy can be varied between 10 eV and 59 keV [141].

Chapter 8

Experimental results, analysis and discussion

This chapter is based on the identification of types of defects observed in BaF_2, $FeTiO_3$ and LiF. LiF color centers due to ion implantation, using slow positron beam and the effect the implantation has on electrical properties of alkali halide (LiF), is discussed. Theoretical calculation due to annihilations of positrons with valence and core states are discussed. This chapter is organized as follows:

- Variation of lattice constant of BaF_2 with temperature by XRD
- S- and W- parameters calculation in BaF_2
- Positron Lifetime in BaF_2
- Positron lifetime in $FeTiO_3$
- Beam based S-parameter in LiF
- Analysis and discussion

8.1 Lattice constant measurements in BaF_2 using XRD

Lattice constant determination at various temperatures is a condition in the calculation of the S-parameter. Aityan et al. [5] also calculated lattice constant in barium flouride using neutron diffraction method. In this study XRD was performed on powder barium flouride using Bruker D8 Advance diffractometer which is equipped with a Goebel Mirror for pseudo parallel beam optics and a Vantec detector and an Anton Paar XRK-900 reaction chamber. A collected X-ray diffraction pattern of powder barium fluoride in the temperature range 300 - 1173 K at regular intervals of 30 K, is represented in figure 8.1. It is evident that there is no phase transition with temperature. The absence of satellite line/peaks indicate no symmetry/localized disorders upon annealing of BaF_2 in the range 300 - 1173 K.

Experimental XRD data was then compared with the reference patterns to determine the phases present. An excellent match is observed in figure 8.2 corresponding to Flourite structure of lattice constant. Rietveld refinement was further done using TOPAS 4.2 and EVA programs to obtain the lattice constant as a function of temperature as shown in figure 8.3.

Lattice constant is utilized in the calculations of S-parameter and electron-positron momentum density in BaF_2 using generalized gradient approximation. Other authors have calculated the lattice constant using various techniques [41, 5].

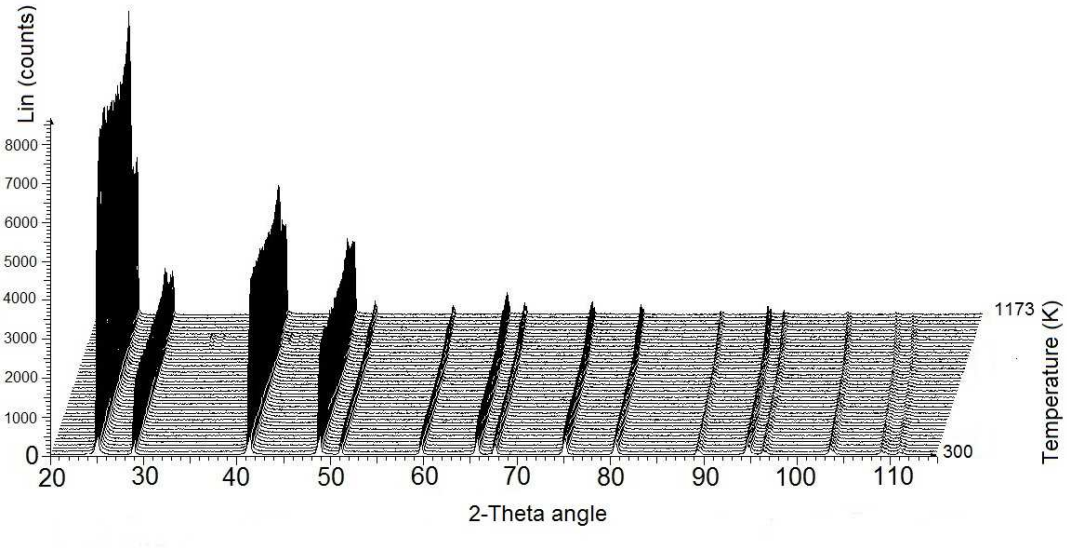

Figure 8.1: Measured X-ray diffraction patterns in BaF_2. The data represents 45 scans from 300 - 1173 K at regular temperature intervals of 30 K.

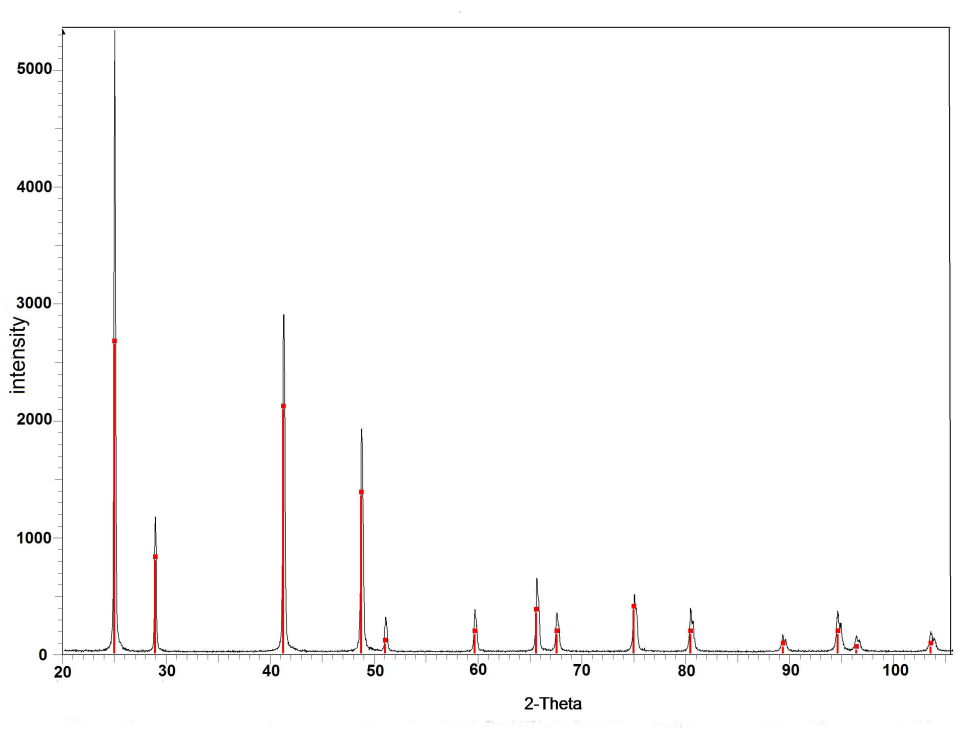

Figure 8.2: X-ray diffraction pattern on BaF_2 fitted with reference pattern to determine the phases present.

8.2 Determination of S- and W-parameters in ionic BaF_2

Doppler broadening spectroscopy is a non-time resolved experiment. The positron annihilation spectra (Doppler broadening spectra) were accumulated over a temperature range starting from 300 K to 800 K. Each spectrum contains an average of about 10^6 events.

The energy resolution achieved at 511 keV was 1.6 keV FWHM. The central S-parameter, which is the ratio of the centroid area to the total area under the annihilation curve, after background subtraction, is plotted in figure 8.4 as a function of temperature. Experimental data is fitted with Boltzmann function and the fitting equation is given by

$$y = A_2 + \frac{A_1 - A_2}{1 + e^{\frac{x - x_o}{dx}}} \tag{8.1}$$

where A_1 is the initial S-parameter value, A_2 is the final S-parameter value, x_o is the center and dx is the width. The s-parameter value at the center is half way between the two limiting values of A_1 and A_2 and the width of this range is approximately dx. W-parameter is obtained from annihilation energy distribution curve. The illustration is shown in figure 8.5. It has to be emphasized that without two-detector system it would be difficult to obtain the wing parameters. The one-detector system has a noise which prohibits the information from core states. W- versus S-parameters is shown in figure 8.6

8.2.1 Analysis and discussion

It is clear from figure 8.4 that, although there is no appreciable increase in S-parameter from 300 K to 580 K ($\Delta S = 0.001$), there is an appreciable increase

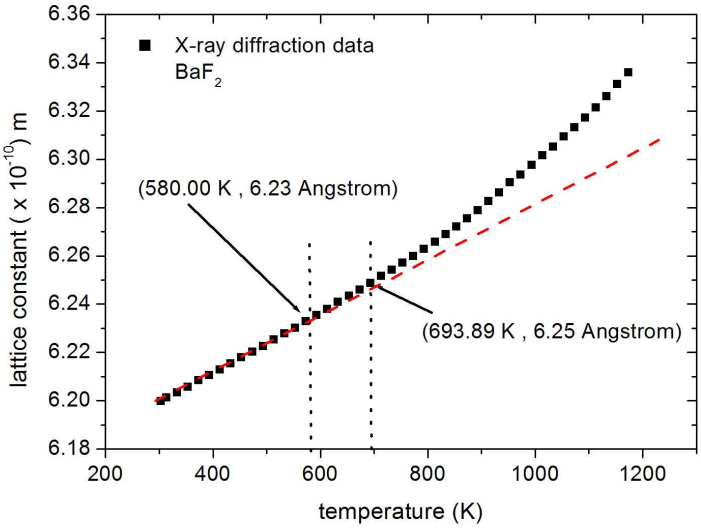

Figure 8.3: The dependence of barium flouride lattice constant on temperature. Lattice constant was extracted from XRD pattern spectra using both EVA and TOPAS programs.

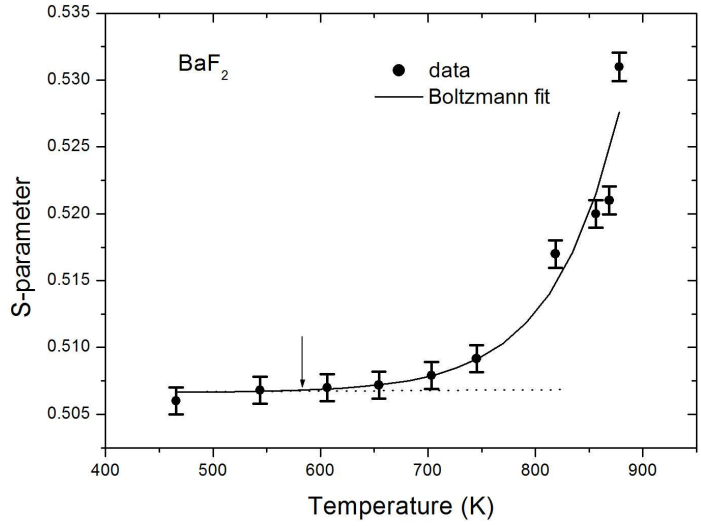

Figure 8.4: S-parameter plotted as a function of temperature. S-parameter begins to deviate from 0.50622 at 580 K as a result of slight thermal expansion of the crystal. The Boltzmann fitting equation is used and the fitting parameters, A_1, A_2, x_o and dx were obtained as 0.50622, 1.13655, 1192.6626 and 92.24452, respectively.

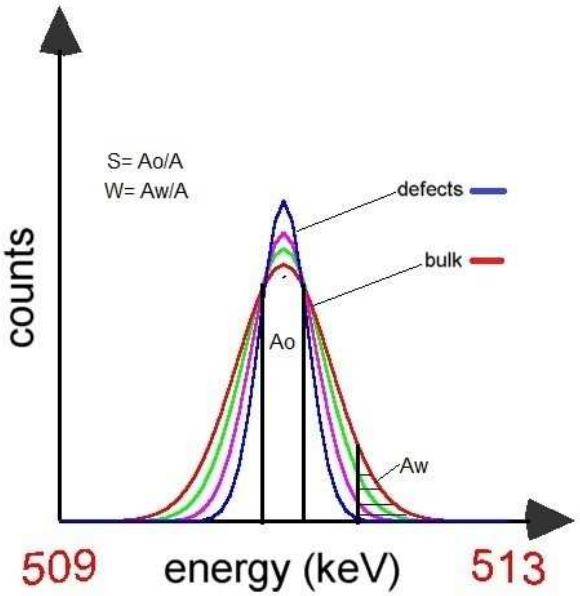

Figure 8.5: The wing parameters (W-parameters) are calculated using the ratio A_w/A_o from each annihilation curve. Different curves have different A_w values as illustrated in the figure

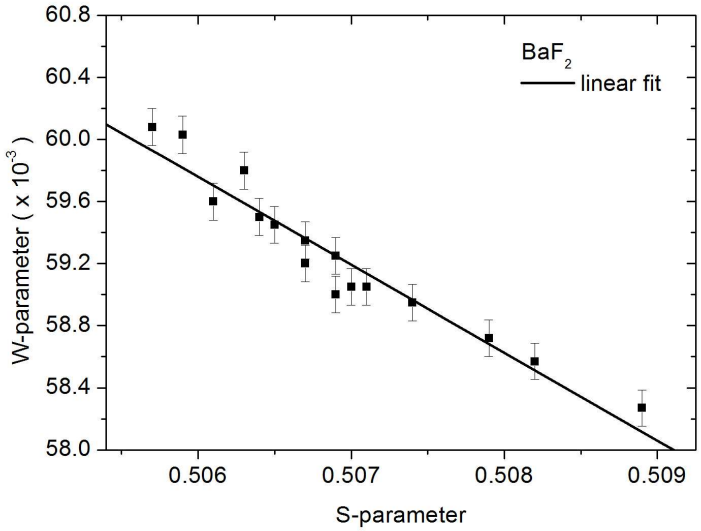

Figure 8.6: The plot of S versus W parameters gives a clear indication of the distribution of annihilation sites in the sample.

of thermal vacancies between 580 K and 877 K ($\Delta S = 0.024$). In BaF_2, the formation energy of anion Frenkel defects as shown in table 6.2 [31], in chapter 6, is between 2.2 and 2.4 eV which is lower compared to the formation energy of cation Frenkel defects which ranges from 7.8 to 8.0 eV. It is also noted that Schottky defect formation requires energy in the range from 6.3 to 6.9 eV which is also high in the temperature range. Therefore throughout the experiment in the temperature range, we assume the migration of fluorine anions (F^-) rather than cations (Ba^{2+}).

These Frenkel defects are a result of an increase of anion interstitials which are characterized by the temperature dependent lattice parameter. These defects when subjected to a constant electric field of about 10^5 V/m and varying the temperature, we obtain the temperature dependent superionic conductivity in BaF_2 as shown in figure 8.7. It is worth emphasizing that a small activity in conductivity occurs at a much later temperature than 580 K. The experiment is fitted with exponential growth curve given by

$$y = A_1 \times e^{\frac{x}{t1}} + y_o \tag{8.2}$$

where A_1, y_o and $t1$ are the amplitude, conductivity off-set and temperature constant respectively.

The S-parameter at the threshold temperature of 580 K, shown in figure 8.4, indicates that anionic interstitials are generated 113 K below a critical temperature.

The wing parameter is obtained from annihilation energy distribution calculated at higher energies than 511 keV as illustrated in figure 8.5. The reason for higher

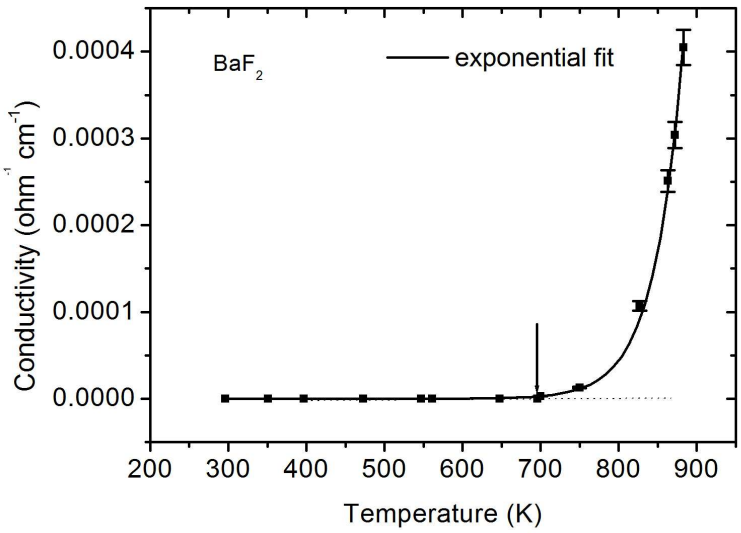

Figure 8.7: Measured conductivity as a function of temperature. Minimum activity in ionic conductivity is established at a threshold temperature of 693 K. This is due to the mobility of flourine ions. The fitting parameters obtained are $y_o = 0$, $A_1 = 1.857E - 14$ (+/- 1.5209E-14) and t1 = 37.06372 (+/- 1.28579)

energy region lies in fact that core electrons have higher momentum and more information regarding annihilation of positrons with different core states can be obtained. It has to be emphasized that without the two-detector system, it would be difficult to calculate the wing parameters. The plot of W versus S parameter shown in figure 8.6 clearly shows the negative slope which is an indication that at low temperatures, the annihilation of positrons with electrons rather take place with valence electrons, in addition to bulk annihilations, rather than at vacancies. As the vacancies increase with temperature, the area under the centroid around the annihilation line (511 keV) increases. This is interpreted as the indication of localization of positrons in vacancies which eventually annihilates giving rise to the centroid area.

8.3 Positron lifetime in barium flouride

Positron lifetime spectrum is composed of the decay function (positron different states), the Gaussian function (resolution function) and the background noise. This is illustrated in figure 8.8

Different decay functions represent different positron states according to equation (8.3) [104].

$$-\frac{dN(t)}{dt} = \sum_{i=1}^{n+1} I_i \lambda_i exp[-\lambda_i t] \tag{8.3}$$

where $N(t)$ is the number of positrons at time t.

In order to obtain reliable positron lifetime values, a source correction has to be done. About 5 to 10 % of the positrons undergo annihilation with electrons in the source material and it becomes crucial to perform source correction in

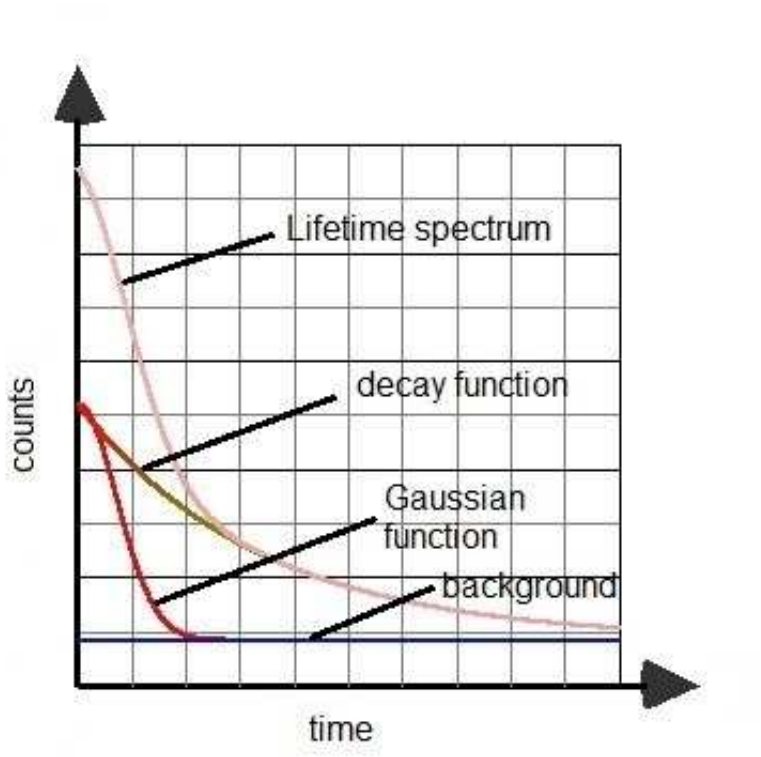

Figure 8.8: Decomposition of positron lifetime spectrum into decay function, the resolution function (Gaussian) and the background noise.

terms of obtaining intensities due to positrons annihilating in the foil (in this case aluminium) using the Bertolucci-Zappa empirical formula [73] which is given by equation (8.4)

$$I_{foil}(\%) = k = 0.324Z^{0.93} \times \Omega^{\alpha} \tag{8.4}$$

where α is given by

$$\alpha = 3.45Z^{-0.4} \tag{8.5}$$

Ω is the surface density of the foil and Z is the average atomic number of the sample. Surface density of aluminium foil is 0.00608 kgm^{-2}. The calculated intensity according to equation (8.4) was found to be 5.64 %.

A typical positron lifetime spectrum in crystal barium flouride is shown in figure 8.9. Figure 8.10 shows the short and long lifetime components, τ_1 and τ_2, respectively. The corresponding intensities are shown in figure 8.13.

8.3.1 Analysis and discussion

Hoydo et al [83] proposed a model where free and trapped states assume both positrons and positronium contribution. The model is as follows

$$\begin{aligned} I_1 &= I_{pPs} + I_{f^+} + I_{foPs} \\ I_2 &= I_{t^+} + I_{toPs} \end{aligned} \tag{8.6}$$

and

$$\begin{aligned} \tau_1 &= \frac{I_{f^+}\tau_{f^+} + I_{pPs}\tau_{pPs} + I_{foPs}\tau_{foPs}}{I_1} \\ \tau_2 &= \frac{I_{t^+}\tau_{t^+} + I_{toPs}\tau_{toPs}}{I_2} \end{aligned} \tag{8.7}$$

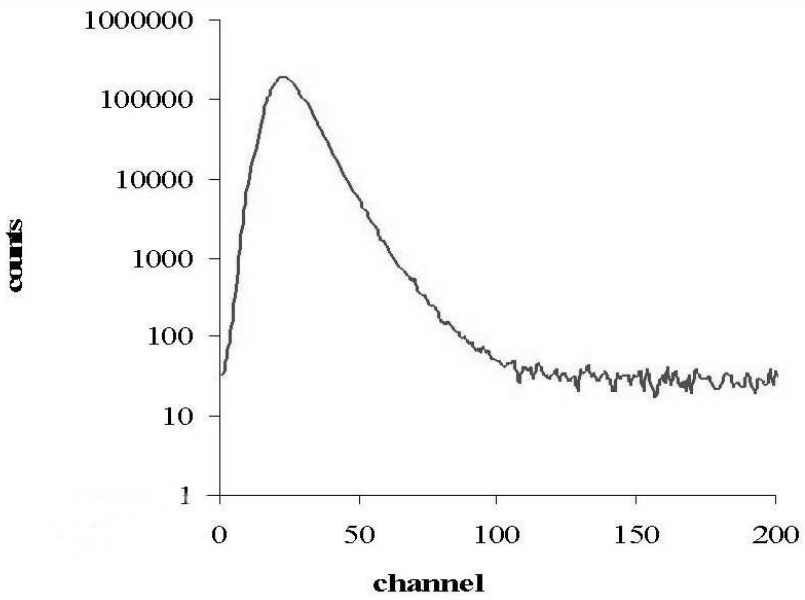

Figure 8.9: Measured positron lifetime spectrum at room temperature. Typically the decomposition of the upper and middle part of the spectrum leads to two positron lifetime components. The Gaussian shape in lower channels is associated with the resolution function.

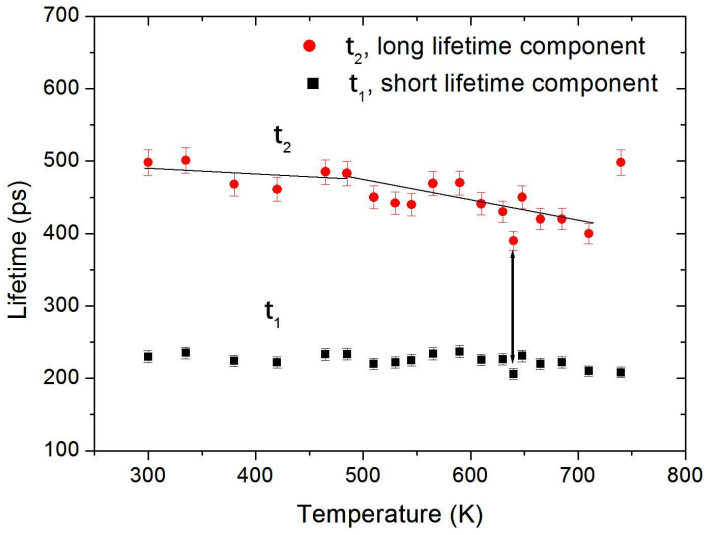

Figure 8.10: Measured positron lifetime components over a temperature range from 300 K to 800 K. The second lifetime components, in addition to annihilations in vacancies, are largely due to faster conversion of ortho-positronium to pick-off annihilation. This is evident from the change of slope in the long lifetime component.

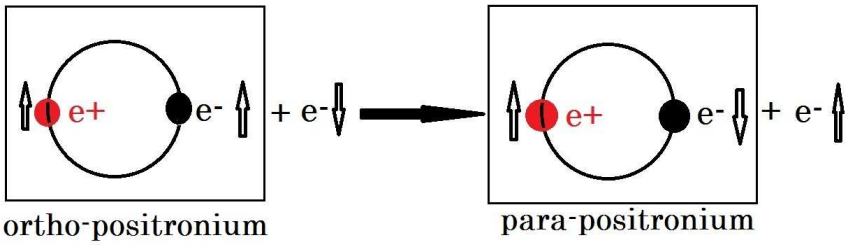

Figure 8.11: Ortho-positronium to para-positronium due to spin conversion.

where the subscripts t^+, f^+, $fpPs$, $foPs$ and $toPs$ refer to trapped positron, free positron, free para-positronium, free ortho-positronium and trapped positronium respectively. I_1 and I_2 are annihilation intensities of the first and second lifetimes respectively.

Ortho-positronium has a long lifetime of 142.04 ns [193] compared to para-positronium which has a lifetime of 125.14 ns [99]. In condensed matter, the ortho-positronium lifetime is affected by one of the following processes:

- Ortho to para - positronium due to spin conversion. In this process an electron which has the same spin as a positron in the positronium system is exchanged with an external electron which has an opposite spin to that of the positron in the ortho-positronium system thus converting ortho-positronium to para-positronium. The annihilation rate will then be the same as that of para-positronium. This is illustrated in figure 8.11.

- Pick-off process. In this process, the positron of the ortho-positronium system collides and annihilates with one of the electrons of the host material and no para-positronium is formed but the emission of two gammas totalling 1022 keV is detected. This process is illustrated in figure 8.12.

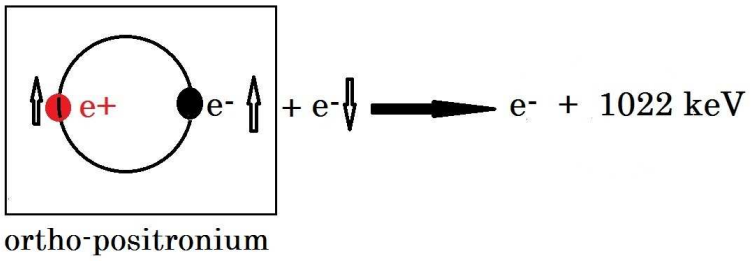

Figure 8.12: Pick-off annihilation process does not involve the formation of para-positronium but the emission of 2γ radiations totalling 1.022 MeV is obsrved.

In our experiment, the probability that 3γ quanta are emitted is very small. In fact there is no evidence of 142 ns ortho-positronium annihilation since our data ranges from 500 ps to 390 ps in the temperature range. Therefore the observed long positron lifetime components in the temperature range, results from ortho-para spin conversion and most probably the pick-off processes in which the electron spin exchange can take place during a collision of positronium with fluorine ions as illustrated in figure 8.12. The second positron lifetime components appear to be decreasing from 499.30 ps at 300 K to 393.94 ps at 641 K as shown in figure 8.13. Elefteriades et al [61] conducted positron annihilation study on BaF_2 only at low temperatures. They concluded that between 80 K and 292 K, positrons start to depopulate the trapping sites (i.e. detrapping of localized positronium). This means that they annihilate in free-states or they form positronium which eventually annihilates. In this work, we extended the investigation into elevated temperatures.

The intensities plotted in figure 8.13 show that the intensity of a long positron lifetime varies between 37.49 % and 24.85 % . At temperature 640 K the intensity of a long positron lifetime component peaks at 37.49 % while at the same temper-

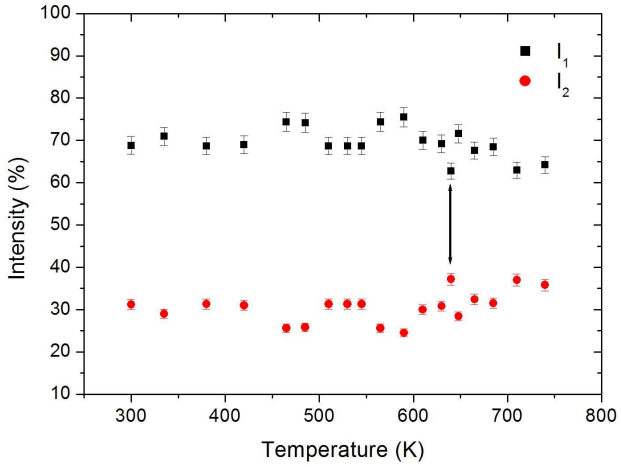

Figure 8.13: Measured positron lifetime intensities over a temperature range from 300 K to 800 K. It is also noted that at 590.3 K, the short positron lifetime component shows a maximum intensity of 75.37 % whilst that of a long positron lifetime shows a minimum intensity at 24.63 %.

ature the short positron lifetime component has a minimum percentage intensity of 63.51 %. At the same temperature of 640 K, the long and short positron lifetimes have minimum values of 392.54 ps and 203.78 ps respectively. This is an anomaly at 640 K and is associated with the beginning of the tail of anomaly in the specific heat of BaF_2 which peaks around 1 200 K [18].

8.3.2 Positron-electron momentum density in BaF_2

Cubic barium flouride of space group Fm3m with lattice constant of 6.196 Angstrom or 11.7087 Borh radius, was used. For the theoretical calculation of positron lifetime (in bulk) or in a vacancy, the MIKA Doppler simulation, which is a program that was developed at Aalto University, is used and is specifically designed to model positron states and annihilations in solids. This requires a construction of either a unit cell or a supercell of a crystal. In this case a supercell was formed in a 124 atoms supercell model for possible annihilation rates in vacancies. The contributions of core and valence electrons toward the electron-positron momentum density only require the use of a unit cell. All atomic positions are in cartesian coordinates and are scaled by a lattice constant.

Figure 8.14 shows a comparison of orbital annihilation rates in the local density approximation (LDA) and independent particle model (IPM). The density functional-based electron-positron enhancement increases rapidly at large distances from the nucleus or as the charge becomes vanishingly small as shown in table 8.1 which compares the calculated values in the LDA and GGA.

Local density approximation does not take into account the variational nature of electron density. Although the LDA is a very good estimate at short distances from the nucleus, at large distances it tends to give unrealistic annihilation rates.

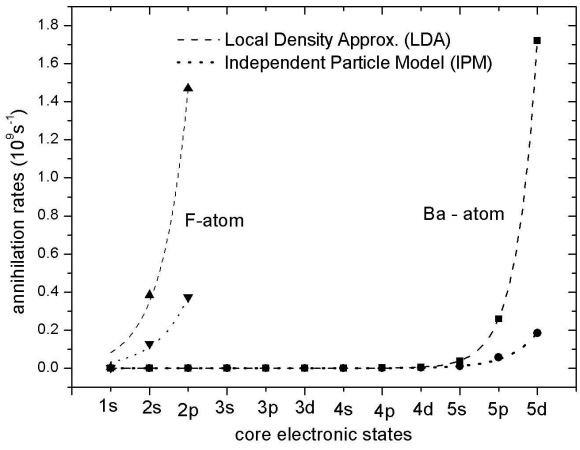

Figure 8.14: Free-atom orbital annihilation rates in barium and flourine atoms within the IPM and LDA.

Table 8.1: Enhancement factors calculated using local density approximation and generalized gradient approximation for comparison purpose.

State	GGA (Ba)	LDA (Ba)	GGA (F)	LDA (F)
1s	1.02771	1.10195	1.15824	1.52058
2s	1.04573	1.17236	2.10571	2.99800
2p	1.04556	1.17498	3.05749	3.92724
3s	1.20029	1.40016		
3p	1.21043	1.40016		
3d	1.21915	1.44164		
4s	1.42731	1.88031		
4p	1.51976	1.98107		
4d	1.76828	2.25638		
5s	3.09075	3.68949		
5p	4.05909	4.56698		
5d	9.24938	9.32316		

In order to correct this, a generalized gradient approximation, in which charge gradient variation is taken into account, is employed for core states to calculate annihilation rates. Figure 8.15 shows a comparison between GGA and IPM.

In alkaline-rare earth and alkali metals as in the case of barium, the high momentum values of the Doppler spectrum (greater than $3\times10^{-3}m_oc$) are dominated by 6s- and 5p- states as shown in figure 8.16. Figure 8.17 shows the core states contributions of flourine atom to the high momentum part of Doppler broadening spectrum. The 2p state dominates the momentum density up to 25 $\times10^{-3}m_oc$.

The ratios of momentum density of barium and flourine with respect to the momentum density of a reference material, in this calculation, aluminium, are shown in figure 8.18. Superposition of high momentum components in barium flouride represents the behaviour of electron-positron annihilations in core states and in valence states. Normalized momentum density is shown in figure 8.19. It can be seen that the theory agrees well with the experiment.

The calculated bulk positron lifetime, which is the inverse of the annihilation rate, was found to be $\tau = 251.54$ ps. This value compares well with the experimental value of 260 ps.

It is also crucial to note that due to high electron density in barium atom over fluorine atom, the probability of positron annihilating with barium valence electron far exceeds the probability of positron annihilating with fluorine valence electron. This is illustrated in table 8.2. The values are calculated in the framework of the generalized gradient approximation.

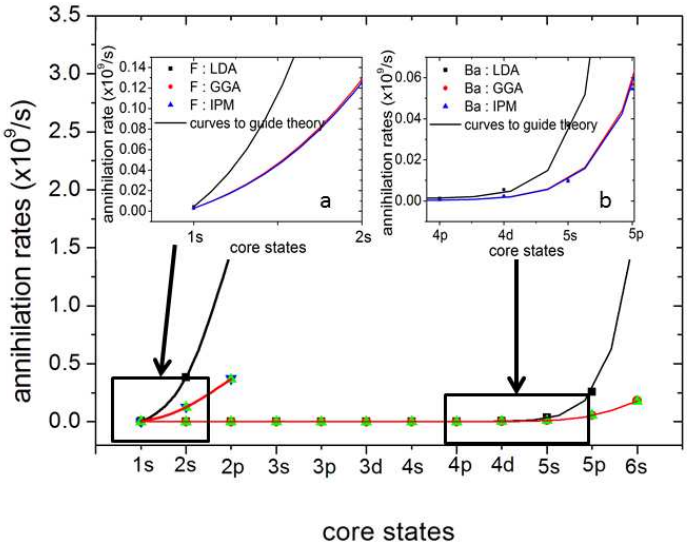

Figure 8.15: Free-atom orbital annihilation rates in barium and flourine atoms within the IPM, GGA and LDA. (a) and (b) shows that the annihilation rates calculated using GGA are slightly higher than the corresponding rates calculated using IPM.

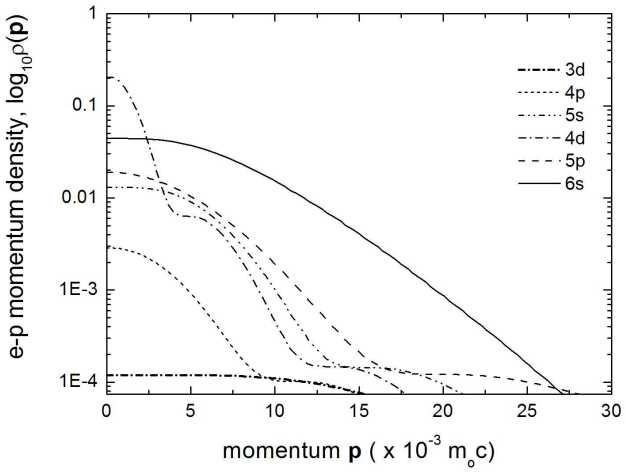

Figure 8.16: Calculated one dimensional electron-positron annihilation momentum density in barium. Electron-positron momentum density is clearly dominated by annihilations in 6s and 5p states at momentum values greater than $3\times10^{-3}m_oc$.

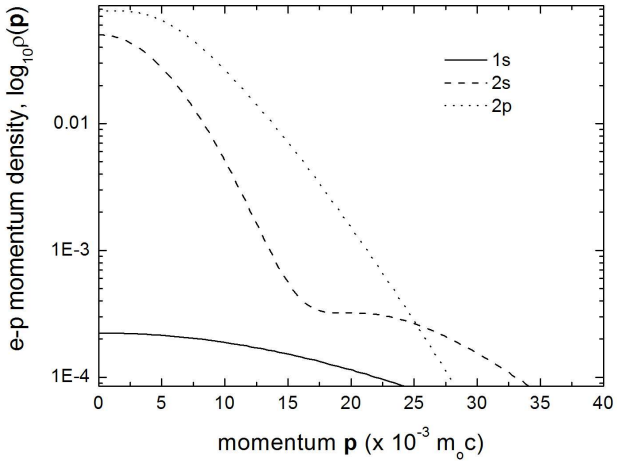

Figure 8.17: Theoretically calculated electron-positron momentum density in flourine. The dominance of 2s and 2p electron-positron annihilations over 1s electron-positron annihilations is evident. Above $2510^{-3}\ m_o c$, 2s electron-positron annihilations dominate the 2p electron-positron annihilations.

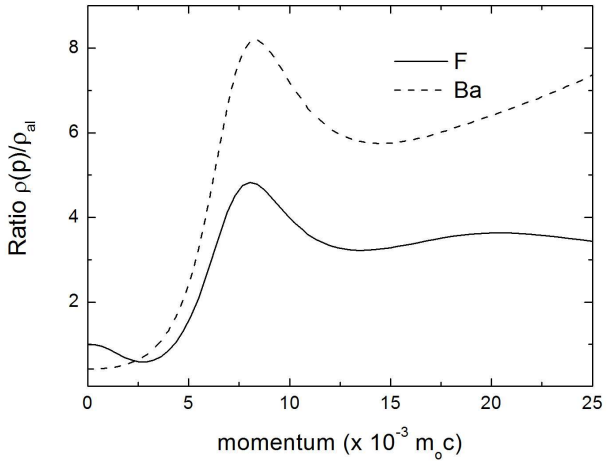

Figure 8.18: Calculated ratios of annihilation probabilities for barium and flourine with respect to the annihilation probability of a reference material, aluminium.

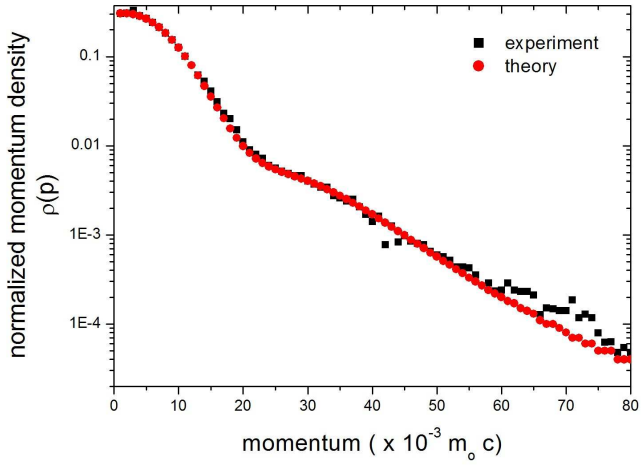

Figure 8.19: Normalized total electron-positron annihilation momentum density in BaF_2 clearly compares well with the experiment. Using coincidence set-up clearly shows the agreement up to about $50 \times 10^{-3} m_o c$.

Table 8.2: Annihilation fractions in BaF_2 at different temperatures due to the presence of anionic vacancies.

BaF_2	λ_{core} $(\times 10^9 s^{-1})$	λ_{5s} $(\times 10^9 s^{-1})$	λ_{5p} $(\times 10^9 s^{-1})$	λ_{6s} $(\times 10^9 s^{-1})$	Annih. fract (%)
F-vac Ba F T=300 K	 0.0053 0.7688	 0.0721	 0.6189	 3.4553	 84.36 15.64
F-vac Ba F T=580 K	 0.0051 0.7578	 0.0698	 0.6019	 3.4257	 84.41 15.59
F-vac Ba F T=693 K	 0.0049 0.7508	 0.0684	 0.5921	 3.4084	 84.44 15.56
F-divac Ba F T=693 K	 0.0052 0.6481	 0.07897	 0.6138	 3.4863	 86.57 13.43

8.3.3 Temperature-dependent S-parameter in BaF_2 in the framework of GGA

Momentum distribution of the annihilating electron-positron pairs is calculated using the state-dependent scheme [7] given as

$$\rho(\mathbf{r}) = \pi \mathbf{r_e}^2 \mathbf{c}\gamma_\mathbf{j} \left| \int \mathbf{dr} e^{\mathbf{p.r}} \psi_+(\mathbf{r}) \psi_\mathbf{j}(\mathbf{r}) \right|^\mathbf{2} \tag{8.8}$$

where γ_j is the enhancement factor and is related to the annihilation rate of core state j and given by [7]

$$\gamma_j = \frac{\lambda_j}{\lambda_j^{IPM}} \tag{8.9}$$

where λ_j^{IPM} is the annihilation rate within the the framework of independent particle model (IPM). λ_j is the annihilation rate of state j within the local density approximation (LDA) or generalized gradient approximation (GGA). Figure 8.20 shows the calculated annihilation rates in barium floride. The enhancement factor which is the ratio of LDA annihilation rate to IPM annihilation rate is shown in figure 8.21 which is based on Arponnen-Pajanne approach [15]. The lattice constant values as a function of temperature were obtained from XRD measurements as explained in chapter 8.1 and are shown in figure 8.3.

The variation of lattice parameter is incorporated in the Generalized Gradient Approximation in which the variation of charge density is included. The corrected enhancement factor is then calculated using equation

$$g_{GGA} = 1 + (g_{LDA} - 1)e^{\alpha\epsilon} \tag{8.10}$$

where the variation in electron density is given by

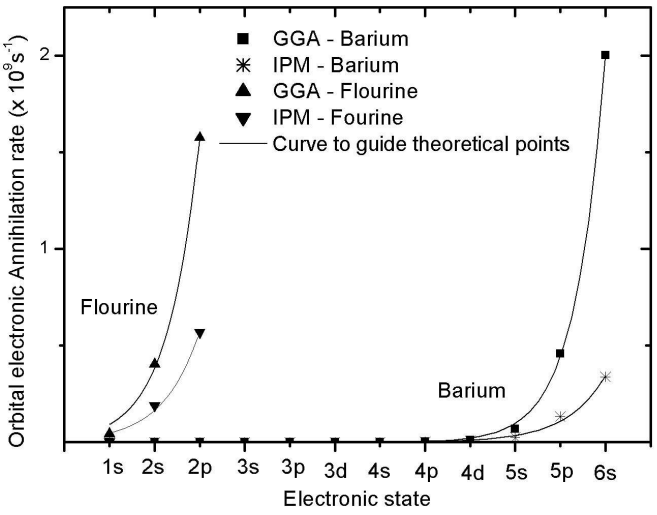

Figure 8.20: Calculated annihilation rates in barium and flourine.

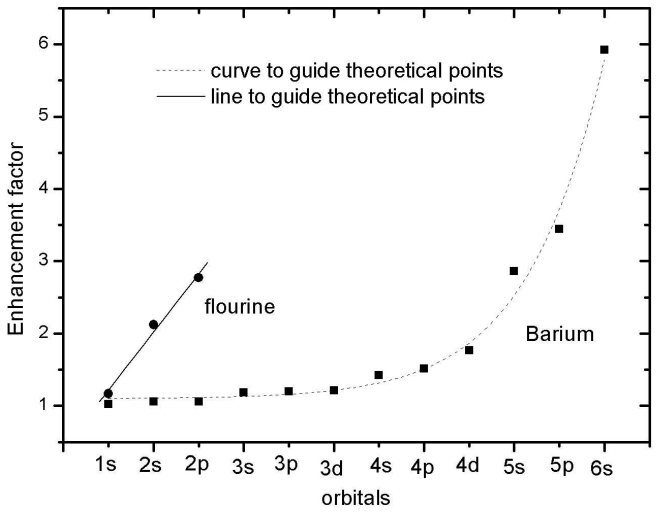

Figure 8.21: Calculated enhancement factor based on Arponen-Pajanne approach in barium and flourine. The visible difference in trends is due to the difference in core states electron densities.

$$\epsilon = \frac{|\Delta n_-|^2}{n_- q_{TF}} \tag{8.11}$$

where q_{TF} is the local Thomas-Fermi screening length given by

$$q_{TF} = (\frac{4}{\pi}(3\pi^2 n_-)^{\frac{1}{3}})^{\frac{1}{2}} \tag{8.12}$$

α is an adjustable parameter. The value of $\alpha = 0.22$ is usually used for Generalized Gradient Approximation and $\alpha = 0.00$ gives the enhancement factor in the Local Density Approximation. In this calculation, α is kept constant at 0.22 for all calculations of momemtum distributions at various temperature points.

The S-parameter as a function of temperature is theoretically calculated at various temperature points by finding the ratio of the selected area, $(0 - 10)\times 10^{-3}$ $m_o c$, to the total area under the distribution curve. This ratio compares well with experimental values up to where the experimental deviation from theoretical trend becomes prominent. This deviation is partly due to the fact that the theory does not consider rapid disordering of flourine sublattice as the temperature increases. This deviation is not of major importance in this study since the threshold temperature in which the defects are created agrees from both the theory and experiment as shown in figure 8.22. The experimental value of 579.5 K in which the disordering of flourine starts without establishing ionic conduction, agrees well with the theoretical value of 588.4 K.

8.4 Positron lifetime in $FeTiO_3$

The $FeTiO_3$ powder (99.9 %) used in this work was produced at School of Physics (University of the Witwatersrand). Grain diameters of approximately 100 μm were achieved. The powders were then pressed into pellets of diameter of 6 mm and

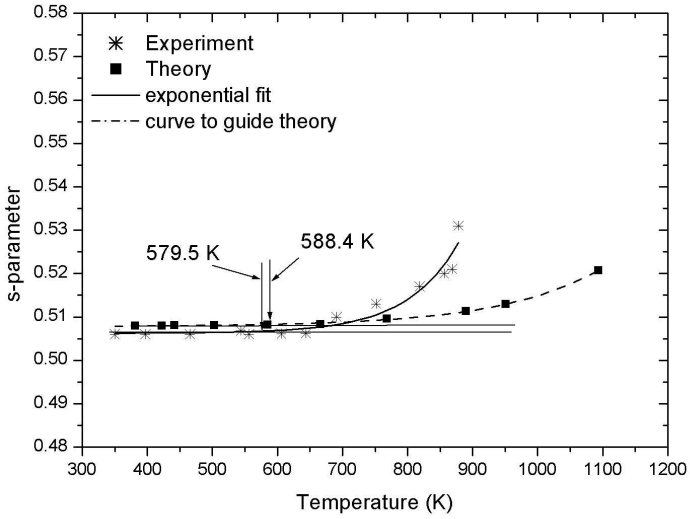

Figure 8.22: Comparison of S-parameter between the values obtained from theory and experiment. The experimental temparature value at 579.5 K in which the flourine sublattice disordering starts without observing the ionic conduction, agrees well with the theoretical temparature value at 588.4 K.

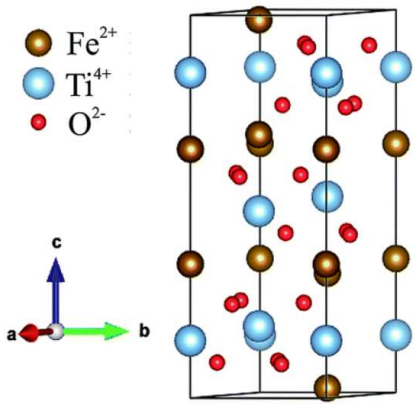

Figure 8.23: The structure of $FeTiO_3$,is related to corundum structure [157].

thickness of 2 mm. The $FeTiO_3$ structure (space group R-3), which is a related structure of corundam, is shown in figure 8.23.

A standard sandwich arrangement in which a $^{22}NaCl$ source of 20 μCi is sandwiched between two $FeTiO_3$ was used. The source is sealed by two electron-welded aluminium foils of thickness 7 μm. The sample chamber was kept at 10^{-4} Torr. The positron lifetime measurement was carried out using a standard coincidence setup. The entire experimental setup is discussed at length in chapter 7. The time resolution was of the order of 280 ps at full width half maximum (FWHM). The data was accumulated between 30 K and 500 K. About 10^6 counts, for each spectrum per selected temperature, was collected. Positron annihilation ratios, $\frac{\lambda_b}{\lambda_d}$, shown in figure 8.24, at various temperature points, are certainly above the threshold of 1.5 which indicates reliable positron lifetime values.

8.4.1 Analysis and discussion

Analysis of positron annihilation rates involves the use of equation (8.3) fitted into the measured positron lifetime spectrum and a proper source correction in

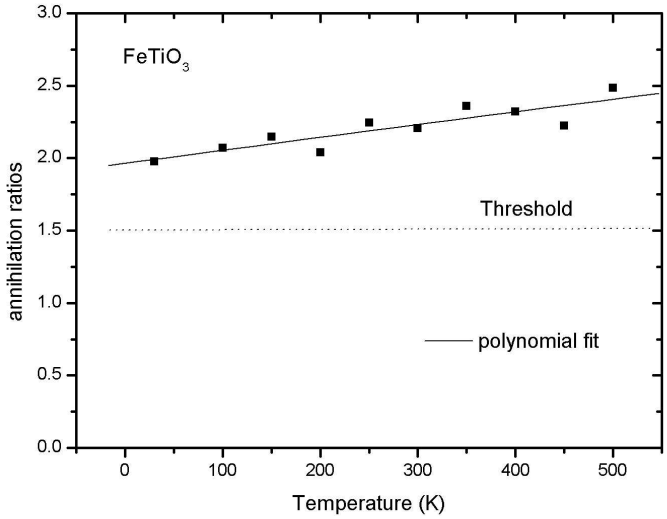

Figure 8.24: Annihilation ratios indicate a clear separation of two positron lifetime components.

which intensities due to electron-positron annihilations in the foil, are given by equation (8.4). The positron lifetimes (or the reciprocal of annihilation rates) in the bulk (i.e. a defect free region) and in a defect are shown in table 8.3 and plotted in figure 8.25. The short positron lifetime of 185.0 ps at 300 K is typically attributed to the free annihilation of positrons in the bulk with valence electrons and possibly through pick-off with unbound electron of oxygen anion (O^{2-}). The second lifetime components arise from annihilations of positrons at defect sites (i.e. at metallic vacancies, Fe^{2+} and possibly Ti^{4+}). In this case it is believed to be coming from annihilations of positrons at vacancy complexes possibly formed as clusters.

Fe free-atom vacancy has an annihilation rate of 4.8260 per ns which was calculated using the local density approximation (LDA) in which the enhancement factor was calculated using the bracketed term of equation (5.21) [24]. Ti free-atom vacancy has a theoretically calculated annihilation rate of 4.975 per ns [121]. Different annihilation rates in these free-atoms show an uneven distribution of positron wavefunctions at various metal vacancies. The observed average positron lifetime values in figure 8.26 show an upward trend with respect to the temperature and this is an indication of increasing metallic cations in the interstitial. The increase of interstitials corresponds to an increase of cationic vacancies in the material thus the observed increase in the second positron lifetime component.

A large positron lifetime is an indication of larger defects (divacancy or cluster). The concentration of defects is proportional to the temperature and therefore more metallic vacancy complexes are generated with respect to the temperature. This suggests a divacancy type of defect at Fe^{2+} ion site at just above room temperature and a cluster as the temperature increases. This is also confirmed by a

Table 8.3: Positron annihilation ratios in $FeTiO_3$ from low to elevated temperatures. Annihilation ratios are expressed in terms of positron lifetimes of both components.

Temperature (K)	τ_{bulk} (ps)	τ_{defect} (ps)	$\frac{\tau_{defect}}{\tau_{bulk}}$
30	177	350	1.9774
100	181	375	2.0718
150	182	391	2.1483
300	184.5	407	2.2060
350	186	439	2.3602
400	186	432	2.3226
500	180	462	2.5667

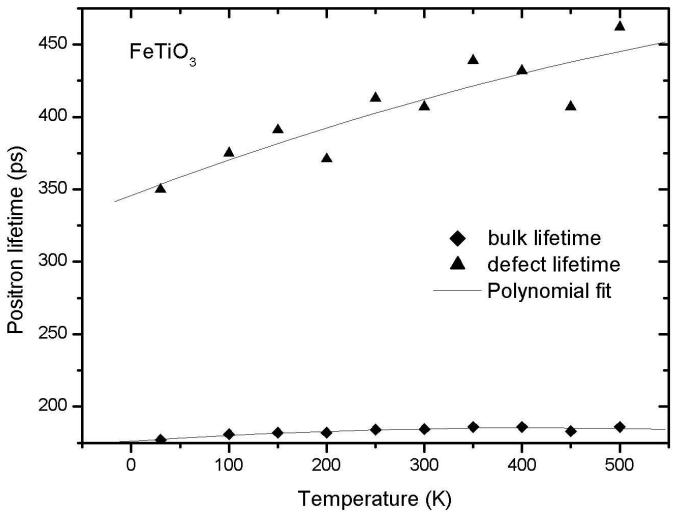

Figure 8.25: First and second lifetime components as a function of temperature.

theoretically calculated value [144] shown in figure 8.27. It is also interesting to note that positron wavefunction has a slightly higher intensity around Fe-vacancy than Ti-vacancy. This can be concluded from their respective annihilation rates.

8.5 Positron annihilation in alkali halides using a variable energy positron beam

Positron annihilation technique was also conducted in alkali halide LiF to determine the near surface defect profile after implantation with 100 keV argon ions (Ar^+) for a range of fluencies from 10^{13} to 10^{16} per cm^{-2}. The implantation was performed at iThemba LABS (Gauteng, South Africa). Pure LiF crystals were obtained from GoodFellows in the United Kingdom. Samples of thickness 1 mm and size 8 mm x 8 mm and each with a net weight of 1.68 g were used in this work.

8.5.1 Optical absorption analysis of LiF implanted with Ar^+

Optical absorptions at wavelengths ranging from 200 to 600 nm were obtained using CARY 400 spectrophotometer to characterize the induced defects due to implantation [173]. Figure 8.28 shows the absorbance against photon wavelength between 200 and 600 nm.

Figure 8.28 clearly shows that the F-band at 245 nm, corresponding to photon energy of 5.06 eV, is present at fluence range. The F_2 band at 444 nm, corresponding to photon energy of 2.79 eV, is only present at higher doses than 10^{13} cm^{-1}. F-band (F color center) is due to the ion vacancy in which an electron trapped [173].

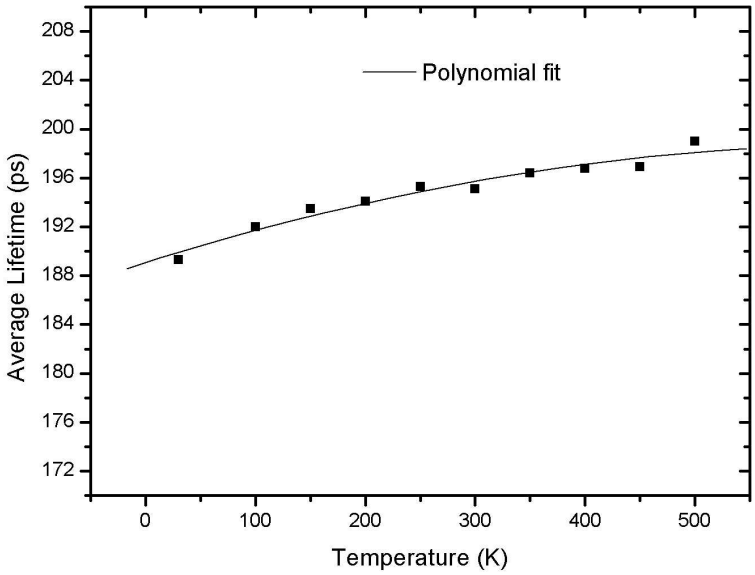

Figure 8.26: Average positron lifetime as a function of temperature.

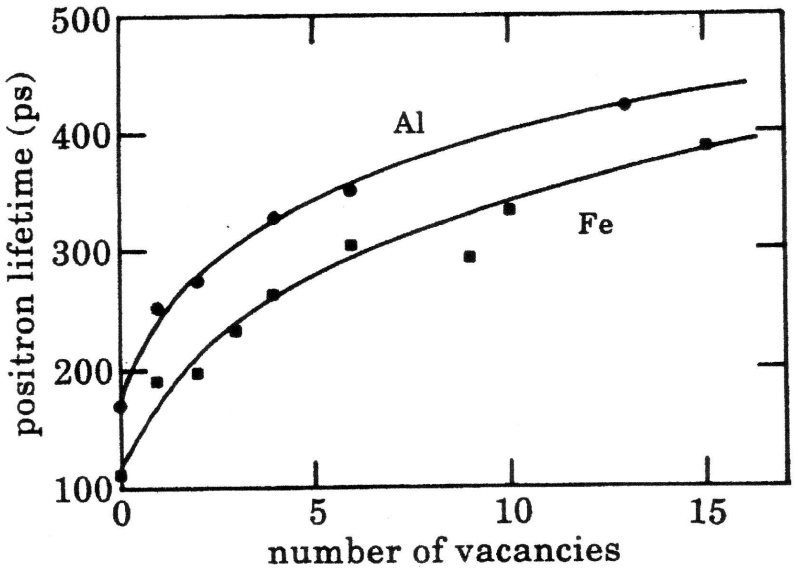

Figure 8.27: Positron lifetime as a function of the number of vacancies. The positron lifetime increases with the number of vacancies [144]. This was done separately through Fe and Al atoms.

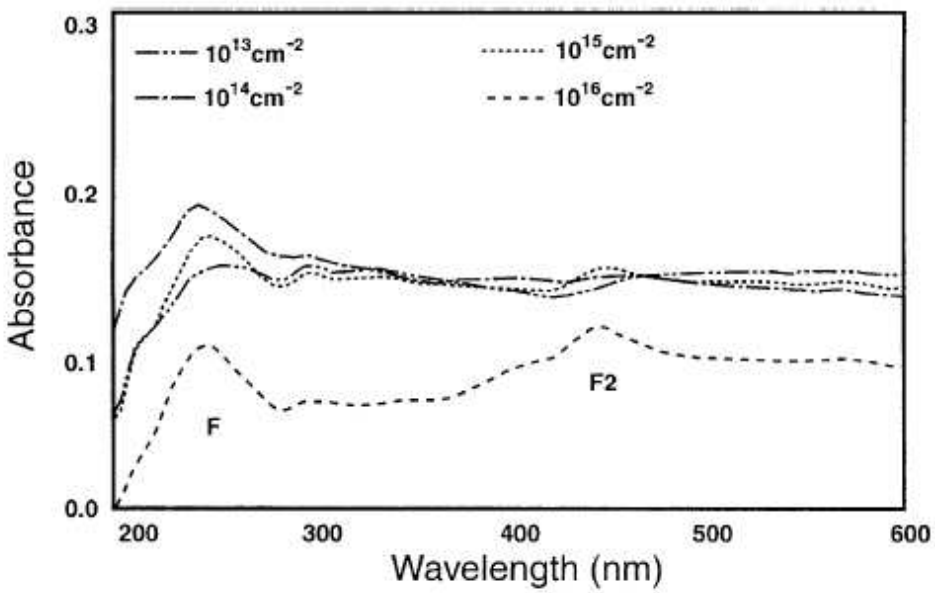

Figure 8.28: The steady growth of F and F_2 bands as the fluence increases is noticeable especially at a fluence of 10^{16} Ar^+ ions per square centimeter [173]

8.5.2 Positron beam analysis of LiF implanted with Ar^+

A schematic diagram of variable energy positron beam used is illustrated in figure 7.10 in chapter 7. Variable energy positron beam has an advantage of selecting various sample layers (depths) for defect identification. The depth profile, also referred to as Makhov profile, $P(z, E)$ of mono-energetic positrons having an energy E is given by equation 8.13 [196, 67, 196]

$$P(z, E) = \frac{mz^{m-1}}{z_o^m} exp - (\frac{z}{z_o})^m \tag{8.13}$$

with

$$z_o = \frac{AE^r}{\rho\Gamma(1 + \frac{1}{m})} \tag{8.14}$$

[196] where m, r and A are commonly used parameters and in general are given by $m = 2$, $r = 1.6$ and $A = 4.0$ μg cm^{-2} KeV^{-r} [196].

The penetration depth profiles in LiF are shown in figure 8.29. A total of about 5×10^6 counts were accumulated each spectrum run for beam energies 0.03 to 25 KeV. Using VEPFIT program [195], the energy dependence of S-parameter was analyzed. Figure 8.30 shows the normalized S-parameter against incident positron energy at different fluencies.

Defects are clearly identified and become prominent as the fluence increases [173] and this identification is achieved through the calculation of S-parameter as a function of incident positron beam energy as shown in figure 8.30. The absence of a peak for the un-implanted LiF sample is visible between the surface S-parameter and the bulk S-parameter. The well defined peaks at 4 keV and 5 keV for higher doses, as shown in figure 8.30 clearly identify the regions of maximum damage

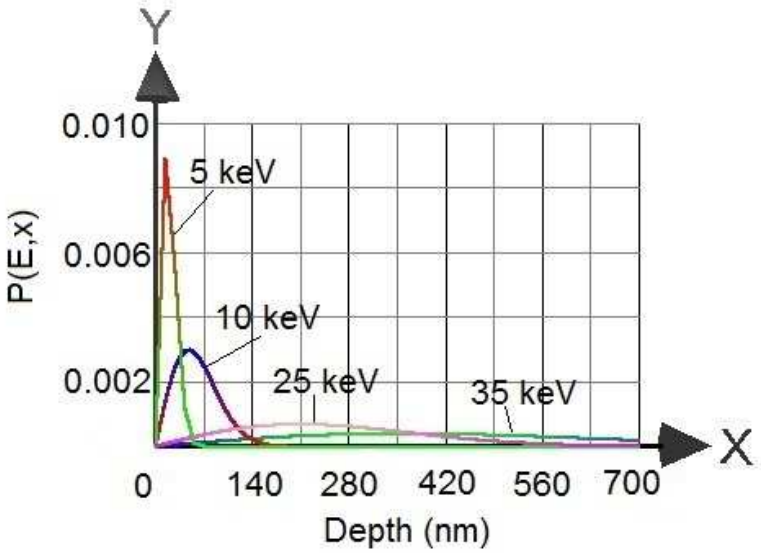

Figure 8.29: Penetration depth profiles P(E,X) in lithium fluoride obtained for different incident positron energies.

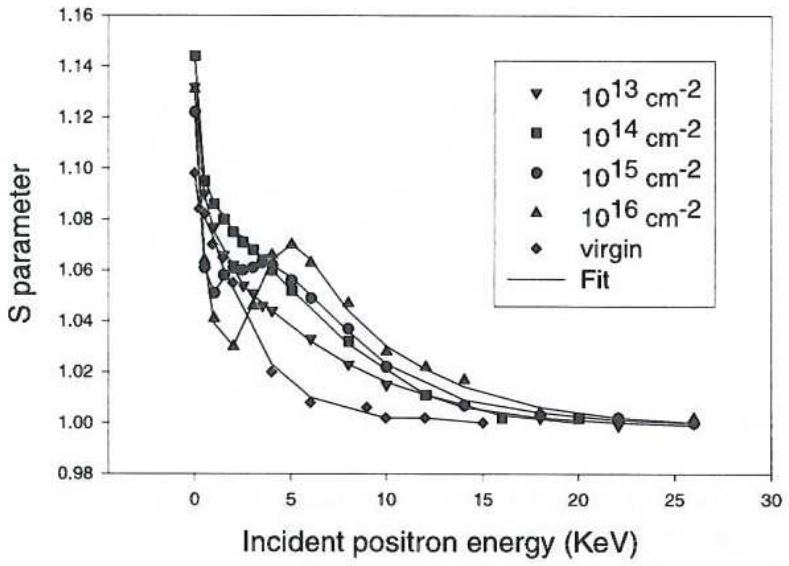

Figure 8.30: Positron beam energy plotted against the S-parameter. The unimplanted LiF (virgin) curve decreases without showing any peaks from the surface to the bulk. Implantation damage is clearly visible for fluencies 10^{16} Ar^{+}/cm^{2} and 10^{15} Ar^{+}/cm^{2} at 5 kev and 4 keV, respectively.

Table 8.4: Annihilation fractions in LiF due to anion and cation vacancies separately.

LiF	lifetime (ps)	λ_{1s} (x $10^9 s^{-1}$)	λ_{2s} (x $10^9 s^{-1}$)	λ_{2p} (x $10^9 s^{-1}$)	Annih. fract (%)
Bulk	142				
Li		0.363171	3.73299		58.34
F		0.00398	0.61490	2.1483	41.66
Li-vac	195.7				
Li		0.010118	3.46061		65.68
F		0.001098	0.324277	1.48751	34.32
F-vac	157.4				
Li		0.419858	3.70203		61.64
F		0.002370	0.518201	2.04456	38.36

due to Ar^+ implantation. The damaged region represents vacancies that act as positron traps. These are positrons, apart from annihilations in the bulk, that eventually annihilate with electrons associated with F centers as shown in figure 8.28.

It is also important to note that some of the contributions toward Doppler broadening needed for the calculation of S-parameters emanate from annihilations of free positrons with valence and core state electrons. The annihilation rates appear to be affected by cation or anion vacancies. Li^+-vacancy has a different effect on fluorine core state annhilations. It is known that, in our particular case, cations have a larger mobility than anions. Table 8.4 shows the effect of cation and anionic vacancies on core and valence annihilation rates.

8.5.3 The effect of implantation on the resistivity in argon-implanted LiF

The concentration of imperfections in crystals can be deduced from temperature dependence of thermal conductivity. Alkali halide LiF is considered for various factors. It is chemically stable and secondly it would be interesting to understand the impact of implantation at different fluencies in relation to its thermal conductivity. Other methods by Kaburaki et al [93] have been utilized at rather low temperatures using the temperature wave method between 1.5 K and 20 K. They also measured thermal diffusivity and specific heat of LiF crystal containing dislocations.

Irradiation of argon-implanted LiF seems to affect the resistivity of lithium fluoride. The resistivity of $LiF : Ar^+$ drops by 24.67% from a fluence of 10^{14} Ar^+/cm^2 to a fluence of 10^{15} Ar^+/cm^2. This is shown in figure 8.31.

This improvement is also accompanied by the enhanced F and F2 bands which are prominent at 245 and 444 nm in the optical absorption spectrum as shown in figure 8.28. It is also interesting that the same phenomenon of crystalline quality improvement has been observed by Takahiro et al [186, 188, 187] on epitaxially grown Ag thin film and Cu films on Si substrates using Rutherford backscattering spectrometry/channeling before and after irradiation.

8.6 Comparison of theory with experiment

The increase in the concentration of interstitials will increase the repulsive energy for interstitial-interstitial interaction. Vacancy-vacancy repulsive energy will also increase. The calculated values are 0.40 eV for vacancy-vacancy interaction and

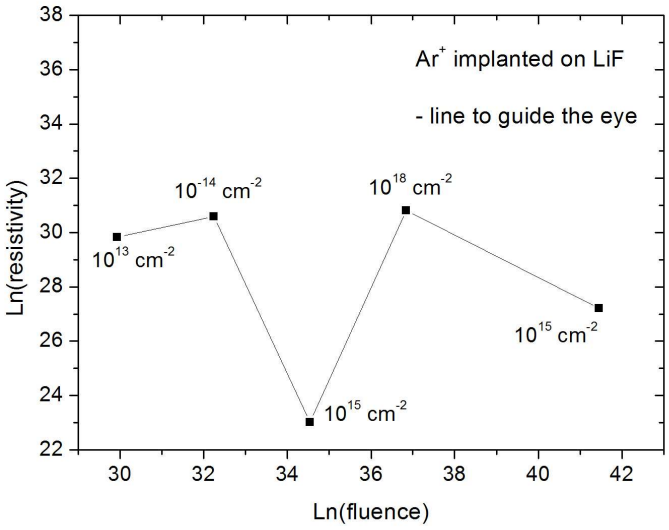

Figure 8.31: The natural log of resistivity plotted against the natural log of fluence clearly shows a 24.67% drop in the log of resistivity from 28.68 to 23.02.

0.55 eV for interstitial-interstitial interaction [130]. This energy has a tendency to slow down the generation of vacancies. As the temperature increases, the thermal expansion of the crystal also varies. The thermal expansion coefficient as a function of temperature, which is discussed in details in chapter 6, is given by equation

$$A = A^o + \frac{x\triangle V^f \triangle H^f}{2kT^2V^p} \tag{8.15}$$

where H is the crystal enthalpy, x the concentration of Frenkel defects and A^o is given by [130]

$$\frac{1}{V^p}(\frac{\partial V^p}{\partial T})_p \tag{8.16}$$

Figure 6.7 shown in chapter 6, shows the variation of thermal expansion as a function of temperature. It is also observed that at 700 K, the thermal expansion coefficient deviates from the linear trend. This is probably due to a rapid disordering of sublattice aided by the expansion of the lattice constant and resulting in the onset of superionic region. The S-parameter as a function of temperature clearly shows that the vacancies are generated 113 K below the critical temperature of 693 K. Therefore this observation ties well with the observed disordering of fluorine sub-structure.

Using positron annihilation technique to calculate the S-parameter in the temperature range as shown in figure 8.4, we also observe that the generation of Frenkel defects take place at 580 K without establishing the ionic conduction. The lattice parameter as a function of temperature increases as the temperature increases until a threshold temperature of 693 K is reached in which the ionic conductivity suddenly increases. This experimentally obtained temperature of

693 K agrees very well with the theoretically calculated value of 700 K obtained by Oberschmidt et al [130]. The generation of Frenkel defects at 580 K agrees very well with theoretically obtained value of 588 K.

Chapter 9

Conclusion

The technique of positron annihilation spectroscopy has been utilized in the investigation of the diverse type of defect configurations prior to the transitional threshold temperature for ionic conduction in superionic barium flouride. Doppler broadening of annihilation radiation momentum and positron lifetime experiments were performed and they reveal the nature of defects but most importantly the elusive thermal point at which the disordering of anion sublattice starts.

In chapter 6, the formation energies of Frenkel and Schottky defects are discussed at length and it is observed that the formation energy of anion Frenkel in barium flouride is far less than that of cation Frenkel. The self-diffusion coefficient of the cations in barium flouride is several orders of magnitude smaller than that of anions. This means that the contribution of cations in ionic conductivity, especially in barium flouride, can be ignored in the temperature range. The non-participation of cations in ionic conductivity in the temperature range is also confirmed by the number of components of positron lifetimes at different temperatures.

The long lifetime component in the temperature range is dedicated to delocalized

positronium annihilations rather than annihilations at either anionic or cationic vacancies. The change of slope in the long lifetime component means that flourine vacancies are rapidly being created as the temperature increases. This can also be viewed as a rapid spin conversion annihilation in a pick-off environment. The absence of a third lifetime component is an indication that anionic vacancies (which are positively charged) are generated in the temperature range. This partly addresses the nature of defects responsible for superionic conduction but again it does not address the elusive temperature point at which these anion Frenkels are generated without observing minimum activity in ionic conduction.

The calculations of momentum ditributions of annihilation radiation of positrons with high and low momentum electrons of the host sample atoms also contribute in the determination of S-parameters in the temperature range. The calculations are conducted in the framework of a Generalized Gradient Approximation in which the electron charge density is considered non-constant. Independent particle model is considered for comparison purposes. Positrons annihilating with low momentum electrons of the host material contribute toward electron-positron annihilation momentum density because of high annihilation fractions with valence electrons. The theory also reveals an interesting situation when an anionic vacancy is created. The annihilation fraction of positrons annihilating with barium 5p and 6s electrons is 84.36 % compared to 15.64 % in fluorine atom. This variation is also temperature dependent as demonstrated in Table 8.4. An interesting revelation from the theory is that when an anionic di-vacancy is generated e.g. at 693 K, the annihilation fraction of positrons with barium low momentum electrons increases to 86.57 % from 84.44 % (anionic mono-vacancy at 693 K). These annihilations with low momentum electrons in host material atoms, in addition to annihilations in the bulk, contribute toward the short positron lifetime

component and electron-positron annihilation momentum density.

X-ray diffraction experiment on barium flouride shows no structural phase change in the temperature range i.e. the cubic structure remains unaltered in the temperature range. XRD is one of the most crucial tools in the determination of the variation of lattice constant measured against the temperature and phase changes. The lattice constant curve deviates from a linear behaviour at a threshold lattice constant of 0.623 nm as indicated in figure 8.3. This is important because it would be difficult to understand or relate the volume expansion (influenced by the variation of lattice constant) of the host material to both the observed ionic conductivity and S-parameter behaviours.

The variation of lattice constant as a function of temperature becomes a major player in the determination of thermal point at which Frenkel defects begin to be created at a detectable rate before entering the superionic region. Theoretical approach shows the creation of defects at 580.0 K while the experimental value is observed at 588.4 K. The experimental deviation of S-parameter from a theoretical curve is mainly due to the disordering nature of anionic sublattice which is not incoporated in the theory. The most crucial point at this stage is that the theory agrees with the experiment. W-parameters obtained from positron-electron annihilation momentum distribution becomes crucial in this study since annihilations of positron with high momentum electrons can be studied using both local density approximation (LDA) and coincidence measurements. The positron-electron momentum density decomposition of host atoms can only be found from wing parameters. W- versus S parameter shown in figure 8.6 shows that at small S parameter values (or at low temperatures), the positron-electron annihilations, apart from bulk annihilations, take place with valence and to certain degree with

core electrons. At elevated temperatures, positrons are likely to annihilate with low momentum electrons because of quantity of vacancies at elevated temperatures.

In addition to the investigation of superionic barium flouride a parallel investigation of the ilmenite disordering was carried out using positron annihilation technique. The utilization of ilmenite was crucial for further test of the validity of theory in a completely different corundum structure of space group R-3. The observed long positron lifetime component in comparison with theoretical calculations clearly shows that it arises from positron annihilations of positrons at metallic vacancies Fe^{2+}. The disordering of Fe substructure which is associated with an increase of long positron lifetime component from 350 ps to 462 ps is due to the mobility of Fe^{+2} ions. There is a possibility that Ti^{+3} might be part of conductivity but the chances are small since we resolved the positron lifetime spectrum into two (not three) lifetime components.

Further test was carried out using variable positron beam on Ar^{+} implanted LiF at various fluencies. Using the penetration depth profile, S-parameter at different incident positron beam energies identifies the concentration of defects. This identification was also confirmed by optical absorption which clearly identified F-band at 242 nm and F2-band at 444 nm.

To our knowledge, we have not yet found any literature in which the positron annihilation technique has been successfully applied to ionic conductors at temperatures higher than 800 K. It would be interesting to pursue studies at these elevated temperatures using positron annihilation technique which is different from neutron diffraction methods and other techniques, in the quest of acquiring a

complete understanding of the crystalline behaviour of ionic barium fluoride and its associated ionic conductivity.

Bibliography

[1] Rahman A. J. Chem. Phys., 65:4845, 1976.

[2] Lidiard A.B. Handbuch der Physik. Springer-Verlag, Berlin, Vol. 20, 1957.

[3] Adkins G.S., Fell R.N. and Sapirstein J. Phys. Rev. Lett., 84:5086, 2000.

[4] Adkins G.S., McGovern N.M., Fell R.N. and Sapirstein J. Phys. Rev. Lett., 82:311, 1999.

[5] Aityan S.K., Ivanov-Shitz, Buchstab A.S., Loshmanov A.A. VINIT (Moscow), N1536 - B90:1–37, 1990.

[6] Akhiezer A.I. and Berestetskii N.B. Quantum Electrodynamics. Wiley:New York, 1965.

[7] Alatalo M., Barbiellini B., Hakala M., Kauppinen H., Korhonen T., Puska M.J., Saarinen K., Hautojarvi and Nieminen R.N. Phys. Rev., B54:2397, 1996.

[8] Allnatt A.R., Chadwick A.V. and Jacobs P.W.M. Proceedings of Royal Society of London, A410:385, 1987.

[9] Anderson C. Phys. Rev., 43:491, 1933.

[10] Mills A.P.(Jr). Phys. Rev. Lett., 41:1828, 1978.

[11] Arponen J. and Pajanne E. Ann. Phys. (NY), 121:343, 1979a.

[12] Arponen J. and Pajanne E. J. Phys., F9:2359, 1979b.

[13] Arponen J. and Pajanne E. In ICPA85, page 21, 1985.

[14] Asai S., Orito S. and Shinohara S. Phys. Lett., B 357:475, 1995.

[15] Barbiellini B., Puska M.J., Torsti T. and Nieminen R.M. Phys. Rev., B51:7341, 1995.

[16] Bardeen J. and Shockley W. Phys. Rev., 80:72, 1950.

[17] Bednorz J.G. and Muller K.A. Z. Phys., B64:189, 1986.

[18] Belosludov V.R., Efremova R.I. and Matizen E.V. Sov. Phys. Solid State [English translation], 16:847, 1974.

[19] Beniere M., Chelma M. and Beniere F. J. Phys. Chem. Solids, 40:729, 1979.

[20] Berestetsky V.B., Lifshis E.M. and Pitaevsky L.P. Relativistskaya Kvantovaya Mekhanika. Moscow:Nanka, 1968.

[21] Bergersen B., Pajanne E., Kubica P., Stott M.J. and Hodges C.H. Solid State Commun., 15:1377, 1974.

[22] Bertolaccini M. and Zappa L. Nuevo Cimento, B52:487, 1967.

[23] Bonne R.W. and Schoonman J. J. Electrochem. Soc., 28:124, 1977.

[24] Boronski E. and Nieminen R.M. Phys. Rev., B34:3820, 1986.

[25] Boyce J.B. and Huberman B.A. Phys. Rep., 51:189, 1979.

[26] Brandt W., Waung H.F. and Levy P.W. Proc. Intern. Symp. Color Centers in Alkali Halides, Rome:48, 1968.

[27] Britton D.T. J. Phys. Condens. Matter, 3:681, 1991.

[28] Britton D.T. and Stormer J. J. Applied Surface Science, 85:1–7, 1994.

[29] Buck O., Tien J.K. and Marcus H.L. Electron and Positron Spectroscopies in Material Science and Engineering. Academy Press, 1979.

[30] Caswell W.E., Lepage G.P. and Sapirstein J. Phys. Rev. Lett., 38:488–491, 1977.

[31] Catlow C.R. and Norgett J. J. Phys., C6:1325, 1973.

[32] Catlow C.R.A. Comments Solid State Phys., 9:157, 1980.

[33] Catlow C.R.A. J. Phys., C15:L9, 1982.

[34] Catlow C.R.A., Chadwick A.V., Corish J., Moroney L.M. and O'Reilly A.N. Cryst. Latt. Def. And Amorph. Mat., 12:193, 1985.

[35] Catlow C.R.A., Comins J.D., Germano F.A., Harley R.T. and Hayes W. J. Phys. C: Solid State Phys., 11:3197, 1978.

[36] Catlow C.R.A., Corish J., Jacobs P.W.M. and Lidiard A.B. J. Phys. C, 14:L121, 1981.

[37] Catlow C.R.A., James R., Mackrodt W.C. and Stewart R.F. Phys. Rev., B25:1006, 1982.

[38] Catlow C.R.,Norgett M.J. and Ross T.A. J. Phys. C: Solid State Phys., 10:1627, 1977.

[39] Catlow:1994. Defects and disorders in crystalline and armophous solids. SpringerLink, 1994.

[40] Ceperley D.M. and Alder B.J. Phys. Rev. Lett., 45:566, 1980.

[41] Chadwick A.V. Solid State Ionics, 8:209, 1983.

[42] Chadwick A.V. and Mario Terenzi. Defect in Solids. NATO ASI series, SpringerLink, 1986.

[43] Chadwick A.V., Kirkwood F.G. and Saghafian. J. Phys. (Paris), 41:C6 – 216, 2008.

[44] Chakraborty B. and Siegel R.W. Phys. Rev., B27:4535, 1983.

[45] Chandrasekhar R. Radiative Transfer. Oxford:Clarendon, 1950.

[46] Chudley and Elliot R.J. Proc. Phys. Soc., 77:353, 1964.

[47] Clausen K., Hayes W., Hutchings M.T., Kjems J.K.,Schnabel P. and Smith C. Solid State Ionics, 5:589, 1981.

[48] Comins J.D., Ngoepe P.E. and Catlow C.R.A. J. Chem. Soc. Faraday Trans., 86:1183, 1990.

[49] Crater H.C. and Wong C.Y. Journal of Physics:Conference Series, 548:012004, 2014.

[50] Czarnecki A., Melnikov K. and Yelkhovsky A. Phys. Rev. Lett., 82:311, 1999.

[51] Daniuk S., Kontrym-Sznajd G., Majsnerowski J., Sob M. and Stachowiak H. J. Phys. Condens. Matter, 1:6321, 1989.

[52] Daniuk S., Kontrym-Sznajd G., Rubaszek A., Stachowiak H., Mayers J., Walters P.A. and West R.N. J. Phys., F17:1365, 1987.

[53] Daniuk S., Sob M. and Rubaszek A. Phys. Rev., B43:2580, 1991.

[54] Denham P., Field G.R., Morse P.L.R. and Wilkinson G.R. Proc. R. Soc. A, 317:55, 1970.

[55] Derrington C.E., Navrosky A. and O'Keeffe. Solid St. Commun., 18:47, 1976.

[56] Dickens M.H., Hayes W., Hutchings M.T. and Smith C. J. Phys. C: Solid State Phys., 12:L97, 1979.

[57] Dixon M. and Gillian M.J. J. Phys. C: Solid State Phys., 11:165, 1978.

[58] Doyama M., Suzuki Y., Ishibashi S. and Abe T. J. Phys. Condens. Matter, 1:SA83, 1989.

[59] Dutt N., Sharma O.P. and Shanker J. Phys. Status Solidi, 127:67, 1985.

[60] Dworkin A.S. and Bredig M.A. J. Phys. Chem, 72:1227, 1968.

[61] Elefteriades C.A., Chardalas M., Dedoussis Sp. and Charalambous Stef. Cryst. Res. Technol., 3:437–440, 1988.

[62] Prokop'ev E.P. Sov. Phys. Semicond., 26:941, 1992.

[63] Prokop'ev E.P. Phys. Chem. Mech. Surfaces, 9:1403, 1993.

[64] Nielsen B. et. al. Phys. Rev. B, 32:2296, 1985.

[65] Foster D. Hydrodynamic Fluctuations, Broken Symmetry and Correlation Functions. Benjamin, New York, 1975.

[66] Frieze W.E., Lynn K.G. and Welch D.O. Phys. Rev., B31:15, 1985.

[67] Ganguly B.N., Menon R., Yalagoud N.R., Bandyopadhyay S.K., Anwand W. and Brauer G. Physica Status Solidi, 252:2024 – 2033, 2015.

[68] Gillan M.J. and Richardson D.D. J. Phys. C: Solid State Phys., 13:L61, 1979.

[69] Goldanskii V.I. Physical Chemistry of a positron and positronium. Moscow:Nanka, 1968.

[70] Goldanskii V.I. et. al. Struc. Chem., 2:135, 1991.

[71] Greenwood N.N. Ionic Crystals, Lattice Defects and Nonstoichiometry. Chemical, New York, 1970.

[72] Gyorffy B.L., Szotec Z., Temmerman W.M. and Stocks G.M. J. Phys. Condens. Matter, 1:SA119, 1989.

[73] Hakala T. Special Assignment. Helsinki University of Technology, 2001.

[74] Hakkinen H., Makinen S. and Manninen M. Europhys. Lett., 9:809, 1989.

[75] Hao H.Y. and Maris H.J. Phys. Rev. B, 64(064302):1–7, 2001.

[76] Harns I. and Brown L. Phys. Rev, 105:1656, 1957.

[77] Hautojarvi P. Positrons in Solids, Topics in Current Physics. Springer-Verlag, 1979.

[78] Hayes W. Contemp. Phys., 19:469, 1978.

[79] Hayes W. and Hutchings M.T. Series on Directions in Condensed Matter, 2:247 – 362, 1981.

[80] Heyne L. Electrochimica Acta, 15:1251 – 1266, 1970.

[81] Hohenberg P. and Kohn W. Phys. Rev., 136:B864, 1964.

[82] Hood G.M. and Morrison J.A. J. App. Phys., 38:4796, 1967.

[83] Hoydo T. and Steward A.T. Phys. Rev. Lett., 29B:4164, 1984.

[84] Huberman B.A. Phys. Rev. Lett., 32:1000, 1974.

[85] Hull S. Rep. Prog. Phys., 67:1233–1314, 2004.

[86] Hutchings M.T., Clausen K., Dickens M.H., Hayes W., Kjems J.K., Schnabel P.G. and Smith C. J. Phys., C17:3903, 1984.

[87] Huttunen P.A., Vehanen A. and Nieminen R.M. Phys. Rev., B40:11923, 1989.

[88] Hwang L.P. and Freed J.H. J. Chem. Phys., 63:118, 1975.

[89] Jacobs P.W.M. J. Phys. Chem. Solids, 41:431–436, 1980.

[90] Jarlborg T. and Singh A.K. Phys. Rev., B36:4660, 1960.

[91] Jensen K.O. J. Phys. Condens. Matter, 1:10595, 1989.

[92] Jones R.O. and Gunnarsson O. Rev. Mod. Phys., 61:689, 1989.

[93] Kaburaki H., Kogure Y. and Hiki Y. J. Phys. Soc. Jpn., 49:1106–1114, 1980.

[94] Kahana S. Phys. Rev., 117:123, 1960.

[95] Kahana S. Phys. Rev., 129:1622, 1963.

[96] Kanda G.S., Ravelli L., Lowe B., Egger W. and Keeble D.J. J. Phys. D: Appl. Phys., 49:025305, 2016.

[97] Kawane K. et al. Phys. Rev. B, 60:11984, 1999.

[98] Keen D. J. Phys: Condens. Matter, 14:R819–R857, 2002.

[99] Kniehl B.A. and Penin A.A. Phys. Rev. Lett., 85:1210, 2000.

[100] Kohn W. and Sham L.J. Phys. Rev., 140:A1133, 1965.

[101] Kosachi I., Litvinchuk A.P., Tarasov J.J. and Valack M Ya. J. Phys.:Condens. Matter, 1:929–934, 1989.

[102] Kourganoff V. Basic Methods in Transfer Problem. Oxford:Clarendon, 1952.

[103] Krause-Rehberg R., Leipner H.S., Abgarjan T. and Polity A. Applied Physics A, 66:599–614, 1998.

[104] Krause-Rheberg R. and Leipner H.S. Positron Annihilation in Semiconductors - Defect Studies. Berlin Springer-Verlag, 1999.

[105] Kudrnovsky J., Christensen N.E. and Masek J. Phys. Rev B, 43:12597, 1991.

[106] Lantto L.J. Phys. Rev., B36:5160, 1987.

[107] Lee C.Y. Appl. Sci. Converg. Technol., 25 (5):85 – 87, 2016.

[108] Levine C., Hoffman E.J. Phys. Med. Biol., 44:781–799, 1999.

[109] Linderoth S. J. Phys. Condens. Matter, 1:SA55, 1989.

[110] Lindqvist S. and March N.H. Theory of Inhomogeneous Electron Gas. Plenum,New York, 1983.

[111] O'Keeffe M. Com. Solid St. Phys., 7:163, 1977.

[112] Makkonen I., Korhanen E., Prozheeva V. and Tuomisto F. J. Phys. Condens Matter, 28 (22):224002, 2016.

[113] Manuel A.A. J. Phys. Condens. Matter, 1:SA107, 1989.

[114] Matsubara T. J. Phys. Soc.Japan, 38:1076, 1975.

[115] Matzke H. J. Materials Science, 5:831, 1970.

[116] Megatron electronics and control. www.megatron.co.il, 2008.

[117] Melnikov K. and Yelkhovsky. Phys. Rev., D62:116003, 2000.

[118] Mijnarends P.E. and Singru R.M. Phys. Rev., B19:6038, 1979.

[119] Mijnarends P.J. and Lynn K.G. Europhys. News, 25:178, 1994.

[120] Mikeska H.J. Phys. Lett., A24:402, 1967.

[121] Mizuno M., Araki H. and Shirai Y. Materials Transactions, 43(7):1451–1455, 2002.

[122] Ngoepe P.E. and Comins J.D. J. Phys., C19:L267, 1986.

[123] Nico J.S., Gidley D.W. and Rich A. Phys. Rev. Lett., 65:1344, 1999.

[124] Nieminen R.M. Positron beams and Their Applications. World Scientific Publishing, 2000.

[125] Nieminen R.M. and Oliva J. Phys. Rev., B22:2266, 1980.

[126] Nieminen R.M. and Oliva J. Phys. Rev., B22:2266, 1980.

[127] Nieminen R.M. and Puska M.J. Phys. Rev. Lett., 50:281, 1983.

[128] Nieminen R.M., Boronski E. and Lantto L.J. Phys. Rev., B32:1377, 1985.

[129] Nilen R.W.N., Connell S.H., Britton D.T., Fischer C.G., Sendezera E.J., Schaaff P., Schmidt W.G., Sellscop J.P.F. and Verwoed W.S. J. Phys. Condens. Matter, 9:6323, 1997.

[130] Oberschmidt J. Phys. Rev. B, 23 (10):5038, 1981.

[131] Oberschmidt J. and Lazarus D. Phys. Rev., B21:2952, 1980.

[132] Mongensen O.E. J. Chem. Phys., 60:998, 1974.

[133] Mongensen O.E. Positron annihilation in Chemistry. Springer-Verlag, Berlin, 1995.

[134] Oostra D.J. and den Hartog H.W. Phys. Rev., B29:2423, 1984.

[135] Ouwerkerk M., Kelder E.M., Schoonman J and Miltenberg J.C. Solid State Ionics 9, 10:531, 1983.

[136] Pardee W. and Mahan G.D. (a) J. Solid State Chem., 15:310, 1975.

[137] Pecora L.M. J. Phys. Condens. Matter, 1:SA1, 1989.

[138] Perdew J.P. and Wong Y. Phys. Rev., B45:13244, 1992.

[139] Perdew J.P. and Zunger A. Phys. Rev., B23:5048, 1981.

[140] Plazaola F., Scitsonen A.P. and Puska M.J. J. Phys. Condens. Matter, 6:8809, 1994.

[141] Prochazka I., Cizek J., Brauer G. and Anwand W. Rosnov pod Radhostem, Czeck Republic, 20:22, 2009.

[142] Prokop'ev E.P. Positronics of Ionic Crystals, Semiconductors and Metals. Moscow:Ked.-Izd Otdel MIET, 1999.

[143] Puska M.J. J. Phys. Condens. Matter, 3:13892, 1991.

[144] Puska M.J. and Nieminen R.M. J. Phys., F13:333, 1983.

[145] Puska M.J., Corbel C. and Nieminen R.M. Phys. Rev., B41:9980, 1990.

[146] Puska M.J., Nieminen R.M. Rev. Mod. Phys., 66 3:841–897, 1994.

[147] Puska M.J.Makinen S., Manninen M. and Nieminen R.M. Phys. Rev., B39:7666, 1989.

[148] Fuller R. Point Defects in Solids, Edited by Crawford J.H. and Slifkin L. Plenum, New York, 1972.

[149] Radulescu A., Padureanu I., repeanu N., Beldiman A., Kozlov A. and Semenov V.A. Phys. Rev., B59:3270, 1991.

[150] Rahemi R. Cond-mat. mat. mtrl-sci, arXiv:1602.01709v1, v1, 2016.

[151] Rahlfs P. Z. Physik. Chem, B31:157, 1936.

[152] Ramasamy P. and Nagaragian T. Phys. Status Solidi, 35:K105, 1976.

[153] Rammutla E., Comins J.D., Erasmus R.M., Netshisaulu T.T., Ngoepe P.E. and Chadwick A.V. Chemical Physics, 467:6 – 12, 2016.

[154] Rathore V. International Journal of Theoretical and Applied Sciences, Special Issue - NCRTAST, 8 (1):151 – 155, 2016.

[155] Remoissenet M. Waves called solitons:Concepts and experiments. Berlin Springer-Verlag, 1994.

[156] Remoissenet M. Waves called Solitons. Springer-Verlag,Heidelberg,3^{rd} Edition, 1999.

[157] Riberio R.A.P and Lazaro S.R. RSC Adv., 4:59839 – 59846, 2014.

[158] Rice M.J., Strassler S. and Toombs G.A. Phys. Rev. Lett., 32:596, 1974.

[159] Rich A. Rev. Mod. Phys., 53:127, 1981.

[160] West R.N. Adv. Phys., 22:3, 1973.

[161] Saarinen K., Corbel C., Hautojarvi P., Lank P., Pierre F. and Vignaud. J. Phys. Condens. Matter, 2:2453, 1990.

[162] Salamon M.B. (ed.). Physics of Superionic Conductors. (Springer:Berlin), 1979.

[163] Samara A. J. Phys. Chem. Solids, 40:509, 1979.

[164] Sata N., Eberman K., Eberl K. and Maier J. Nature, 408:946, 2000.

[165] Schmidt E.D. and Vedam K. J. Phys. Chem. Solids, 27:1563, 1996.

[166] Schroter W. and Nolting J. J. Phys. (Paris) Colloq., 41:c6–20, 1980.

[167] Schultz P.J. and Lynn K.G. Rev. Mod. Phys., 60:701, 1989.

[168] Schulz M. Annual Rev. Mater. Sci., 12:351–376, 1982.

[169] Sedivy L., Cizek J., Belas E., Grill R. and Melikhova O. Sci. Rep., 6:20641, 2016.

[170] Seeger A. Appl. Phys., 4:183, 1974.

[171] Seeger A. Appl. Surf. Sci., 85:8, 1995.

[172] Seeger A. and Britton D.T. Appl. Surf. Sci., 149:287 – 303, 1999.

[173] Sendezera E.J., Davidson A.T., Jili P.T., Chithambo M.L., Anwand W., Brauer G. and Nicht E.H. . Nucl. Instrum. Meth., B 192:202 – 205, 2002.

[174] Seymour G. Topics in Applied Physics. (Springer:Berlin), 1977.

[175] Shapiro S.M. and Reidinger F. Physics of Superionic Conductors, Edited by Salamon M.B. Springer, Berlin, 1979.

[176] Shi J., Wang J., Zhu Z. and Wu Y. Materials Research, 19 (2):316 – 321, 2016.

[177] Shiotani N., Sakai N., Ito M., Mao O., Itoh F., Kawata H., Amemiya Y. and Ando M. J. Phys. Condens. Matter, 1:SA27, 1989.

[178] Simon R., Cherry D., Sorenson A. and Phelps M. Physics in Nuclear Medicine. Elsevier, 2012.

[179] Singh A.N. Journal of Applied Spectroscopy Reviews, 51 (5):359 – 378, 2016.

[180] Soininen E., Makinen J., Beyer D. and Houtojarvi P. R.M. Phys. Rev., B46:13104, 1992.

[181] Sterne P.A. and Kaiser J.H. Phys. Rev., B43:13892, 1991.

[182] Stoll H., Castellaz P., Koch S., Major J., Schneider H., Seeger A. and Siegle A. Mater. Science Forum, 92:255–257, 1997.

[183] Stoll H., Wesolowski P., Koch M., Maier K., Major J and Seeger A. Mater. Sc. Forum, 1989:104–110, 1992.

[184] Surka A., Chakrabarti M., Ray S.K., Bhowmick D. and Sanyal D. J. Phys. Condens Matter, 23 (15):155801, 2011.

[185] Takahashi T. and Iwahura H. J. Appl. Electrochem, 3:65, 1973.

[186] Takahiro K., Nagata S. and Yamaguchi S. Appl. Phys. Lett., 69:2828 – 2830, 1996.

[187] Takahiro K., Nagata S. and Yamaguchi S. Appl. Phys. Lett., 69:2828 – 2830, 1996.

[188] Takahiro K., Takeshima N., Kawatsura K., Nagata S., Yamamoto S. and Naramoto H. Surface and Coatings Technology, 158-159:334 – 338, 2002.

[189] Thoma R.E. and Brunton G.D. Inorg. Chem., 5:1937, 1966.

[190] Tsuchiya Y., Tamaki S., Waseda Y. and Toguri J.M. J. Phys., C11:651, 1978.

[191] Tubandt C. and Lorenz E. Z. Phys. Chem., 87:513–542, 1914.

[192] Lauff U. Dr. Rer. Nat. Thesis: Stuttgart University. Gottingen:Cuvillier, 1997.

[193] Vallery R.S., Zitzewitz P.W. and Gidley D.W. Phys. Rev. Lett., 90:203402, 2003.

[194] Van House, Van Veen A., Schut H., de Vries J., Hakvoort R.A. and IJpma M.R. In SLO90, page 171, 1990.

[195] Van Veen A., Schut H., de Vries J., Hakvoort R.A. and Ijpma M.R. AIP Conf. Proc., 218:171, 1990.

[196] Vehanen A., Saarinen K., Hautojarvi P. and Huomo H. Phy. Rev., B 35:4606, 1987.

[197] Hayes W. Light Scattering in Solids ed. Cardona M. and Guntherodt G. (Springer:Berlin), 1982.

[198] Wang Y., Richards W.D., Ong S.P., Miara L.J., Kim J.C., Mo Y. and Ceder G. Nature Materials, 14:1026 – 1031, 2015.

[199] Welch D.O. and Dienes G.J. J. Phys. Chem. Solids, 38:311, 1977.

[200] West R.N. Positron Studies of Condensed Matter. Taylor and Francis Ltd., 1974.

[201] Williams M.M.R. The Slowing Down and Thermalization of Neutrons. Amsterdam:North-Holland, 1966.

[202] Wilson N.C., Russo P., Muscat J. and Harrison N.M. Phys. Rev. B, 72:0241110, 2005.

[203] Wu C.S. and Moskowski S.A. beta decay. New York:Interscience, 1996.

[204] Wurschum R., Bauer W., Maier K., Seeger A. and Schaefer H-E. J. Phys. Condens. Matter, 1:SA33, 1989.

[205] Zhukov A. Novel Functional Magnetic Material. Springer Series in material science, 2016.